UNIVERSITY OF CALIFORNIA
RIVERSIDE

Synthesis and Applications of Large Area Graphene-Based Electrode Systems

A Dissertation submitted in partial satisfaction
of the requirements for the degree of

Doctor of Philosophy

in

Mechanical Engineering

by

Rajat Kanti Paul

December 2011

Dissertation Committee:
Prof. Ashok Mulchandani, Chairperson
Prof. Masaru Rao
Prof. Roger Lake

The Dissertation of Rajat Kanti Paul is approved:

_____

_____

_____
Committee Chairperson

University of California, Riverside

Acknowledgements

I wish to convey my heartiest gratitude and profound respect to my supervisor Dr. Ashok Mulchandani, Professor, Chemical and Environmental Engineering, University of California, Riverside for his continuous guidance, constructive suggestions and whole-hearted supervision throughout the progress of this work, without which this thesis could never be materialized. I am deeply grateful to him for his continuous efforts to make me acquainted with the world of advanced research. I also would like to express my gratitude to Prof. Masaru Rao, Mechanical Engineering and Prof. Roger Lake, Electrical Engineering, University of California, Riverside for being my dissertation committee members and their kind encouragements and advices. I also thank Prof. Huinan Liu, Bioengineering, University of California, Riverside for collaborating with part of my thesis work in stem cell research.

This work has benefited directly or indirectly in numerous ways from a number of people both in UC Riverside and outside. Especially, I am grateful to Prof. Cengiz Ozkan, Mechanical Engineering, University of California, Riverside and Prof. Robert Haddon, Chemistry, University of California, Riverside for providing me with their lab facilities and advices to develop my thesis project. I wish to thank all of my friends and lab-mates in *Bionanotechnology and Biosensor Group* for the friendly feelings I have had with them while studying and doing research in UC Riverside. Especially, I would like to thank Dr. Sushmee Badhulika, Sira Srinives, Tapan Kumar Sarkar, James Kakoullis,

Nuvia Saucedo, Trupti, Dr. Rajesh, Dr. Chakar Tilili, Dr. Gong, Miro Penchev, Jian Lin, Ziebin Zhong, Maziar Ghazinezad, for their help and encouragements.

I would like to thank the office staff of Department of Mechanical Engineering and Department of Chemical and Environmental Engineering for their time and help throughout the course of my Ph.D work. I am grateful to Mark Heiden, Facility Manager, Center for Nanoscale Science and Engineering (CNSE; UC Riverside Cleanroom) facility UC Riverside for providing me the scope to develop hands-on skills in semiconductor processing technology. I also appreciate help of Dexter Humphrey, Senior Development Engineer in training with all the tools in the Cleanroom.

And I am deeply indebted to my father, my mother, my brother, my sisters and my wife (Sumi) for their encouragement, patience and love.

Dedication

To My Parents.

ABSTRACT OF THE DISSERTATION

Synthesis and Applications of Large Area Graphene-Based Electrode Systems

by

Rajat Kanti Paul

Doctor of Philosophy, Graduate Program in Mechanical Engineering
University of California, Riverside, December 2011
Professor Ashok Mulchandani, Chairperson

Graphene is a single sheet of carbon atoms with outstanding electrical and physical properties and being exploited for applications in electronics, sensors, fuel cells, photovoltaics and energy storage. However, practical designs of graphene-based electrode systems and related experimental implementations are required to realize their widespread applications in nano- to bioelectronics. In this dissertation, different graphene-based electrode systems having metallic and semiconducting properties are synthesized optimizing process conditions. Also realized is the potential of the fabricated electrode systems by applying them in practical applications such as sensor devices and fuel cells.

The zero bandgap of semimetal graphene still limits its application as an effective field-effect transistor device or a chemiresistor sensor operating at room temperature. It has been shown theoretically and experimentally that graphene nanoribbons (GNRs) or

nanomeshes (GNMs) can attain a bandgap that is large enough for a transistor device, and hence would show high sensitivity to various gaseous species or biomolecules. Large-area mono- and bilayer graphene films are synthesized by a simple chemical vapor deposition (CVD) technique depending on the carbon precursors such as methane, acetylene and ethanol, and the results are compared using optical microscopy (OM), Raman spectroscopy, high-resolution transmission electron microscopy (HRTEM) and x-ray photoelectron spectroscopy (XPS). A simple reactive ion etching (RIE) combined with well-established nanosphere lithography is performed on the synthesized CVD-grown monolayer graphene platform to fabricate large area GNMs with specific dimension and periodicity. The fabricated GNMs chemiresistor sensor devices show excellent sensitivity towards NO_2 and NH_3, significantly higher than their film counterparts. The GNM sensor devices exhibit sensitivities of about 4.32%/ppm (parts-per-million) in NO_2 and 0.71%/ppm in NH_3 with estimated limit of detections of 15 ppb (parts-per billion) and 160 ppb, significantly lower than Occupational Safety and Health Administration (OSHA) permissible exposure limits of 5 ppm (NO_2) and 50 ppm (NH_3), respectively. The demonstrated studies on the sensing properties of graphene nanomesh would essentially lead further improvement of it's sensitivity and selectivity as a potential sensor material.

Furthermore, a three-dimensional (3D) carbon electrode in the form of vertically aligned carbon nanotubes (CNTs) on a graphene floor is applied as a supporting electrode for platinum (Pt) nanoflowers electrocatalysts in methanol oxidation as well as in nonenzymatic sensing of blood glucose. Experimental results demonstrate an enhanced

efficiency of the 3D graphene-carbon nanotubes hybrid film, as catalyst support, for methanol oxidation with regard to electroactive surface area, forward anodic peak current density, onset oxidation potential, diffusion efficiency and the ratio of forward to backward anodic peak current density (I_f/I_b). Also, the developed nonenzymatic 3D carbon hybrid sensor responded linearly to the physiological glucose concentration ranging from 1 to 7 mM ($R^2 = 0.978$) with a sensitivity of 11.06 μA $mM^{-1}cm^{-2}$.

Contents

List of Figures

CHAPTER 1

Literature Survey on Graphene

1.1 Graphene

Graphene is a one-atom-thick carbon atoms tightly packed into a two-dimensional (2D) hexagonal honeycomb network, and is a basic building block for all other carbon allotropes, as shown in Fig. 1.1.[1] Theoretical properties of graphene (and/or graphite) have been investigated for more than sixty years to describe various properties of carbon-based materials and their composites.[2] This strictly 2D system was believed to not exist in a free state, and to be thermodynamically unstable with respect to the formation of 0D fullerene, 1D nanotube and 3D graphite as shown in Fig. 1.1.[3] However, in 2004, a group of researchers led by A. Geim and K. Noveselov at University of Manchester experimentally isolated graphene by mechanical exfoliation of highly ordered pyrolitic graphite (HOPG), and that achievement fascinated the scientific community to study the free-standing graphene for the first time.[4] This atomically thin sheet was found to be stable under ambient conditions, exhibiting high quality and continuity on a microscopic scale.

Graphene research received a jolt in 2004 when Geim and coworkers at University of Manchester first reported the electrical properties of monolayer graphene by mechanically isolating it from highly ordered pyrolytic graphite (HOPG).[4] The scientific findings obtained on this wonder material were so remarkable that Geim and Novoselov

were awarded the Nobel Prize in Physics in 2010, within just 7 years of their first publication on this material. The studies go on to show the promise graphene carries both in fundamental science as well as technological and applied research.

Graphene is found to possess many interesting properties. Most importantly, it exhibits pronounced ambipolar electric field effect with mobilites of charge carriers exceeding 15,000-200,000 cm^2/Vs even at room temperature.[4-7] This high mobility of graphene is due to its weak dependency on temperature, which is limited only by the defect/impurity

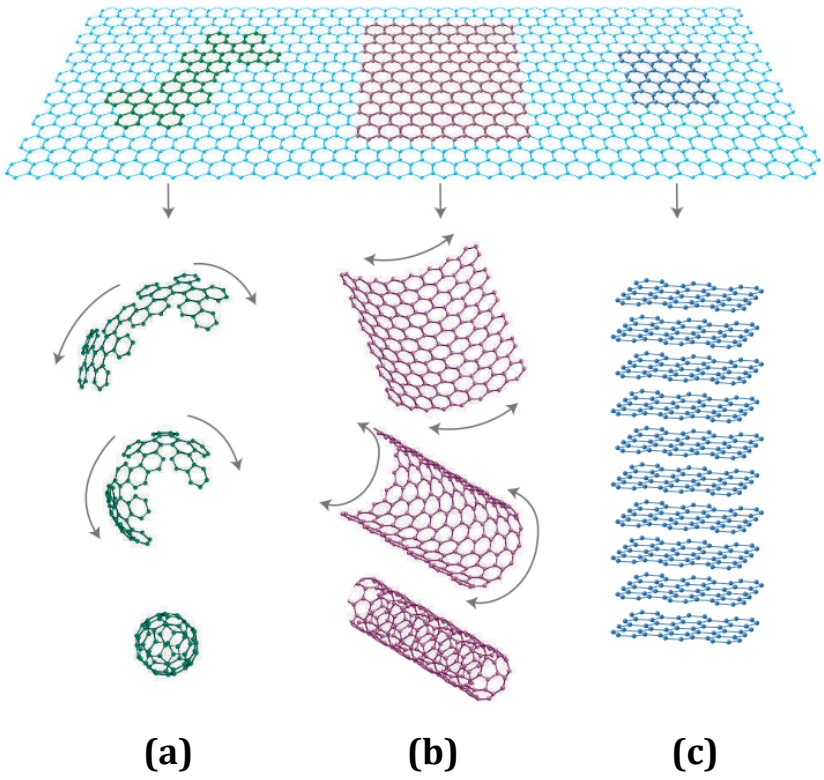

Figure 1.1 Graphene: building block for all other carbon allotorpes. It can be rolled into a) 0D buckyballs, b) 1D CNT and stacked to form c) 3D graphite.[1]

scattering. Unlike some undoped III-V semiconductors (such as indium antimonide, InSb) that exhibit room temperature mobilities of about 77,000 cm^2/Vs, the mobility of graphene remains high at high carrier concentration ($\sim 10^{12}$ cm^{-2}) in electrically or chemically doped devices resulting ballistic transport on submicron scale. Moreover, graphene is an excellent heat conductor (thermal conductivity~5000W/mK) and the strongest material ever tested, and is optically transparent (~ 97.7%) and flexible.

Due to the properties mentioned above, graphene has been considered as a promising material in variety of applications such as field-effect transistors, capacitors, energy storage, sensors, photovoltaics etc. Moreover, graphene-based composite materials exhibit high electrical conductivity and show potential in biosensing[8] as well as Li-ion batteries.[9] Graphene-based sensors show promising responses because of the dependency of electrical conductivity of grapheneon concentration of various gaseous species or bio-molecules. Graphene can be used as a transparent and flexible electrode in photovoltaics, liquid crystal displays (LCDs) and organic light emitting diodes (OLEDs).[10-12] Graphene has also been envisioned as a potential candidate to replace indium tin oxide (ITO) due to its high strength, flexibility and stretchability.

1.2 Structure of Graphene

Graphene consists of a layer of sp^2 carbon hexagonal networks, in which strong covalent bonds are formed between two adjacent carbon atoms. In the graphene lattice, two sub-lattice of carbon atoms are bonded together with σ bonds, and π orbital of each carbon atom in the lattice contribute to a delocalized network of electrons. The electronic

structure of graphene is different from typical 3D materials. Six double cones characterize the Fermi surface of graphene, as shown in Figure 1.2.

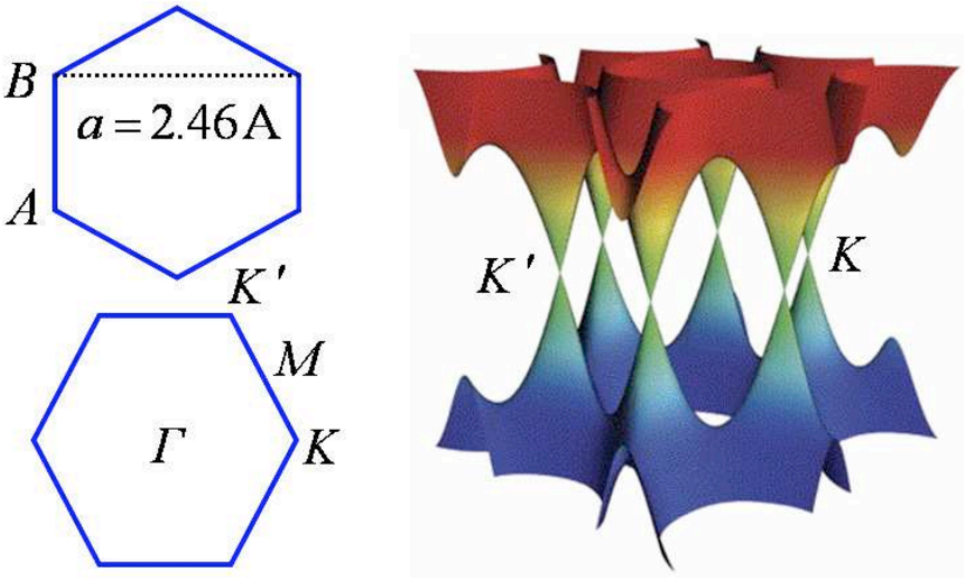

Figure 1.2 Band structure of graphene at low energies. The conduction and valence bands intersect at points K and K′. The dispersion relation is linear at those points.[13]

In intrinsic or undoped graphene, the Fermi level is situated at the contact points of these cones. Since the density of states of graphene is zero at that point, the electrical conductivity of intrinsic graphene is quite low. However, the Fermi level can be tuned by an electric field so that the graphene becomes either n- or p-doped depending on the polarity of the applied field. Graphene can also be doped by adsorbants such as water or ammonia on its surface. The electrical conductivity of doped-graphene is potentially high; at room temperature it could be higher than that of copper.

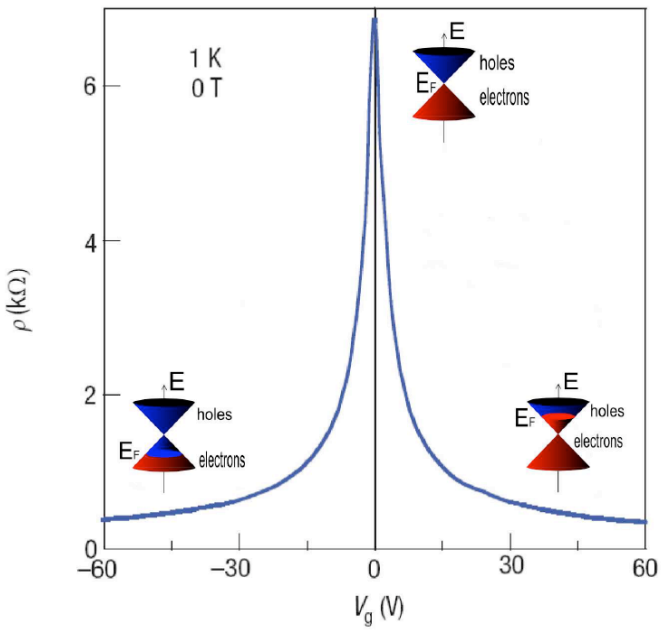

Figure 1.3 Ambipolar electric field effects in monolayer graphene. The inset cones represent low-energy spectrum E(k), indicating changes in the position of the Fermi energy (E_F) with increasing (inducing electron) or decreasing (inducing holes) gate voltage (V_g). The rapid decrease in resistivity ϱ by adding charge carriers describes their high mobility and does not noticeably change up to room temperature.[1]

The dispersion relation for electrons and holes is linear close to the Fermi level. Since the effective masses are given by the curvature of the energy bands, therefore, this corresponds to zero effective mass. The charge carriers in graphene are described with the Dirac equation instead of Schrödinger equation,[14-20] and they act like quasiparticles called massless fermions that travel at a constant speed. The contact points of these cones are therefore called Dirac points. Now, due to the low density of states near the Dirac point in graphene, a shift of the Fermi level by gating causes a significant variation of

charge density, leading to a significant change in transmission. The relaxation and recombination of photo-induced electron-hole pairs in the graphene occurs in tens of picoseconds depending on the carrier concentration of graphene.[21,22] With this high carrier transport velocity even under a moderate electrical field, the graphene FET exhibits an ultra-fast and efficient photoresponse,[23] suggesting its application high-speed optoelectronic devices for communications, detection, sensing etc.

1.3 Synthesis Methods of Graphene

Currently, there are now four primary synthesis processes, as delineated below, that have been employed to produce pristine graphene.

1.3.1 Epitaxial Graphene

In this process graphene grows on epitaxially matched surface by chemical deposition technique. Approximately 40 years ago, graphene was first experimentally determined and detailed investigations were carried out on the thermodynamics of growth of "monolayer graphite" and "bilayer graphite" on single crystalline metal surfaces.[24-27] However, due to the lack of consistency between properties of those film on different metal crystals and the limitation of finally identifying the proper application of those films, this process was not studied that extensively. A more recently implemented technique to grown epitaxial graphene is, to grow large area epitaxial graphene on SiC substrate. In this process graphene formation is initiated by the sublimation of Si atoms and the formation carbon-segregated surface containing mobile carbon atoms, during the

annealing at >1300°C in ultra-high vacuum or atmospheric pressure.[28-30] Diffusion of those carbon atoms on the surface at that high temperature produces layer of a wafer scale large area epitaxial graphene film with a mobility of 2000 $cm^2V^{-1}S^{-1}$.[31] Large area monolayer growth has also been performed on Cu foils. The size of the graphene could be as large as possible and is synthesized by simply exposing a large metal foils to carbon precursor to form either monolayer or multilayer graphene films. Further, this method provides the feasibility of transfering a large area graphene film onto any arbitrary substrate due to the fact that graphene film can be extracted by etching the underneath metals. This method is envisioned as the eventual solution for large area epitaxial graphene growth. Direct growth of graphene on dielectric surfaces is an another technological interest that would be beneficial for field-effect transistors or related devices in nanoelectronics.

1.3.2 Mechanical Exfoliation of Graphite

Even though it has been recognized that carbon segregates in the form of graphitic layers on transition metal surfaces, until 2004, no detailed reports were published on their electronics properties probably due to the fact that the substrates were all metallic and no attempts were performed to transfer them on insulating/dielectric substrates. In 2004, Geim and coworkers published first report[4] on the electronic properties of graphene. They first mechanically isolated mono/few layers graphene from HOPG and transferred it on SiO_2/Si substrate that allowed them to fabricate graphene transistor devices. Since then, mechanical exfoliation method received an immediate attention as a reliable method for

obtaining monolayer graphene flakes on foreign substrates. This method involves isolating graphene flakes from HOPG block by repeated peeling/exfoliation using different techniques such as scotch tape,[4] ultrasonication[32], transfer printing technique[33,34] etc. The technique was also used to produce 2D atomic crystals of many other materials such as BN and MoS_2. It is the cheapest technique that has been used so far to produce high quality monolayer graphene flakes. However, locating a monolayer graphene flake is tedious and the yield of mono/few layer graphene obtained by this technique is very poor and the flakes are randomly distributed on the substrate. The resulting graphene flakes are very small which is about few microns to a millimeter in size. Thus mechanical exfoliation technique is so far practiced only to study graphene in a lab scale, and is not scalable to a commercial level.

1.3.3 Reduced Graphene Oxide

In this method, graphene platelets are prepared from dispersions of graphene oxide platelets made from graphite oxide (GO). In general, GO is synthesized by modified Brodie,[35] Staudenmaier,[36] or Hummers methods.[37] All these methods involve oxidation of graphite to GO. Brodie and Staudenmaier methods involve a combination of potassium chlorate ($KClO_3$) with nitric acid (HNO_3) to oxidize graphite, while the Hummers method involves a combination of potassium permanganate ($KMnO_4$) and sulfuric acid (H_2SO_4) treatment to oxidize graphite. GO is highly hydrophilic due to the existence of polar oxygen functional groups of GO during the oxidation. Thus, it is easy to exfoliate GO in many solvents, and disperse it particularly well in water.[38] GO platelets

can be easily disintegrated into graphene oxide by stirring and sonication of GO in either in water or various organic solvents. After that, the colloidal dispersion of graphene oxide can be reduced to graphene sheets using several reducing agents such as hydrazine,[39] hydroquinone,[40] sodium borohydride ($NaBH_4$),[41,42] and ascorbic acid.[43] Reduction of graphene oxide using thermal treatment[44,45] in reducing atmosphere or electrochemical method has also been considered as an efficient and low cost method.[44-46] Reduced graphene oxide has been shown to have promising potential in various applications, such as transparent conductive electrodes, graphene-based polymer composites, sensors, capacitors etc. However, these chemically modified graphene sheets still contains oxygen functional groups and other impurities due to the lack of complete reduction of graphene oxide, which limit their application in many other areas of nanoelectronics.

1.3.4 Chemical Vapor Deposition (CVD) of Graphene

As discussed earlier, graphene can be grown on metal surfaces by carbon segregation on the surface or by hydrocarbon decomposition at elevated temperature. This process is similar to epitaxial graphene metallic single crystals. However, CVD-grown graphene on metallic films or foils require relatively higher growth pressure than epitaxially grown graphene. This technique has been considered practical for large area graphene production because of the availability of large metallic substrate in the form of thin films or foils. However, these metallic films/foils are polycrystalline in nature, and thus the individual grains are oriented in different directions forming grain boundaries as opposed to epitaxial metallic surface. Thus, carbon segregation occurs relatively higher in

grain boundaries as they are thermodynamically in higher energy states in a polycrystalline material, and thus grain boundaries are the regions where graphene grows in higher thickness. CVD growth of graphene was performed on various metallic substrates, but

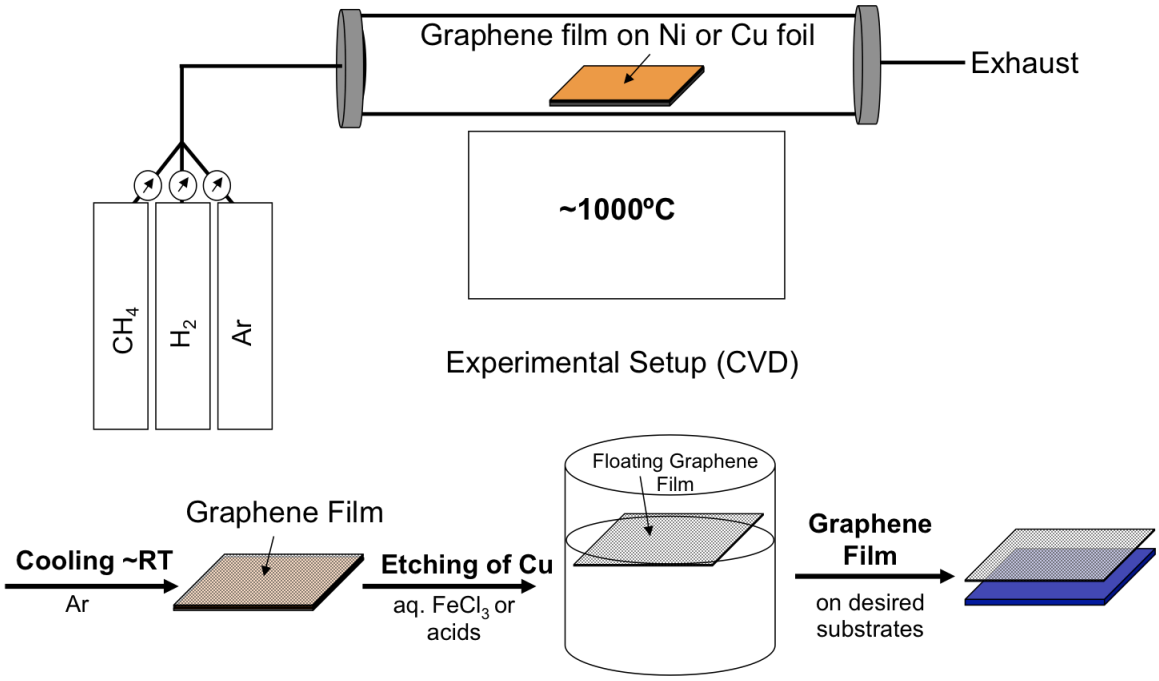

Figure 1.4 A schematic representation of the steps involved to synthesis larger area graphene film using CVD technique.

mostly practiced ones are nickel (Ni)[47-49] and copper (Cu).[50,51] Fig. 1.4 shows a schematic diagram of typical CVD setup and the steps involved to synthesize large area graphene on Ni or Cu substrates. In a typical growth process, at first, the Ni or Cu foil is inserted in a tube furnace as shown in Fig. 1.4. The temperature of the furnace is then raised to ~1000°C in flowing Ar/H_2 atmosphere under low or atmospheric pressure to anneal the

foil. The individual grains of Ni or Cu grow bigger during annealing, which eventually decreases the density of defects (wrinkles, folds, impurities etc.) in the resulting graphene film. After annealing for a certain period of time, CH_4, as a carbon precursor, is supplied to deposit carbon on Ni or Cu foil. CH_4 flow is switched off once the growth is done, and cooling of the furnace is performed for carbon segregation on the surface to form graphene film. Finally, Ni or Cu foil is etched away in aqueous $FeCl_3$ solution to allow graphene floating on the surface of etching solution. After subsequent cleaning, the graphene film is then transferred on desired substrate. The growth mechanisms of graphene are different on different metal substrates. In last few years, several reports have been published on CVD growth of graphene on various metal substrates, and this process is still in its way to provide high quality single crystal of large area graphene.

1.4 CVD Growth Mechanisms of Graphene

Mono/few-layer large area graphene films were first grown on polycrystalline Ni substrate by CVD of methane (CH_4) by controlling the growth time and cooling rate of the metal substrates to suppress the amount of C precipitation during the growth process.[47,48,52] These reports immediately attracted remarkable interest in CVD synthesis of graphene. Since then, many reports have been published exploring the controlled growth parameter to improve the quality of graphene film. However, the major drawback of using Ni substrate for graphene growth is that the solubility of C in Ni is relatively high. Thus, it is difficult to suppress C precipitation completely and therefore the resulting graphene films can vary from monolayer to few layers. In this case, the

thickness of graphene film strictly depends on the exposure time of Ni substrate to carbon precursor, the cooling rate and the thickness of Ni substrate. Moreover, large number of wrinkles and folds appear in these films due to the difference in thermal expansion coefficients between graphene and Ni, and defect nucleation at the step edges/grain boundaries on Ni surface. However, large-area graphene films with about 95% as monolayer graphene were grown on Cu foils by CVD of CH_4 by taking advantage of the very low solubility of C in Cu.[51] It has been shown that graphene growth on Cu surface is a surface-mediated process, and the process is self-limiting; that is, once the Cu surface was fully covered with graphene, the growth process gets terminated; also it is possible to achieve 100% monolayer graphene.[53] Graphene films grown on Cu substrates also are high quality with carrier mobilities typically in the range 2000 to 4000 $cm^2V^{-1}s^{-1}$. These values are lower than those of exfoliated graphene flakes from HOPG. Thus, continuous improvements are being performed on CVD grown graphene in terms of synthesis, and successful transfer of large area monolayer graphene onto foreign substrates.

1.5 Characterization of Graphene

Graphene is usually characterized by optical microscopy (OM), Raman spectroscopy, atomic force microscopy (AFM) and transmission electron microscopy (TEM). Using TEM, the number of graphene layers can be counted in atomic scale. Also, TEM could provide information about the crystalline quality of the synthesized graphene film by electron diffraction patterning technique. TEM image in the inset of Fig. 1.5a, clearly shows monolayer (avg. thickness ~ 0.34 nm) and bilayer graphene films. One of

the widely employed methods of identifying monolayer graphene is through optical microscopy (OM) because this technique is non-destructive and quick testing. Depending on the thickness (comprised of number of layers), graphene film exhibits a characteristic color contrast on a thermally grown SiO_2 (300nm)/Si substrate as shown Fig. 1.5 b. AFM analysis is also a frequently used technique to verify thickness of graphene transferred onto any arbitrary substrates, leading to identification of the number of layers.

Raman spectroscopy is another popular method, and is considered the non-destructive, quickest and most precise method to identify the thickness of graphene film together with its crystalline quality. This is because graphene exhibits characteristic Raman spectra based on the number of layers and density of defects as shown in Fig. 1.5 d, taken from the regions (colored circles) in Fig. 1.5 a and b, corresponding to the number of layers in the Raman spectra in Fig. 1.5d.

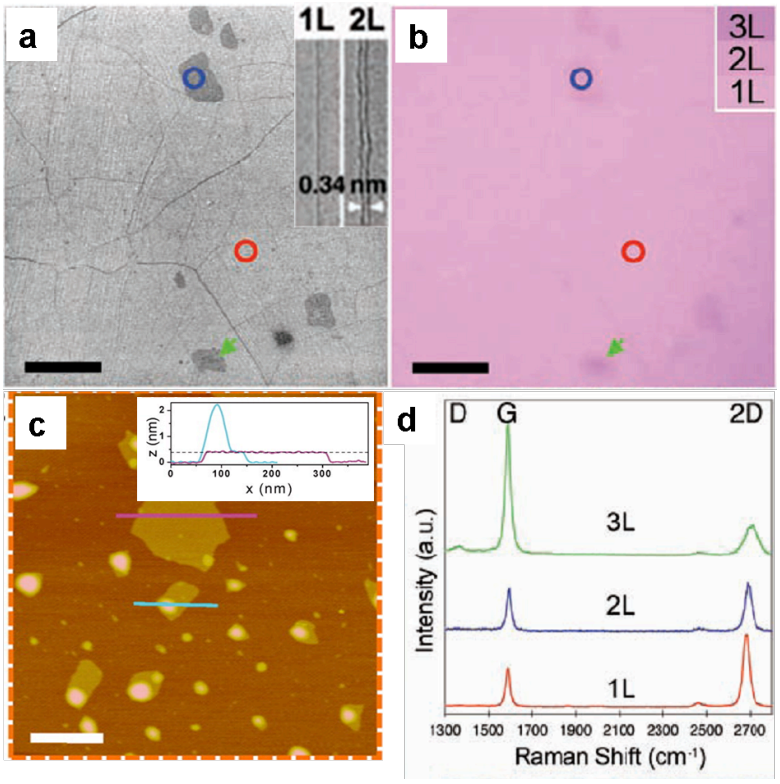

Figure 1.5 a) SEM, b) OM and c) AFM images and Raman spectra of graphene films.[51,54]

The main signatures of the Raman spectra of graphite or graphene are the G band at ~1584 cm^{-1} and the 2D band at ~2700 cm^{-1}. The G band is due to the E2g vibrational mode, and the 2D band is a second-order two-phonon mode. A third feature, the D band at ~1350 cm^{-1}, is not Raman active for pristine graphene but usually appears if the symmetry is broken by edges or due to a high density of defects. The relative peak heights of the G and 2D bands indicates the number of layers present for a given graphene film. The location of the G peak for monolayer graphene situates at 3-5cm^{-1} higher than that for bulk graphite while its intensity is roughly the same. The 2D peak shows a significant change in both shape and intensity as the number of layers is decreased. For monolayer graphene, the 2D band is a single sharp peak at the lower shift,

with intensity about two times the intensity of the G peak. As the number of layers increases the relative 2D peak intensity decreases compared to that for D peak as shown Fig. 1.5d.

1.6 Bandgap Engineering of Graphene

Graphene exhibits promising properties desired for future transistor applications, and therefore this material has been envisioned as a potential candidate to replace silicon. However, the major drawback of graphene for transistor application is its zero bandgap. Due to such band structure, graphene based FETs usually show low I_{ON}/I_{OFF} ratio. Since its discovery one of the major focuses in graphene research has been on finding a technique to open up a band gap in graphene without compromising on any of its other properties. Several techniques have been practiced so far such as substrate induced bandgap opening,[55] chemical substitution doping with various elements,[56-61] quantum confinement of charge carriers in graphene etc. The above mentioned techniques other than quantum confinement of charge carriers have been experimentally successful to quite an extent in opening up a finite band gap in graphene, and thereby improving I_{ON}/I_{OFF} ratio in graphene based switching devices. However a major drawback with most of these methods is that the carrier mobility is significantly reduced affecting the ultimate device performance. But quantum confinement of charge carriers in graphene on the other hand does not affect the carrier mobility to a great extent. Therefore, quantum confinement of graphene by laterally reducing the dimension of graphene at a nanometer scale has been investigated extensively to open up a bandgap in a monolithic graphene

film.

1.6.1 Quantum Confinement of Charge Carriers: Graphene Nanoribbons (GNRs) and Graphene nanomesh (GNMs)

As mentioned above, graphene, a zero band gap material, has showed remarkable promises for applications in future nanoelectronic devices. Charge transport in graphene is different from that of conventional 2D electronic systems due to its linear energy dispersion relation near the Dirac point in the electronic band structure. However, its practical applications cannot be effectively realized unless a finite bandgap is opened up in its electronic structure. It has already been recognized that when graphene is processed into a narrow ribbon called GNRs, the carriers are confined to a quasi-one-dimensional system, resulting in an introduction of finite energy gap.[62] Similar to the case of CNTs, the energy gap depends on the width and the chirality of a CNT.[63,64] The GNRs were theoretically investigated by Mitsutaka Fujita and coauthors to examine the edge and nanoscale size effect in graphene.[63-65] Since no impurities are being introduced in the graphitic lattice no charge scattering would occur except at the edges, and therefore the carrier mobility will not be significantly reduced in a GNR. Thus, GNR with a width less than 10 nm possesses large enough bandgap together with high carrier mobility, leading to high I_{ON}/I_{OFF} ratio while being used as transistor channel.[62] This all-semiconducting property of sub-10 nm GNRs could then by pass the problem of the chirality dependence of electronic properties observed in SWNTs, and thus make GNR an ideal candidate for nanoelectronics. Metallic GNRs are also ideal candidates as conductive interconnects

than CNTs since they have extremely high current carrying capacity. However, controlled and scalable synthesis of GNRs is very difficult at this point.

One of the alternatives is to drill nanohole superlattice in large area graphene. Recent theoretical studies in such systems, followed by experimental demonstration of the same have attracted significant interest in this area.[66-71] This work reported producing GNMs from graphene by conventional block copolymer lithography. The neck formed between two nanoholes acts as a nanoribbon to confine the charge carriers passing through it. By simply changing the hole diameter and density, the neck-width can be controlled to tune the bandgap of graphene. Moreover, these GNMs transistor devices show high drive currents or transconductances compared to those of GNRs devices, exhibiting a I_{ON}/I_{OFF} ratio of about 100.[71]

1.7 Graphene-Based Gas Sensor

The field of sensors covers a wide variety of materials and devices used for capturing physical, chemical or biological stimuli, and converting them to measurable output signals. Nanomaterials has been used as active sensing elements or receptors, as transducing components (e.g. electro- or chemo-mechanical actuators), and even as electrodes in electronic circuitry and power systems (e.g. nanowires).[72,73]

In general, gas adsorption on the surface of a sensor material is fundamental to the resistive gas detection process. Thus, reduction of the dimension of sensor materials to the nanoscale therefore increases their surface-to-volume ratio, resulting a significant fraction of the atoms is exposed at the surface to participate in the surface reactions.

Thus, nanomaterials have the obvious effect of improving gas sensitivity while being used in sensor devices. On the other hand, the Debye length λ_D, a measure of the field penetration into the bulk, for most nanomaterials (such as nanowires and nanotubes) is comparable to their extremely narrow dimensions/radius that results their electronic properties to be strongly modulated by the processes at their surface. This basically leads a sensor exhibiting improved sensitivity and selectivity. Several reports in the literature have documented several orders of magnitude enhancements in the gas sensing response of nanomaterials compared to their bulk counterparts.[72,74] The response and recovery time of nanomaterials-based chemiresistors would be impressively as low as milliseconds.[72-74] The electronic properties of graphene are strongly modulated by the adsorption of molecules,[75] a prerequisite for an electrically based sensor. The high sensitivity of graphene emerges due to two primary reasons: (1) the 2D nature of graphene allows total exposure of all of its surface carbon atoms to the adsorbed gas molecules, providing the high surface area per unit volume,[76] and (2) it is inherently a low-noise material due to the quality of its crystal lattice, which leads to screen charge fluctuations more than one-dimensional systems such as carbon nanotubes. Beyond the electronic properties, graphene has other practical advantages for making sensors, such as ease of making devices using conventional lithographic techniques and the good long-term stability of the material.[77-79] The potential use of graphene as gas sensing elements has been well realized in a multi-terminal Hall bars device, where the detection of the single gas molecule adsorbed on its surface was achieved.[79] After that, significant efforts have been undertaken to improve sensitivity and selectivity of graphene-based gas sensor devices

upon exposure to various gaseous species.

1.8 Graphene-CNTs Hybrid

Carbon allotropes such as graphite, diamond, fullerenes, and nanotubes have their distinct structures and properties, which lead them to various commercial applications. In the last few decades, several unique micro- and/or nanostructures composed of different carbon allotropes including a composite of CNTs and fullerene, have been discovered.[80] CNT is a unique allotrope of carbon, formed by rolling up single sheet of graphene into individual tubes. Their shape and nanostructure give them an unusually high specific surface area (SSA), high current density and extremely high thermal conductivity, which may lead to widespread applications such as interconnects for large scale integrated circuit, thermal bumps and thermal interface materials, sensors and different electrode systems.[81-84] On the other hand, graphene, one atom thick 2D honeycomb lattice of sp^2-bonded carbon atoms, has unique band structure, band-tuning ability, extremely high carrier mobility, high thermal transport properties as well as high chemical stability.[4,85] Thus, graphene nanostructures have been envisioned as promising materials for their potential applications as electrodes materials in sensors, supercapacitors, batteries and photovoltaics. However, those excellent properties emerge in the axial direction for CNTs and in the planar direction of graphene. Therefore, a bundle of CNTs show poor physical properties in the directions perpendicular to the tube axis. However, a composite material consisting of CNTs and graphene could be an excellent choice, which combines the unique properties of two carbon allotropes in all directions.

Furthermore, the major requirements of an electrode material to be used in supercapacitors, batteries, fuel cells or photovoltaics are: low material costs and easy fabrication process, high electrochemical reactivity and fast redox reaction, high electrical conductivity (comprised of high power density) and high specific surface area (comprised of high energy density). Graphene/CNTs composites would provide all those necessary properties due to it unique architecture that is ideal for an extremely high SSA electrode material.

1.9 Graphene-Based Methanol Fuel Cells

Direct methanol fuel cells (DMFCs) have been considered as promising power sources for automobiles and portable electronic devices, employing hydrogen proton exchange membrane electrolytes to convert chemical energy of the fuel directly into electricity with no harmful emissions. Although the operating principle of the fuel cell is similar to that of conventional battery, fuel cell requires continuous supply of the fuel and oxidant from external sources to produce electricity. The methanol is usually diluted with water, less than 2M, for better fuel efficiency.[86-89]

The anode consumes methanol with water supplied to produce hydrogen (H^+) ions and CO_2:

$$CH_3OH + H_2O \rightarrow CO_2 + 6H^+ + 6e^-$$

and the hydrogen ions (H^+) reacts with oxygen on cathode and produces water as the reaction product:

$2O_2 + 2H^+ + 2e^- \rightarrow H_2O$

However, the successful commercialization of DMFCs depends on the activity and durability of electrocatalyst involving the oxidation of methanol as well as the reduction of oxygen.[90-92] At present, almost all pre-commercial low-temperature DMFCs use supported platinum (Pt) or Pt-alloys as their electrocatalyst. The critical parameters for an electrocatalyst include electrical conductivity, surface area, morphology, micro/nanostructure, corrosion resistance and cost. The reduction of the amount of Pt catalyst used can be achieved using high-surface-area carbon supports such as CNTs, fullerenes, graphene, etc., which generally enable the effective utilization of Pt catalysts.[91-94]

Besides the superior electrical conductivity and outstanding mechanical properties, as a one-carbon atom-thick material, graphene has a high surface-to-volume ratio and a theoretical mass-specific surface area up to 2630-2965 m^2/g.

This surface-to-mass ratio is much larger than that of other carbon materials such as CNTs, carbon black, etc.[95,96] Therefore, graphene has a unique advantage as a supporting platform for use of catalytic metallic materials to electro-oxidize methanol compared to other nanomaterials such as carbon black, CNTs, carbon nanofibers (CNFs), CNx nanotube etc.[98-103]

Graphene/CNTs composites could be an excellent choice as an electrode material for methanol fuel cell. The vertical orientation of CNTs connected to the large-area graphene floor enables: (a) the ballistic transport of charge carriers through 1D CNTs and

their collection through the high carrier mobility 2D graphene floor, and (b) high surface-to-volume ratio to achieve enhanced current density. Combining these two carbon allotropes with their outstanding electronic conductivity, graphene/CNTs composites could be a potential candidate as an excellent electrochemical test bed to study surface interactions and dynamics. Thus, a graphene/CNTs composite is chosen as a novel electrode system for mediating the metal catalytic electro-oxidation of methanol. The catalytic properties of such composites and their hybrids are studied and compared with other electrode systems with the aim of optimizing various factors such as different precious metal loading, high current density, and fast mass and electron transport rate such etc.

1.10 Objective of the Work

- Develop low cost chemical vapor deposition (CVD) technique for synthesis of large area graphene.
- Synthesis of large area graphene nanomeshes (GNMs) by the combination of CVD and nanosphere lithography techniques.
- To investigate the gas sensing properties/mechanism of GNMs sensor devices.
- Application of graphene/CNTs composite structure and its hybrid as electrode materials in methanol fuel cells and non-enzymatic glucose sensor.

The morphology, crystal structure and electrical characteristics of CVD-synthesized large area graphene are investigated depending on the process conditions. A simple reactive ion etching (RIE) combined with well-established nanosphere lithography is

performed on the synthesized CVD-grown monolayer graphene platform to fabricate large area GNMs with specific dimension and periodicity. The gas sensing mechanism of fabricated GNMs chemiresistor sensor devices is evaluated by exposing them to electron-withdrawing NO_2 and electron-donating NH_3 gas molecules. Furthermore, a graphene-based hybrid nanostructure, which is a combination of two carbon allotropes such as graphene and carbon nanotubes, is applied in methanol fuel cells and sensing of blood glucose.

1.11 Organization of the Thesis

Chapter 2 discusses CVD-synthesis and characterization of large area graphene using ethanol as a carbon precursor. Chapter 3 describes patterning of CVD-graphene into graphene nanomesh (GNM) using reactive ion etching and nanosphere lithography techniques. Chapter 4 presents gas-sensing properties/mechanisms of GNMs sensor devices in various gas molecules. Chapter 5 discusses the electrocatalytic activity of platinum (Pt) nanoflower decorated PGN in methanol oxidation. At last, concluding remarks of this dissertation along with suggestions for future work are presented in chapter 6.

1.12 References

1. Geim, A.K.; Novoselov, K.S. Nat. Mater. 2007, 6, 183.

2. Wallace, P.R. Phys. Rev. 1947, 71, 622.

3. Mermin, N.D. Phys. Rev. 1968, 176, 250.

4. Novoselov, K.S.; Geim, A.K.; Morozov, S.V.; Jiang, D.; Zhang, Y.; S. V. Dubonos, S.V.; Grigorieva, I.V.; Firsov, A.A. Science, 2004, 306, 666.

5. Morozov, S.V.; Novoselov, K.S.; Katsnelson, M.I.; Schedin, F.; Elias, D.C.; Jaszczak, J.A.; Geim, A.K. Phys. Rev. Lett. 2008, 100, 016602.

6. Bolotin, K.I.; Sikes, K.J.; Jiang, Z.; Klima, M.; Fudenberg, G.; Hone, J.; Kim, P.; Stormer, H.L. Solid State Commun. 2008, 146, 351.

7. Dean, C.R.; Young, A.F.; Meric, L.; Lee, C.; Wang, L.; Sorgenfrei, S.; Watanabe, K.; Taniguchi, T.; Kim, P.; Shepard, K.L.; Hone, J.; Nat. Nano. advance online publication, 2010.

8. Hong, W.; Bai, H.; Xu, Y.; Yao, Z.; Gu, Z.; Shi, G. J. Phys. Chem. 2010, C 114 (4), 1822.

9. Choi, D.; Wang, D.; Viswanathan, V.V.; Bae, I.T., Wang, Nie, W.Z.; Zhang, J.G.; Graff, G.L.; Liu, J.; Yang, Z.; Duong, T. Electrochem. Commun. 2010, 12, 378.

10. Gomez De Arco, L.; Zhang, Y.; Schlenker, C.W.; Ryu, K.; Thompson, M.E.; Zhou, C. ACS Nano, 2010, 4, 2865-73.

11. Li, X.S.; Zhu, Y.W.; Cai, W.W.; Borysiak, M.; Han, B.Y.; Chen, D.; Piner, R.D.; Colombo, L.; Ruoff, R.S. Nano Lett . 2009, 9 (12), 4359.

12. Blake, P.; Brimicombe, P.D.; Nair, R.R.; Booth, T.J.; Jiang, D.; Schedin, F.; Ponomarenko, L.A.; Morozov, S.V.; Gleeson, H.F.; Hill, E.W.; Geim, A.K.; Novoselov, K.S. Nano Lett. 2008, 8 (6), 1704.

13. Katsnelson, M.I., Materials Today, 2007, 10, 20.

14. Semenoff, G. W. Phys. Rev. Lett. 1984, 53, 2449-2452.

15. Fradkin, E. Phys. Rev. B, 1986, 33, 3263-3268.

16. Schakel, A. M. J. Phys. Rev. 1991, D 43, 1428-1431.

17. González, J.; Guinea, F.; Vozmediano, M. A. H. Phys. Rev. Lett. 1996, 77, 3589-3592.

18. Katsnelson, M. I.; Zitterbewegung. Eur. Phys. J. 2006, B 51, 157-160.

19. Katsnelson, M. I; Novoselov, K. S.; Geim, A. K. Nature Phys. 2006, 2, 620-625.

20. Tworzydlo, J.; Trauzettel, B.; Titov, M.; Rycerz, A.; Beenakker, C. W. J.; Phys. Rev. Lett. 2006, 96, 246802.

21. George, P.A.; Strait, J.; Dawlaty, J.; Shivaraman, S.; Chandrashekhar, M.; Rana, F.; Spencer, M.G. Nano Lett. 2008, 8, 4248.

22. Rana, F.; George, P.A.; Strait, J.H.; Dawlaty, J.; Shivaraman, S.; Chandrashekhar, M.; Spencer, M.G.; Phys. Rev. B, 2009, 79, 115447.

23. Xia, F.; Mueller, T.; Lin, Y.M.; Valdes-Garcia, A.; Avouris, P. Nat. Nanotechnol. 2009, 4, 839.

24. Shelton, J.C.; Patil, H.R.; Blakely, J.M. Surf. Sci. 1974, 43, 493.

25. Eizenberg, M.; Blakely, J.M. J. Chem. Phys. 1979, 71, 3467.

26. Eizenberg, M.; Blakely, J.M. Surf. Sci. 1979, 82, 228.

27. Hamilton, J.C.; Blakely, J.M. Surf. Sci. 1980, 91, 119.

28. Berger, C.; Song, Z.M.; Li, T.B.; Li, X.B.; Ogbazghi, A.Y.; Feng, R.; Dai, Z.T.; Marchenkov, A.N.; Conrad, E.H.; First, P.N.; De Heer, W.A. J. Phys. Chem. B, 2004, 108, 19912.

29. Berger, C.; Song, Z.; Li, X.; Wu, X.; Brown, N.; Naud, C.; Mayou, D.; Li, T.; Hass, J.; Marchenkov, A.N.; Conrad, E.H.; First, P.N.; de Heer, W.A. Science, 2006, 312, 1991.

30. de Heer, W.A.; Berger, C.; Wu, X.; First, P.N.; Conrad, E.H.; Li, X.; Li, T.; Sprinkle, M.; Hass, J.; Sadowski, M.L.; Potemski, M.; Martinez, G. Solid State Commun. 2007, 143, 92.

31. Emtsev, K.V.; Bostwick, A.; Horn, K.; Jobst, J.; Kellogg, G.L.; Ley, L.; McChesney, J.L.; Ohta, T.; Reshanov, S.A.; Rohrl, J.; Rotenberg, E.; Schmid, A.K.; Waldmann, D.; Weber, H.B.; Seyller, T. Nat. Mater. 2009, 8, 203.

32. Ci, L.J.; Song, L.; Jariwala, D.; Elias, A.L.; Gao, W.; Terrones, M.; Ajayan, P.M. Adv. Mater. 2009, 21, 4487.

33. Liang, X.; Fu, Z.; Chou, S.Y. Nano Lett. 2007, 7, 3840.

34. Chen, J.H.; Ishigami, M.; Jang, C.; Hines, D.R.; Fuhrer, M.S.; Williams, E.D. Adv. Mater. 2007, 19, 3623.

35. Brodie, B.C.; Ann. Chim. Phys. 1860, 59, 466.

36. Staudenmaier, L. Ber. Deut. Chem. Ges. 1898, 31, 1481.

37. Hummers, W.S.; Offeman, R.E.; J. Am. Chem. Soc. 1958, 80, 1339.

38. Paredes, J.I.; Villar-Rodil, S.; Martinez-Alonso, A.; Tascon, J.M.D. Langmuir, 2008, 24, 10560.

39. Stankovich, S.; Dikin, D.A.; Piner, R.D.; Kohlhaas, K.A.; Kleinhammes, A.; Jia, Y.; Wu, Y.; Nguyen, S.Y.; Ruoff, R.S. Carbon, 2007, 45, 1558.

40. Wang, G.X.; Yang, J.; Park, J.; Gou, X.L.; Wang, B.; Liu, H.; Yao, J. J. Phys. Chem. C, 2008, 112, 8192.

41. Si, Y.; Samulski, E.T. Nano Lett. 2008, 8, 1679.

42. Shin, H.J.; Kim, K.K.; Benayad, A.; Yoon, S.M.; Park, H.K.; Jung, I.S.; Jin, M.H.; Jeong, H.K.; Kim, J.M.; Choi, J.Y.; Lee, Y.H. Adv. Funct. Mater. 2009, 19, 1987.

43. Dua, V.; Surwade, S.P.; Ammu, S.; Agnihotra, S.R.; Jain, S.; Roberts, K.E.; Park, S.; Ruoff, R.S.; Manohar, S.K.; Angew. Chem. Int. Ed. 2010, 122, 2200.

44. McAllister, M.J.; Li, J.L.; Adamson, D.H.; Schniepp, H.C.; Abdala, A.A.; Liu, J.; Herrera-Alonso, M.; Milius, D.L.; Car, R.; Prud'homme, R.K.; Aksay, I.A.; Chem. Mat. 2007, 19, 4396.

45. Schniepp, H.C.; Li, J.L.; McAllister, M.J.; Sai, H.; Herrera-Alonso, M.; Adamson, D.H.; R. K. Prud'homme, R.K.; Car, R.; Saville, D.A.; Aksay, I.A.; J. Phys. Chem. B, 2006, 110, 8535.

46. Zhou, M.; Wang, Y.L.; Zhai, Y.M.; Zhai, J.F.; Ren, W.; Wang, F.A.; Dong, S.J. Chem. Eur. J. 2009, 15, 6116.

47. Reina, A.; Jia, X.; Ho, J.; Nezich, D.; Son, H.; Bulovic, V.; Dresselhaus, M.S.; Kong, J. Nano Lett. 2008, 9, 30.

48. Kim, K.S.; Zhao, Y.; Jang, H.; Lee, S.Y.; Kim, J.M.; Kim, K.S.; Ahn, J.H.; Kim, P.; Choi, J.Y.; Hong, B.H. Nature, 2009, 457, 706.

49. Yu, Q.; Lian, J.; Siriponglert, S.; Li, H.; Chen, Y.P.; Pei, S.S. Appl. Phys. Lett. 2008, 93, 113103.

50. Wei, D.; Liu, Y.; Wang, Y.; Zhang, H.; Huang, L.; Yu, G. Nano Lett. 2009, 9, 1752.

51. Li, X.S.; Cai, W.W.; An, J.H.; Kim, S.; Nah, J.; Yang, D.X.; Piner, R.; Velamakanni, A.; Jung, I.; Tutuc, E.; Banerjee, S.K.; Colombo, L.; Ruoff, R.S. Science, 2009, 324, 1312.

52. Yu, Q.K.; Lian, J.; Siriponglert, S.; Li, H.; Chen, Y.P.; Pei, S.S. Appl. Phys. Lett. 2008, 93, 113103.

53. Li, X.S.; Cai, W.W.; Colombo, L.; Ruoff, R.S.; Nano Lett. 2009, 9, 4268.

54. Xu, K,; Cao, P.; Heath, J.R. Science, 2010, 329, 1188-1191.

55. Kawasaki, T. Surf. Rev. Lett. 20022, 9, 1459.

56. Wei, D.; Liu, Y.; Wang, Y.; Zhang, H.; Huang, L.; Yu, G. Nano Lett. 2009, 9, 1752.

57. Panchakarla, L.S.; Subrahmanyam, K.S.; Saha, S.K.; Govindaraj, A.; Krishnamurthy, H.R.; Waghmare, U.V.; Rao, C.N.R. Adv. Mater. 2009, 21, 4726.

58. Yu, S.S.; Zheng, W.T.; Wen, Q.B.; Jiang, Q. Carbon, 2008, 46, 537.

59. Li, Y.; Zhou, Z.; Shen, P.; Chen, Z.; ACS Nano, 2009, 3, 1952.

60. Cervantes-Sodi, F.; Csányi, G.; Piscanec, S.; Ferrari, A.C.; Physical Review B, 2008, 77, 165427.

61. Li, N.; Wang, Z.; Zhao, K.; Shi, Z.; Gu, Z.; Xu, S.; Carbon, 2010, 48, 255.

62. Li, X.; Wang, X; Zhang, L.; Lee, S.; Dai, H. Science, 2008, 319, 1229-1232.

63. Nakada, K.; Fujita, M.; Dresselhaus, G.; Dresselhaus, M.S. Phys. Rev. B, 1996, 54, 17954.

64. Wakabayashi, K.; Fujita, M.; Ajiki, H.; Sigrist, M. Phys. Rev. B, 1999, 59, 8271.

65. Fujita, M, Wakabayashi, K.; Nakada, K.; Kusakabe, K. J. Phys. Soc. Jpn. 1996, 65, 1920.

66. Liu, W.; Wang, Z.F.; Shi, Q.W.; Yang, J.; Liu, F. Phys. Rev. B, 2009, 80, 233405.

67. Pedersen, T.G.; Flindt, C.; Pedersen, J.; Mortensen, N.A.; Jauho, A.P.; Pedersen, K. Phys. Rev. Lett. 2010, 100, 136804.

68. V. Nenad, V. et al. Phys. Rev. B, 2010, 81, 041408.

69. Fürst, J.A. et al. New Journal of Physics 11 (9), 095020 (2009)

70. J. Eroms, J.; Weiss, D. New Journal of Physics, 2009, 11, 095021.

71. Bai, J.; Zhong, X.; Jiang, S.; Huang, Y.; Duan, X.; Nat. Nanotech. 2010, 5, 190.

72. Gouma, P. Nanomaterials for Chemical Sensors and Biotechnology, Pan Stanford Publishing, 2009.

73. Gouma, P; Kubinski, D.; Comini, E. Guidi, V. Materials Research Society, Warrendale, PA, Spring 2006.

74. Shen, G.; Chen, P.C.; Ryu, K.; Zhou, C. J. Mater. Chem. 2009, 19, 828-839, 2009.

75. Y.M. Lin, Ph. Avouris., Nano Lett., **8**, pp. 2119-2125 (2008).

76. F. Schedin, K.S. Novoselov et al., Nat. Mater., **6**, pp. 652-655 (2007).

77. Q.H. Shao, D. Yan et al, IEEE Electr. Device L., **30**, pp. 288-290
(2009).

78. C. Berger, A. Walt de Heer et al., Journal of Physical Chemistry B, **108**, pp. 19912-

19916 (2004).

79. Schedin, F.; Geim, A.K.; Morozov, S.V.; Hill, E.W.; Blake, P; Katsnelson, M.I.; Novoselov, K.S. Nat. Mater. 2007, 6, 652 – 655.

80. Smith, B.W.; Monthioux, M.; Luzzi, D.E. Nature, 1998, 396, 323.

81. Z. Yao, Z.; Kane, C.L.; Dekker, C. Phys. Rev. Lett. 2000, 84, 2941.

82. Kim, P.; Shi, L.; Majumdar, A.; McEuen, P.L. Phys. Rev. Lett. 2001, 87, 215502.

83. Nihei, M.; Horibe, M.; Kawabata, A.; Awano, Y. Jpn. J. Appl. Phys. 2004, 43, 1856.

84. Iwai, T.; Shioya, H.; Kondo, D.; Hirose, S.; Kawabata, A.; Sato, S.; Nihei, M.; Kikkawa, T.; Joshin, K.; Awano, Y.; Yokoyama, N. IEDM Tech. Dig., 2005, 11-3.

85. Balandin, A.A.; Ghosh, S.; Bao, W.; Calizo, I.; Teweldebrhan, D.; Miao, F.; C. N. Lau, C.N. Nano Lett. 2008, 8, 902.

86. Jung, D.H.; Lee, C.H.; Kim, C.S.; Shin, D.R. J. Power Sources, 1998, 71, 169.

87. Shim, J.H.; Song, S.M.; Her, W.K.; Koo, I.G.; Lee, W.M. J. Electrochem. Soc. 2003, 150, A1583.

88. Shim, J.H.; Koo, I.G.; Lee, W.M.; Electrochem. Solid-State Lett. 2005, 8, H1.

89. Arico, S.; Baglio, V.; Modica, E.; Blasi, A.D.; Antonucci, V. Electrochem. Commun. 2004, 6, 164.

90. Arico, S.; Srinivasan, S.; Antonucci, V. Fuel Cells, 2001, 1, 133.

91. Girishkumar, G.; Vinodgopal, K.; Kamat, P.V.; J. Phys. Chem. B, 2004, 108, 19960.

92. Gloaguen, F.; Leger, J.M.; Lamy, C. J. Appl. Electrochem. 1997, 27, 1052.

93. Liu, Z.L.; Lin, X.H.; Lee, J.Y.; Zhang, W.; Han, M.; Gan, L.M.; Langmuir, 2002, 18, 4054.

94. Rajesh, B.; Thampi, K.R.; Bonard, J.M.; Mathieu, H.J.; Xanthopoulos, N.; Viswanathan, B. Chem. Commun. 2003, 2022-2023.

95. Vinodgopal, K.; Haria, M.; Meisel, D. Kamat, P. Nano Lett. 2004, 4, 415.

96. Peigney, A.; Laurent, C.; Flahaut, E.; Bacsa, R. R.; Rousset, A. Carbon 2001, 39, 507–514.

97. Chae, H. K.; Siberio-Perez, D. Y.; Kim, J.; Go, Y.; Eddaoudi, M.; Matzger, A. J.; O'Keeffe, M.; Yaghi, O. M. Nature 2004, 427, 523–527.

98. Park, I. S.; Lee, K. S.; Jung, D. S.; Park, H. Y.; Sung, Y. E. Electrochim. Acta 2007, 52, 5599–5605.

99. Wang, C. H.; Du, H. Y.; Tsai, Y. T.; Chen, C. P.; Huang, C. J.; Chen, L. C.; Chen, K. H.; Shih, H. C. J. Power Sources 2007, 171, 55–62.

100. Sun, C. L.; Chen, L. C.; Su, M. C.; Hong, L. S.; Chyan, O.; Hsu, C. Y.; Chen, K. H.; Chang, T. F.; Chang, L. Chem. Mater. 2005, 17, 3749–
3753.

101. Ge, X. B.; Wang, R. Y.; Liu, P. P.; Ding, Y. Chem. Mater. 2007, 19, 5827–5829.

102. Yoo, E.; Okata, T.; Akita, T.; Kohyama, M.; Nakamura, J.; Honma, I. Nano Lett. 2009, 9, 2255–2259.

103. Xu, C.; Wang, X.; Zhu, J. W. J. Phys. Chem. C 2008, 112, 19841–19845.

CHAPTER 2

The Production of Oxygenated Polycrystalline Graphene by One Step Ethanol-Chemical Vapor Deposition

Large-area mono- and bilayer graphene films were synthesized on Cu foil (~ 1 inch^2) in about 1 min by a simple ethanol-chemical vapor deposition (CVD) technique. Raman spectroscopy and high resolution transmission electron microscopy revealed the synthesized graphene films to have polycrystalline structures with 2-5 nm individual crystallite size which is a function of temperature up to 1000°C. X-ray photoelectron spectroscopy investigations showed about 3 atomic% carboxylic (COOH) functional groups were formed during growth. The field-effect transistor devices fabricated using polycrystalline graphene as conducting channel (Lc=10 ìm; Wc=50 ìm) demonstrated a p-type semiconducting behavior with high drive current and Dirac point at ~35 V. This simple one-step method of growing large area polycrystalline graphene films with semiconductor properties and easily functionalizable groups should assist in the realization of potential of polycrystalline graphene for nanoelectronics, sensors and energy storage devices.

2.1. Introduction

Graphene, a one atom thick sp^2-hybridized two-dimensional (2D) honeycomb lattice of a carbon allotrope, because of its unique band structure, band-tuning ability, extremely high carrier mobility, themal transport properties and high chemical stability [1-3], is being envisioned as a promising material for replacing silicon in future electronics towards applications in actuators, solar cells, field-emission devices, field-effect transistors, supercapacitors, and batteries [4-9]. To realize this goal will require large area synthesis of high quality graphene layers that is not presently possible with the current exfoliation method.

Among the several approaches reported to-date, chemical vapor deposition (CVD) of carbon atoms on metal substrates has created great interest because of the low-cost production of graphene layers [10, 11]. Most importantly, highly crystalline large area monolayer graphene film can be grown directly on a copper (Cu) surface by a surface-catalysis process up to 1000°C using a gaseous or solid carbon source such as methane (CH_4), acetylene (C_2H_2) and polymethaylmethacrylate (PMMA) without the limitation of the underlying features of the copper substrate [6, 10, 12, 13]. Perfectly crystalline graphene, a zero bandgap material, while ideal for several electronic applications, lacks the semiconductor properties required for application as a transistor channel. Development of bandgap energy in graphene has ranged from lateral charge confinement in lithographically patterned graphene nanoribbons to covalent attachment of aryl groups to the basal carbon and doping with nitrogen [14-16].

A recent report on electronic transport modeling in polycrystalline graphene showed that an introduction of a short-range charge disorder, that is about 0.1 nm^{-1}, can help achieve a higher on/off current ratio of about 10^3 larger than that of top gated single crystalline monolayer graphene field-effect transistor (about 5) [17, 18]. In fact, an introduction of a controlled amount of crystal defects could be a band-tuning tool for semi-metallic graphene film without engaging bulk bandgaps to achieve desired electronic properties. However, in a typical graphene synthesis method, incorporation of randomly oriented defects in the form of polycrystallinity should be the common features in the graphene film instead of having a certain periodicity of defects. Thus, a disorder induced polycrystalline graphene film may be worth studying in its practical application in nano- and opto-electronics.

In this report, we have evaluated the use of ethanol vapor as a carbon source for the synthesis of large area (>1 sq. in.) graphene by CVD on copper foil. Detailed investigation of the mono- and bi-layer graphene synthesized by ethanol precursor for 1 min by Raman spectroscopy, high resolution transmission electron microscopy (HRTEM), X-ray photoelectron spectroscopy (XPS) revealed the material to be polycrystalline with a large number of edge defects and disorder and C=O and COOH groups. The size of graphene nanocrystal in the polycrystalline graphene, the amount of oxygen-related groups and the amount of sp^2- and sp^3-hybridized carbon were a function of the synthesis temperature. Field-effect transistor investigations demonstrated the film to be a p-type semiconductor with high drive current capacity. Randomly oriented defects

towards the grain boundaries of polycrystalline graphene could be beneficial to incorporate specific doping elements and/or different functional groups in the defect sites to achieve desired electronic properties.

2.2 Experimental Procedure

2.2.1 Growth and Transfer of Polycrystalline Graphene

Graphene films were grown by CVD process on copper foil (25 μm thick and 2.5 cm x 2.5 cm) as growth substrate. The process started with cleaning of the foil with acetone followed by drying with blowing Ar gas. The foil was then placed inside a fused silica tube (5 cm inside diameter by 100 cm long) and the temperature raised to 1000°C under flowing Ar/H_2, 200 sccm (standard cubic centimeter per min)/100 sccm, followed by annealing for 30 min. The flow rates were controlled precisely by mass flow controllers. Graphene was synthesized at the specified growth temperature under an atmosphere of ethanol vapors in Ar as carrier gas (200 sccm) by the bubbling of anhydrous ethanol and H_2 at 100 sccm for 1 min. After the reaction the bubbling was stopped and the substrate cooled naturally down to room temperature under Ar/H_2 flow. Bilayer graphene films were removed from the Cu foil by etching in a 1 M aqueous $FeCl_3$ solution, followed by subsequent cleaning with an aqueous HCl (5%) and D.I. water. The cleaning steps were performed by gently removing the solution several times using a pipette to keep the graphene flims intact on the D.I. water surface. For monolayer, graphene on one side of Cu foil was removed with O_2 plasma before the etching of the

foil. Graphene film was transferred/collected onto quartz or SiO_2/Si substrate by contacting the substrate with the film floating on water. In the case of CH_4-CVD of graphene film, the growth was performed at 900°C for 5 min in flowing $Ar/H_2/CH_4$ (200/100/10 sccm) atmosphere.

2.2.2 Materials Characterization

Detailed characterization of synthesized large-area graphene layer was performed using optical microscopy, Raman spectroscopy (Nicolet Almega XR Raman microscope; λ_{EX}= 532 nm), X-ray photoelectron spectroscopy (XPS; PHI Model 5400AXIS Ultra Kratos XPS) and transmission electron microscopy (TEM; Philips, CM300, Japan) with a LaB6 cathode operated at 300kV.

For electrical characterization, the as-grown graphene film was transferred on p+ Si/SiO_2 substrate. The heavily doped Si substrate served as a global back-gate, while the thermally grown SiO_2 (300 nm) was used as gate insulator. Source and drain electrodes were fabricated to a graphene film (channel length, Lc: 10 μm and width, Wc: 50 μm) using photolithography to define the contact areas, followed by electron-beam evaporation of Cr (20 nm)/Au (180 nm) using an E-beam evaporator (Temescal, BJD-1800). I–V characteristics of individual graphene FET were obtained at room temperature using a semiconductor parameter analyzer (Hewlett Packard-4155A, Austin, TX, USA).

2.3 Results and Discussion

Fig. 1a shows optical micrographs of mono and bilayer polycrystalline graphene films grown at 900°C for 1 min in flowing H_2 (80 sccm) and ethanol vapor saturated Ar (200 sccm) atmospheres, floating on deionized (D.I.) water after etching of Cu foil in 1 M aqueous $FeCl_3$ solution. Since graphene was formed on both sides of the Cu foil (~25 μm thick), two films are attached together on the removal of interfacial Cu foil during the etching process to give a bilayer. For monolayer graphene, one side of the Cu foil was exposed to O_2 plasma to extract the film formed on the other side. Both monolayer and bilayer films had high transparencies as evident by 97% and 91% transmittance, respectively, in the 500 to 1000 nm wavelength regime (Fig. 1b).

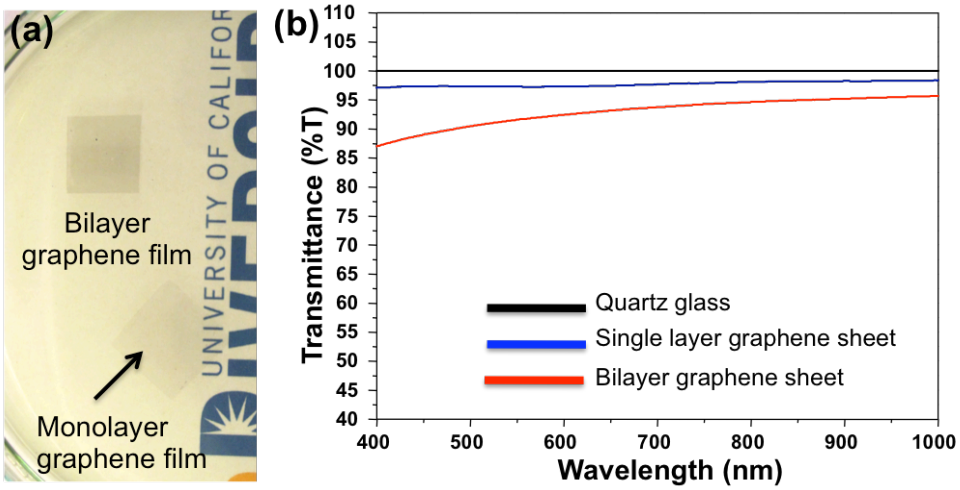

Figure 2.1. a) Optical micrograph showing single layer and bilayer graphene film synthesized at 900°C for 1 min using ethanol-CVD, floating on D.I. water. b) Optical transmittance of single and bilayer graphene films on a quartz substrate showing a transmittance value of about 97% and 91%, respectively, in the 500-1000 nm wavelength regime.

The Raman spectrum of single layer graphene films synthesized using ethanol vapor and CH_4 precursors at 900°C are presented in Fig. 2a. As expected, the Raman spectrumof graphene film grown using CH_4 precursor had (a) G-band (1560 cm^{-1} to1620 cm^{-1}) comprised of E2g vibrational mode of sp^2-bonded carbon in a two dimensional hexagonal lattice, (b) a negligible disorder mode D-band (1300 cm^{-1} to 1400 cm^{-1}) due to the breathing vibrations of sp^2 carbon rings with dangling bonds in plane terminations of the disordered graphite which becomes Raman active after neighboring sp^2 carbons are converted to sp^3 hybridization in graphitic structure [19, 20], (c) 2D-band (2660 cm^{-1} to

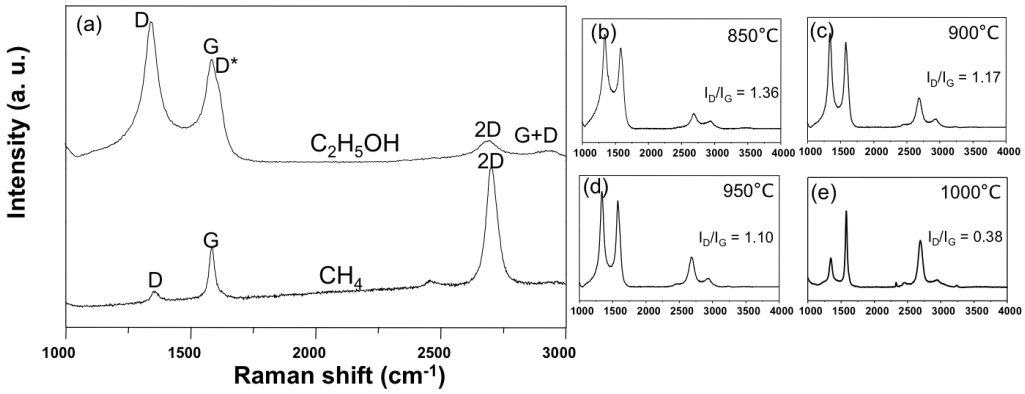

Figure 2.2 a) A comparison of collected Raman spectra of CVD grown graphene film synthesized at 900°C using CH_4 and C_2H_5OH precursors. b-e) Raman spectra of CVD grown graphene film grown for 1 min using ethanol vapor as a function of temperature.

2700 cm^{-1}) comprised of a second order vibration appearing from the scattering of phonons at the zone boundary and (d) 2D-band intensity approximately two times the intensity of G-band. These results are consistent with the characteristics for highly

crystalline graphene layers [10, 11].On the other hand, in the case of graphene film grown using ethanol vapor the intensity of D-band at 1345 cm^{-1} became the most prominent feature in the Raman spectrum and the characteristic 2D-band intensity at 2675 cm^{-1} was significantly reduced, characteristics of highly disordered sp^3 hybridization of carbon lattice was not observed in graphene film synthesized using CH_4. Further, these films had a large number of edge defects and disorder as evidenced by the well-defined presence of D* band at 1620 cm^{-1} and strong (G + D) band at about 2940 cm^{-1}, respectively [21].

Having confirmed that the graphene film using ethanol vapor had unique polycrystalline features not present in methane grown film, we investigated the effect of synthesis temperature, while keeping the other process parameters constant, on crystallinity using Raman microscopy (Fig. 2b-e). As shown in these spectra, the FWHM (full width at half maximum) of the G-band decreased and was an inverse function of the growth temperature, which is direct evidence of enhanced sp^2-hybridization of carbon lattice and the annealing of structural defects [22]. On the other hand, the I_D/I_G ratio decreased gradually from a value of 1.36 at 850°C (Fig. 2b) to about 0.38 at 1000°C (Fig. 2e), revealing the restoration of damaged lattice, i.e., induction of the crystalline order at higher growth temperature. However, the presence of disorder-induced D and (G+D) features in the graphene film synthesized by ethanol-CVD was not totally diminished even up to 1000 °C. Thus, the higher growth temperature may increase the crystallite size in polycrystalline graphene film only by the maximal restoration of existing defects up to

1000 °C, which were further analyzed using TEM studies (Figs. 3 and 4). This observation confirms the existence of short-range order in graphene films even at higher growth temperatures as well as the inability of these films to achieve long range order of AB stacking sequences.

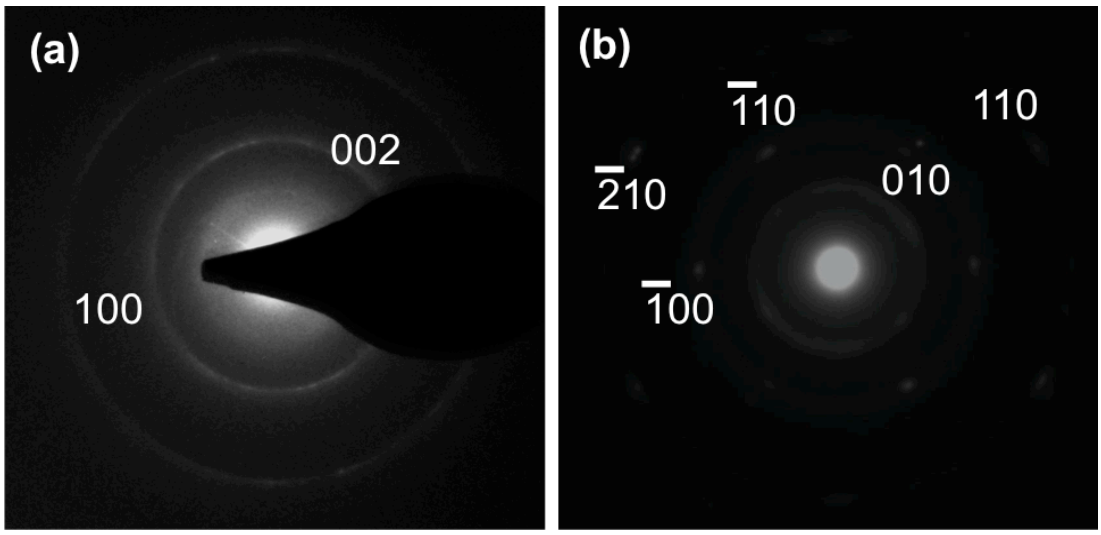

Figure 2.3 Electron diffraction pattern of CVD grown graphene film synthesized at 900°C using a) C_2H_5OH (for 1 min) and b) CH_4 (for 5 min) precursors.

Fig. 3 shows a comparison of the electron diffraction patterns taken from the graphene films synthesized at 900°C using ethanol vapor and CH_4 gas. The ethanol-derived graphene film (Fig. 3a) consisted of concentric rings corresponding to (002) and (100) planes of graphitic structures, which are expected due to the highly polycrystalline nature of the graphene layer. The Bragg spacings d_{002} and d_{100} were found to be 0.347 nm and 0.210 nm as compared to 0.348 nm and 0.212 nm, respectively, for single crystal

graphitic structure (JCPDS data). On the other hand, the CH_4-derived graphene film (Fig. 3b) had the typical six-fold symmetrical spots attributed to the long range crystalline ordering of mono- or bi-layer single crystal graphene film.

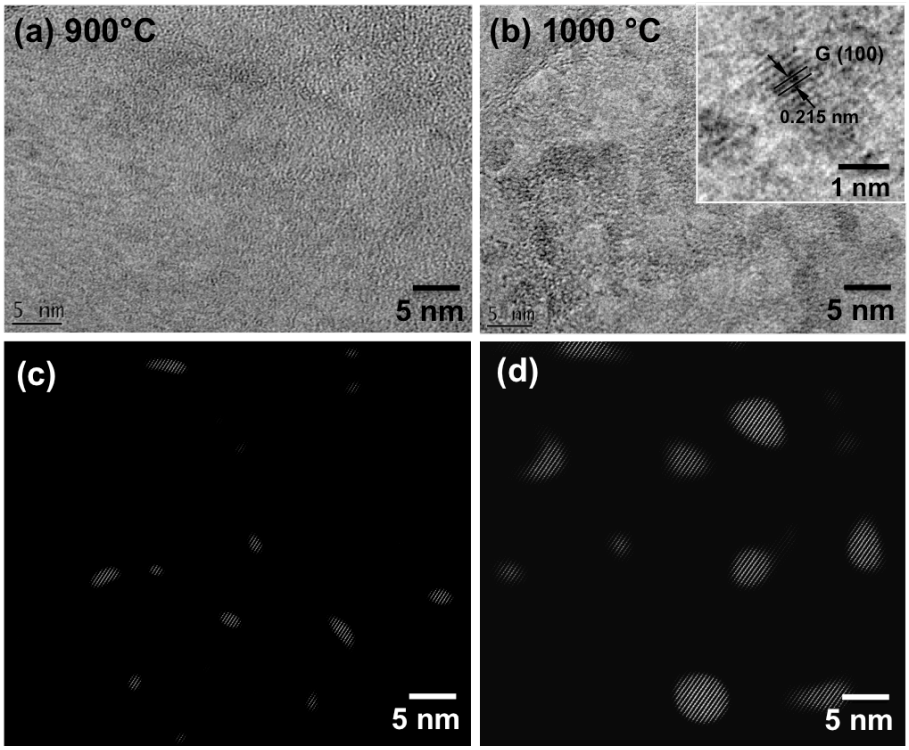

Figure 2.4. a, b) HRTEM and corresponding c, d) inverted FFT images of polycrystalline graphene film synthesized at 900°C and 1000°C using ethanol vapor.

To further characterize the polycrystallinity in ethanol-derived graphene film, HRTEM analysis was carried out. Fig. 4 shows HRTEM and corresponding inverted FFT images of graphene films synthesized at 900°C and 1000°C for 1 min using ethanol vapor. The size of individual crystals in polycrystalline graphene synthesized at 900°C and 1000°C were about ~2 nm (Fig. 4c) and ~5 nm (Fig. 4d), respectively. The inset

HRTEM image in Fig. 4b clearly shows the two dimensional lattice fringes of individual graphene crystals. The interplanar d-spacing measured from the fringe pattern, as indicated in Fig. 4b, was about 0.215 nm corresponding to the {100} planes of the graphitic crystal system. These results revealed that the size of graphene nanocrystals in the polycrystalline graphene film increased at 1000°C due to the restoration of defect sites at high temperature.

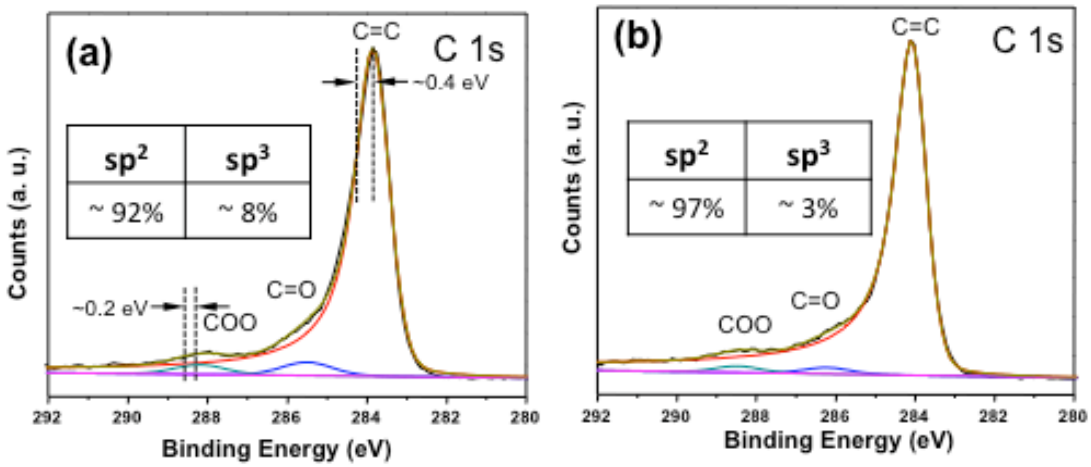

Figure 2.5 XPS spectra of ethanol CVD grown graphene film synthesized at a) 900°C and b) 1000°C for 1min using ethanol vapor.

Fig. 5 shows the X-ray photoelectron spectroscopy (XPS) of graphene films grown by ethanol-CVD at 900ºC and 1000ºC. We first examined the XPS spectra for graphene synthesized at 900ºC. As shown in Fig. 5a, the C 1s XPS spectra exhibited three Gaussian peaks centered at 284.2 eV, 285.5 eV and 288.3 eV, attributed to sp^2-hybridized carbon atoms (C=C), keto (C=O) and carboxylic (COOH) or epoxy groups, respectively

[21, 23]. The presence of C=O and COOH are strong indicators of considerable degree of oxidation. The amount of sp^2- and sp^3-hybridized carbon were estimated to be 92% and 8%, respectively. The ratio of sp^3/sp^2 carbon atoms could also explain the large intensity of the D-band observed in Raman spectroscopy in Fig. 2. It is likely that oxygen-related functional groups could have originated from the dissociated ethanol vapor at high temperature. The grain boundaries in polycrystalline graphene are unsaturated carbon sites where bound oxygen and hydrogen in the oxygen related functional groups could saturate the carbon dangling bonds. The amount of –COOH functional group was estimated at ~3 atomic%, which is comparable to the 0.5 to 3% in commercial CNTs. The high content of COOH functional groups in the large area polycrystalline graphene were incorporated in-situ during the CVD growth as opposed to the traditional post-synthesis nitric acid refluxing, as in the case of CNTs. This is a significant advantage since acid treatement involves modification of unsaturated carbon-carbon bonds on CNT surfaces that can have serious implications on electronic properties. The presence of COOH groups opens the way for further functionalization and covalent binding of various monomer and polymer matrices to graphene for applications in energy storage, biological systems, photovoltaics and nanoelectronics [22-24].Further studies would be required for a better understanding of methods to control the amount of functional groups in the polycrystalline graphene. Figure 5b shows the XPS spectra of polycrystalline graphene film synthesized at 1000°C. While spectra were similar in terms of the major peaks, there were however subtle important differences. Notably, there was an increase in the intensity and sharpness of the peak at 284.6 eV and decrease in the intensity of the peak

at 288.3 eV. The former is attributed to increased sp^2-hybridization of carbon lattice at higher temperatures whereas the latter is a result of the removal of oxygen-related functional groups during cooling of the film from 1000ºC to room temprature under Ar/H_2 environment. The amount of sp^2- and sp^3-hybridized carbon atoms were estimated at about 97% and 3%, respectively, compared to 92% and 8%, respectively, in film grown at 900ºC (Fig. 5a). Moreover, there was a typical redshift (~0.4 eV) towards lower binding energy and broadening of C 1s peaks caused by the incorporation of oxide functional groups which is similar to the case for p-doped carbon nanotubes in graphene film synthesized at 900°C compared to one synthesized at 1000°C [25, 26].

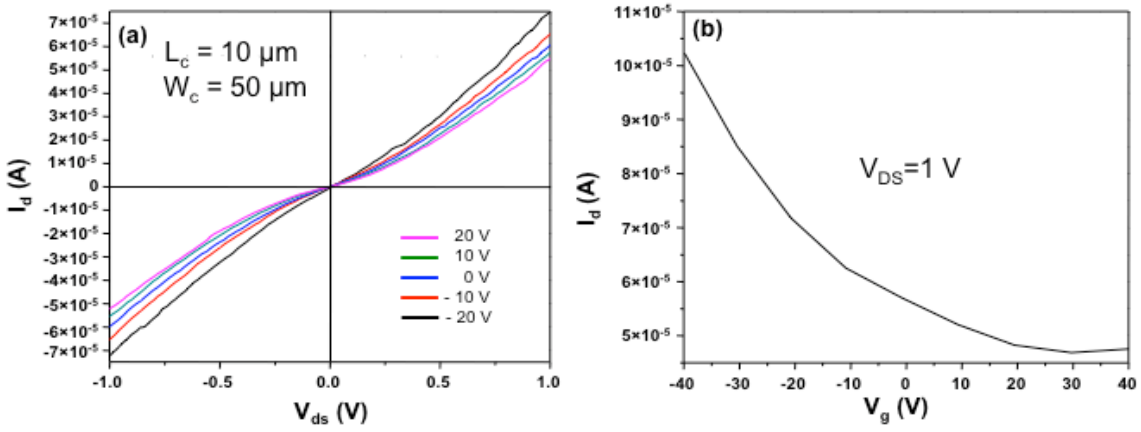

Figure 2.6 Electrical properties of polycrystalline graphene film synthesized at 900°C using ethanol vapor. a) Low bias two terminal source–drain current–voltage (I_d–V_{ds}) and b) transfer (I_d-V_g) characteristic curves recorded on a graphene FET (L_c=10 µm and W_c=50 µm).

To evaluate the impact/contribution of oxide functional group incorporation on the electronic properties of polycrystalline graphene film, we performed field-effect transistor studies (Fig. 6), on polycrystalline graphene having channel length (L_c) and width (W_c) of about 10 μm and 50 μm, respectively. Source-drain current (I_{ds}) vs. the source-drain voltage (V_{ds}) characteristic curves at different gate voltages (V_g) for the polycrystalline graphene (Fig. 6a) exhibited typical p-channel transistor behavior as well as clear gate modulation of conductance compared with that of CH_4-CVD grown graphene film, which could be attributed to the polycrystalline nature of ethanol-CVD grown graphene film[11]. Additionally, the total drive current of the polycrystalline graphene FET showed comparatively much higher value than the sub-micron width bulk graphene FET showing similar gate modulation with the gate biases [10, 11, 15]. Similarly, the transfer curve of the device with back gate voltage varied from –40 to 40 V at V_{ds} of 1V showed a slow increase of I_{ds} with decreasing V_g (Fig. 6b), confirming a p-type behavior of the polycrystalline graphene FET having a Dirac point at about 35V. The p-type behavior as well as shifting of the Dirac point can also be attributed to the adsorbed oxygen and the oxygen-related functional groups (such as C=O and COOH) and is in accordance with the observations of p-type doping when the edge defects in carbon nanotube (CNT), CVD graphene and graphene nanoribbon are terminated by hydrogen and oxygen and hydroxyl and carboxylic groups [27-29]. The decrease in L_c and W_c of polycrystalline graphene channel by patterning polycrystalline graphene into nanoribbons 30-32] or nanomesh [33] can potentially improve gate modulation further.

2.4 Conclusion

Using an ethanol-chemical vapor deposition technique, polycrystalline graphene film was synthesized utilizing surface catalysis mechanism on a copper surface. By using Raman spectroscopy, X-ray photoelectron spectroscopy, electron diffraction pattern analysis and high-resolution transmission electron microscopy techniques, we demonstrated the polycrystalline nature of synthesized graphene film showing p-type semiconducting behavior as well as incorporation of oxygen-related carboxylic functional group (~ 3 at.%). The sizes of individual graphene crystallite in the graphene films synthesized at 900°C and 1000°C were about 2 nm and 5 nm, respectively, and they are oriented in [100] the crystal direction. The synthesized polycrystalline graphene film could potentially be exploited in the doping of heteroatoms as well as binding with other functional groups for desired applications. The reported method provides large-area polycrystalline graphene film, which could be a potential candidate to study further for applications in sensors, energy storage, biological systems and nanoelectronics.

Acknowledgements

We acknowledge the financial support from the Dean of Bourns College of Engineering at the University of California, Riverside and the National Institutes of Health grant U01ES016026. Part of the characterization work was carried out in the Frederick Seitz Materials Research Laboratory Central Facilities, University of Illinois,

which are partially supported by the U.S. Department of Energy under grants DE-FG02-07ER46453 and DE-FG02-07ER46471.

2.5 References

1. Novoselov KS, Geim AK, Morozov SV, Jiang D, Zhang Y, Dubonos SV, et al. Electric field effect in atomically thin carbon films. Science 2004; 306, 666-669.

2. Zhang Y, Tan JW, Stormer HL, Kim P.Experimental observation of the quantum Hall effect and Berry's phase in graphene. Nature 2005; 438, 201-204.

3. Novoselov KS, Geim AK, Morozov SV, Jiang D, Katsnelson MI, Grigorieva IV, et al. Two-dimensional gas of massless Dirac fermions in graphene. Nature 2005; 438, 197-200.

4. Lin J, Penchev M, Wang G, Paul RK, Zhong J, Jing X, et al. Heterogeneous graphene nanostructures: ZnO nanostructures grown on large-area graphene layers. Small 2010; 6, 2448-2452.

5. Wang X, Zhi L, Mullen K. Transparent, conductive graphene electrodes for dye-sensitized solar cell. Nano Lett 2008; 8, 323-327.

6. Paul RK, Ghazinejad M, Penchev M, Lin J, Ozkan M, Ozkan CS. Synthesis of a pillared graphene nanostructure: a counterpart of three-dimensional carbon architectures. Small 2010; 6, 2309-2313.

7. Yoo E, Kim J, Hosono E, Zhou H, Kudo T, Honma I. Large reversible Li storage of graphene nanosheet families for use in rechargeable lithium ion batteries. Nano Lett 2008; 8, 2277-2282.

8. Blake P, Brimicombe PD, Nair RR, Booth TJ, Jiang D, Schedin F, et al. Graphene-based liquid crystal device. Nano Lett 2008; 8, 1704-1708.

9. Nair RR, Blake P, Grigorenko AN, Novoselov KS, Booth TJ, Stauber T, et al. Fine structure constant defines visual transparency of graphene. Science 2008; 320, 1308.

10. Li X, Cai W, An J, Kim S, Nah J, Yang D, et al. Large-area synthesis of high-quality and uniform graphene films on copper foils. Science 2009; 324, 1312-1314.

11. Kim KS, Zhao Y, Jang H, Lee SY, Kim JM, Kim KS, et al. Large-scale pattern growth of graphene films for stretchable transparent electrodes. Nature 2009; 457, 706-710.

12. Sun Z, Yan Z, Yao J, Beitler E, Zhu Y, Tour JM. Growth of graphene from solid carbon sources. Nature 468; 2010, 549-552.

13. Rasool HI, Song EB, Allen MJ, Wassei JK, Kaner RB, Wang KL, et al. Continuity of graphene on polycrystalline copper. Nano Lett 2011;11, 251-256.

14. Niyogi S, Bekyarova E, Itkis ME, Zhang H, Shepperd K, Hicks J, et al. Spectroscopy of covalently functionalized graphene. Nano Lett 2010; 10, 4061-4066.

15. Wei D, Liu Y, Wang Y, Zhang H, Huang L, Yu G. Synthesis of n-doped graphene by chemical vapor deposition and its electrical properties. Nano Lett 2009; 9, 1752-1758.

16. Bekyarova E, Itkis ME, Ramesh P, Berger C, Sprinkle M, deHeer WA et al. Chemical modification of epitaxial graphene: spontaneous grafting of aryl groups. J Am Chem Soc 2009; 131, 1336-1337.

17. Kim P. Graphene: across the border. Nat Mater 2010; 9, 792-793.

18. Yazyev OV, Louie SG. Electronic transport in polycrystalline graphene. Nat Mater 2010; 9, 806-809.

19. Ferrari AC, Meyer JC, Scardaci V, Casiraghi C, Lazzeri M, Mauri F,et al. Raman spectrum of graphene and graphene layers. Phys Rev Lett 2006; 97, 187401-187404.

20. Malard LM, Pimenta MA, Dresselhaus G, Dresselhaus MS. Raman spectroscopy in graphene. Phys Rep 2009; 473, 51-87.

21. Campos-Delgado J, Romo-Herrera JM, Jia X, Cullen DA, Muramatsu H, Kim YA, et al. Bulk production of a new form of sp^2carbon: crystalline graphene nanoribbons. Nano Lett 2008; 8, 2773-2778.

22. Dresselhaus M, Jorio SA, Saito R. Characterizing graphene, graphite, and carbon nanotubes by Raman spectroscopy. Annu Rev Condens Matter Phys 2010; 1, 89-108.

23. Campos-Delgado J, Farhat H, Kim YA, Reina A, Kong J, Endo M, et al. Resonant Raman study on bulk and isolated graphitic nanoribbons. Small 2009; 5, 2698-2702.

24. Janowska I, Chizari K, Ersen O, Zafeiratos S, Soubane D, Costa VD, et al. Microwave synthesis of large few-layer graphene sheets in aqueous solution of ammonia. Nano Res 2010; 3, 126-137.

25. Bae S, Kim H, Lee Y, Xu X, Park JS, Zheng Y, et al. Roll-to-roll production of 30-inch graphene films for transparent electrodes. Nat Nanotechnol 2010; 5, 574-578.

26. Geng HZ, Kim KK, So KP, Lee YS, Chang Y, Lee YH. Effect of acid treatment on carbon nanotube-based flexible transparent conducting films. J Am Chem Soc 2007; 129, 7758-7759.

27. Woo HS, Czerw R, Webster S, Carroll DL, Ballato J, Strevens AE, et al. Hole blocking in carbon nanotube–polymer composite organic light-emitting diodes based on

poly (m-phenylene vinylene-co-2, 5-dioctoxy-p-phenylene vinylene). Appl Phys Lett 2000; 77, 1393-1395.

28. Gunlycke D, Li J, Mintmire JW, White CT. Altering low-bias transport in zigzag-edge graphene nanostrips with edge chemistry. Appl Phys Lett 2007; 91, 112108-112110.

29. Wang X, Li X, Zhang L, Yoon Y, Weber PK, Wang H, et al. N-doping of graphene through electrothermal reactions with ammonia. Science 2009; 324, 768-771.

30. Han, MY, Ozyilmaz B, Zhang Y, Kim, P. Energy band-gap engineering of graphene nanoribbons. Phys Rev Lett 2007; 98, 206805-2068808.

31. Li X, Wang X, Zhang L, Lee S, Dai H. Chemically derived, ultrasmooth graphene nanoribbon semiconductors. Science 2008; 319, 1229-1232.

32. Kobayashi T, Kimura N, Chi J, Hirata S, Hobara D. Channel-length-dependent field-effect mobility and carrier concentration of reduced graphene oxide thin-film transistors. Small 2010; 6, 1210-1215.

33. Bai J, Zhong X, Jiang S, Huang Y, Duan X. Graphene nanomesh. Nat Nanotechnol 2010; 5, 190-194.

CHAPTER 3

Patterning of Large Area Graphene Using Nanosphere Lithography: Toward High I_{ON}/I_{OFF} Ratio Graphene Nanomesh Field-Effect Transistor

The zero bandgap of semimetal graphene still limits its application as an effective field-effect transistor device operating at room temperature.[1] Thus, continuous efforts have been made to open up a bandgap in this material. It has been shown theoretically and experimentally that graphene nanoribbons (GNRs)[2] or nanomeshes (GNMs)[3] can attain a bandgap that is large enough for a transistor device, and show considerable transconductance or I_{ON}/I_{OFF} ratio while being used as channel materials. In this work, a simple reactive ion etching (RIE) combined with well-established nanosphere lithography was performed to fabricate large area GNMs from ethanol-chemical vapor deposition (CVD) grown monolayer graphene film. The detailed process conditions were optimized and characterized to form GNMs with specific dimensions and periodicity. The fabricated GNM transistor device exhibited promising electronic properties featuring high drive current and I_{ON}/I_{OFF} ratio of about 6, significantly higher than it's film counterpart. This method could also open up a way to fabricate nanomesh of various thin-film semiconductors for nanoelectronics.

3.1 Introduction

Since the discovery of graphene in 2004,[1] significant efforts have been made to open a bandgap in this zero-bandgap two-dimensional (2D) carbon nanostructure for room temperature transistor operation. In fact, it has been shown experimentally that processing of graphene into a feature size of less than 10 nm in the form of graphene nanoribbons (GNRs) could potentially open up large enough bandgap to be used as transistor channel materials.[2] Currently, chemical and sonochemical approaches, unzipping carbon nanotubes (CNTs), plasma etching of CNTs and masking graphene with silicon nanowires (SiNWs) have been employed to fabricate GNR transistor devices.[2,4-7] However, single GNR transistor devices usually have low driving current or transconductance. Therefore, mass production of GNRs as well as their successful alignment is required to develop dense arrays of circuitry for practical devices. Even though wafer scale graphene have been produced recently using chemical vapor deposition (CVD) techniques, but it is still challenging to pattern this graphene into GNRs using the state-of-the-art techniques such as e-beam lithography.

Recently, an alternative approach to produce graphene nanostructure called graphene nanomesh (GNM) with sub-10 nm features using block copolymer lithography patterning was reported.[3] These GNMs possessed an electronic bandgap, and fabricated GNM transistor devices showed an I_{ON}/I_{OFF} value comparable to individual GNR devices and supported driving currents about 100 times higher than the individual GNR device. Due to the unique characteristics, GNMs are being investigated further for possible applications in nanoelectronics. Large-scale GNMs have also been fabricated using self-

assembled monolayers of monodispersed SiO_2 colloidal microspheres.[8] These colloidal spheres can be synthesized in the size range of 50 nm to several micron using established chemistries, or are readily available commercially. Therefore, these two approaches have attracted significant interest to achieve GNMs with different neck width and periodicities. In this work, large-area GNM was synthesized using nanosphere lithography optimizing detailed process conditions. The process used polystyrene (PS) spheres to make a periodic nanoporous platinum (Pt) mask for etching graphene. Using this approach the neck width of nanoporous mask can be tuned over a large range to finally achieve GNM with desired neck width. This approach can also be employed in fabricating large area nanomesh of different thin film semiconductors for nanoelectronics.

3.2 Experimental Procedure

Synthesis of large area GNM film: Graphene film was grown by ethanol-CVD process as described previously,[9,10]and transferred onto SiO_2 (300 nm)/Si substrate. Scheme 3.1 represents the detailed process flow for synthesis of GNMs from CVD-grown large area graphene film. At first, PMMA is spin-coated onto graphene/SiO_2/Si substrate and baked at 110°C for 5 min, followed by O_2 plasma etching for 40 sec to make the surface hydrophilic. This substrate was used as the platform to perform nanosphere lithography. A stock solution consisting of 10 wt% PS spheres (Alfa Aesar) was ultra-sonicated in ethanol/water (1:1) solution for 30 min to disperse the PS spheres uniformly. Subsequently, a few drops of the stock solution are dispersed on the D.I. water surface and a drop of SDS (1%) solution was added to assemble those PS spheres into a

large area compact monolayer film on the water surface. The PMMA coated graphene/SiO_2/Si substrate was then brought into the contact of PS monolayer film on the water surface and transferred to cover the whole substrate, followed by drying at room temperature.

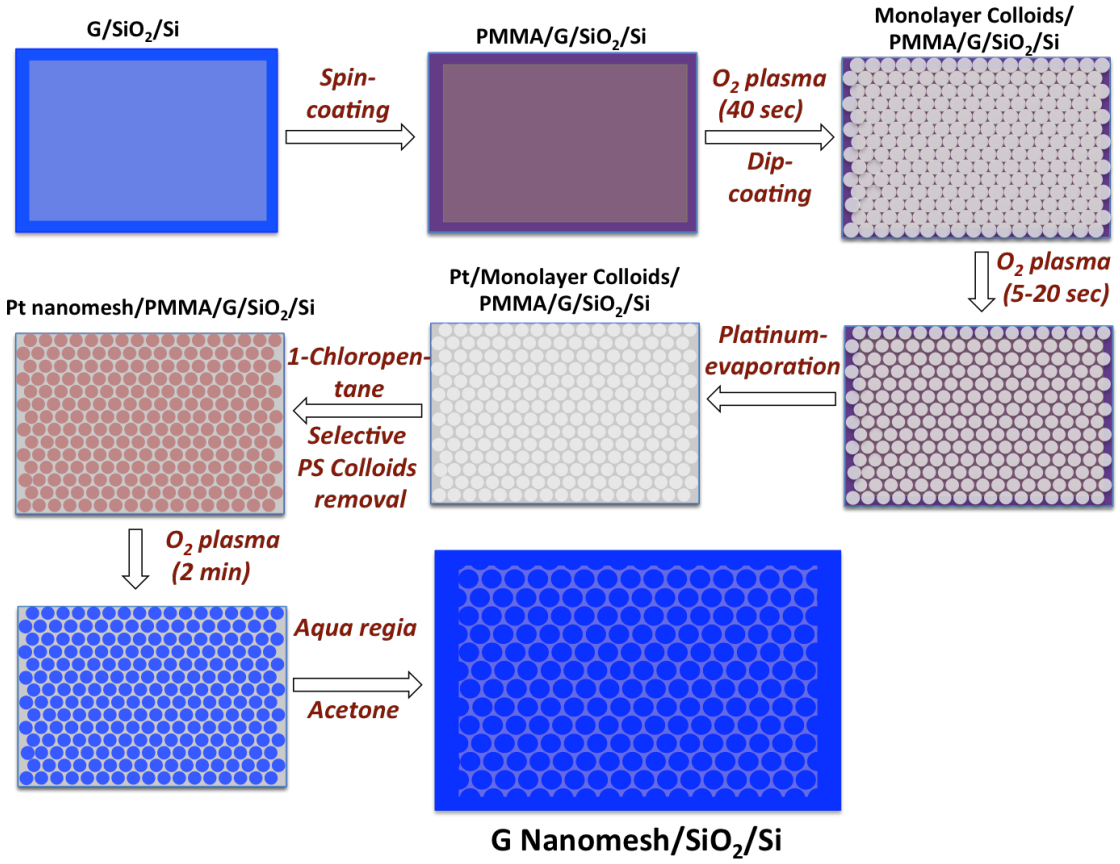

Scheme 3.1 Detailed process flow to synthesize large area GNM using PS nanosphere lithography.

Reactive ion etching (RIE; O_2) was then employed to define the desired gaps (comprised of resulting neck width of GNMs) between the spheres; the smaller the neck width, the shorter the etching time is required. Subsequently, a 15 nm Pt was deposited over the substrate using an e-beam evaporator to fill up the gaps. To perfectly remove the PS sphere afterwards, that is to form Pt nanomesh mask over the substrate, two approaches were employed: (1) ultra-sonication of PS spheres off the substrate and/or (2) dissolution of PS spheres in cyclohexane and 1-choropentane at 60°C for 2 h to optimize the process conditions. In the second RIE step, the substrate was exposed to O_2 for 150 sec to remove the graphene in the unprotected area from Pt nanomesh. A second lift-off in acetone removed the Pt nanomesh and underneath PMMA to form GNMs over SiO_2/Si substrate.

3.3 Results and Discussion

The realization of a nanoporous mask of Pt over the large area graphene film which can then be exposed to O_2 plasma to etch the graphene in the unprotected areas is the crucial step in synthesizing GNMs. The preparation of the Pt nanoporous mask consisted of four steps: 1) formation of a densely packed monolayer of PS nanospheres, 2) controlled etching of PS nanospheres to open gaps, 3) deposition of Pt and 4) removal of PS nanospheres. Figure 3.1 shows self-assembled monolayer of PS spheres transferred onto PMMA/graphene/SiO_2/Si substrate. As shown in Figure 3.1a, a monolayer of PS spheres (~200 nm) formed a close-packed hexagonal array over the entire substrate. The simple methodology of making closely packed nanospehere layer demonstrated here can be easily scaled to wafer level by using a larger water surface. PS nanospheres were then

etched using RIE. This is an important step as it will determine the neck width of the final graphene nanomesh, a larger reduction in PS nanosphere size will produce a wider neck width and vice-versa. As shown in Fig. 3.1b, RIE for 10 sec at 200W in flowing 50 sccm of flowing O_2, reduced the PS nanosphere size to form an average gap of 15-20 nm while keeping the pitch between the PS spheres unchanged. However, almost all PS nanospheres were etched away leaving debris of small PS fragments when the etching time was increased to 20 s (Fig. 3c). On the other hand, an etching time of 5 s did not produce sufficient etching to produce any gap (fig. not shown). Following the RIE, 15 nm thick Pt was deposited in the gap between PS nanospheres by metal evaporator and the sample was processed to remove the PS nanospheres.

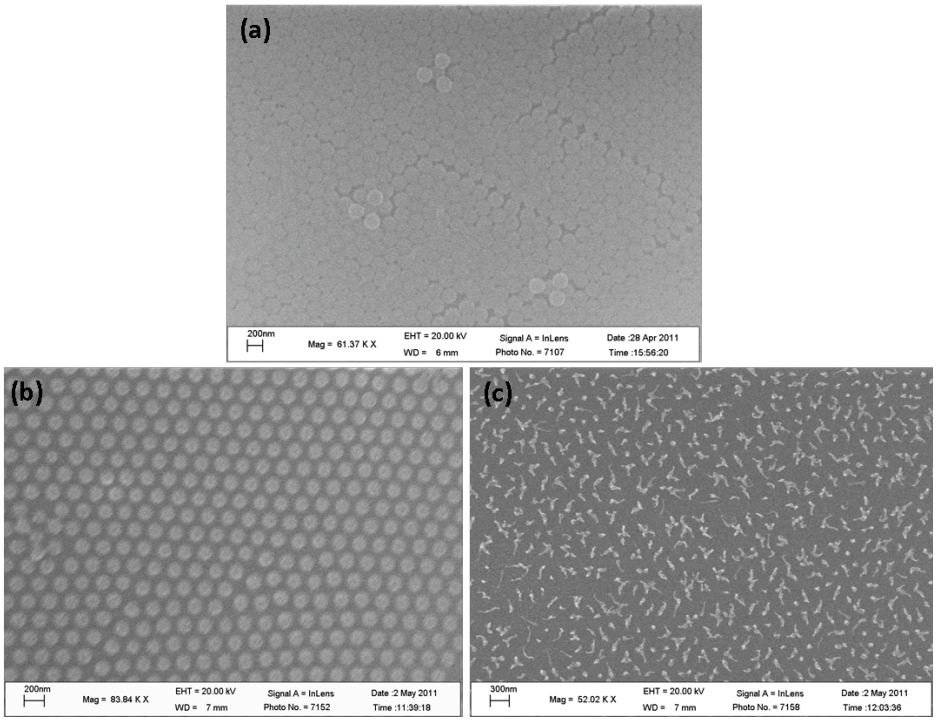

Figure 3.1 SEM images of self-assembled monolayer of PS spheres over SiO_2/Si substrates a) before and after RIE etching at 200W for b) 10 sec and (c) 20 sec.

The complete removal of PS nanospheres is another critical step in the production of a perfect Pt nanomesh over the entire substrate. The existence of any PS nanosphere in the Pt nanomesh is problematic since the unremoved PS spehere would protect graphene from etching in O_2 plasma, which will eventually form a defect in the nanoporous periodicity in the resulting GNM. Three different methods involving ultrasonication, wet-etching (lift-off) and a combination of the two were evaluated for PS nanosphere

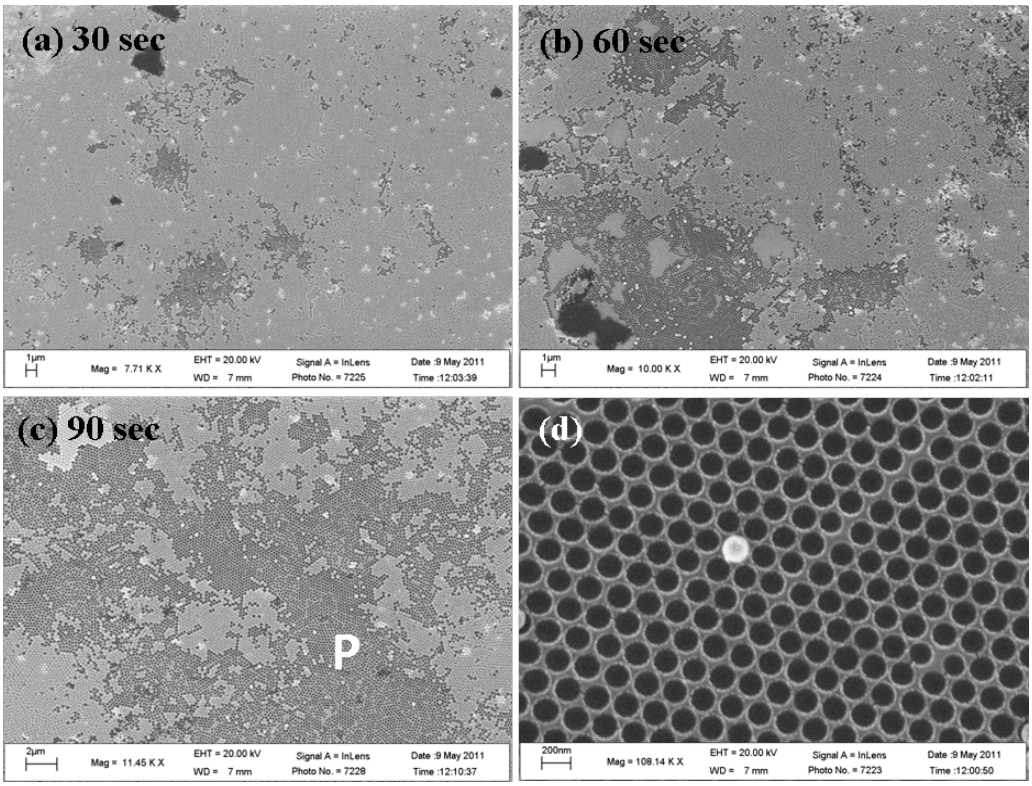

Figure 3.2 SEM images of Pt nanomesh formation after removal of PS spheres using ultrasonication for a) 30 sec, b) 60 sec, c) 90 sec in deionized water and d) magnified image of area P in image c).

removal. Ultrasonication is the most commonly use method to remove colloidal spheres.[8] Three (30, 60 and 90s) intervals of sonication for PS sphere removal were investigated and the SEM images of Pt nanomesh after removal of PS spheres are shown in Fig. 3.2. With 30 s sonication (Fig. 3.2a), the PS spheres removal was totally inefficient. Even up to 90 s sonication (Fig. 3.2c), most of PS spheres remained on the substrate. Figure 3.2d taken from region P in Fig. c, confirmed the formation of Pt nanomesh in some areas with certain periodicity, and without any damages of Pt film for 90 sec sonication. However, a longer sonication time disintegrated the Pt nanomesh (figure not shown).

Selective solvents have been used for reversible self-assembly or reconstruction/reorganization of polymer domains in block copolymers.[11,12] Cyclohexane has been recognized as one of the solvents for selective removal of PS in PMMA matrix.[13] Figure 3.3a shows SEM images of Pt deposited substrate after immersing in cyclohexane at 60°C for 2 h. Even though the treatment decreased the diameter of the PS spheres was decreased due to the surface etching, the spheres were still attached on the underneath PMMA surface. This is may be due to the residual PS remaining at the interface of PS spheres and PMMA surface, and the PS adsorbed to PMMA surface from solution of PS in cyclohexane.[14] As shown in the Fig. 3.3a inset, some PS spheres were released or tend to release at some satellite areas. However, additional removal was only possible through a 90 s ultrasonication (Fig. 3.3b).

To further investigate/optimize the conditions for the complete removal of PS spheres, 1-chloropentane was used as an alternative selective solvent and the results

were compared with cyclohexane-treated samples. SEM images in Figure 3.4 compares the Pt nanomesh formation over PMMA/graphene/SiO_2/Si substrate after removal of PS spheres in cyclohexane and 1-choropentane at 60°C for 2 h. As shown in Figure 3.4b, 1-chloropentane treatment was more efficient in removing PS speheres when compared to cyclohexane (Fig. 3.4a). In fact, PS spheres were essentially non-existent in the Pt nanomesh after 1-chloropentane treatment, as a consequences of 1-chloropentane providing a weaker driving force than cyclohexane for adsorption of PS to PMMA.[14]

The electronic properties of the resulting GNMs can be tuned by changing the size of the graphene neck-width by controlling the neck-width of the nanoporous Pt mask through control of the gap between two nanospheres. Figure 3.5 shows the effect of etching time of PS nanospheres on the resulting Pt nanomeshes. With RIE for 5 sec, the gaps were not still formed and produced hexagonal nanodot arrays of Pt after e-beam evaporation of 15 nm Pt. As the duration of RIE was increased to 10 sec, the resulting neck-width of the Pt nanomesh was about 20 nm (Fig. 3.5b). The neck-width of Pt nanomeshes was about 60 nm and 110 nm for 12 sec and 15 sec RIE, respectively, as shown in Figures 3.5c and 3.5d. These results revealed that process parameters such as RIE time, RF power and flow rate of O_2, can be varied to control the neck-width and the periodicity of the GNMs.

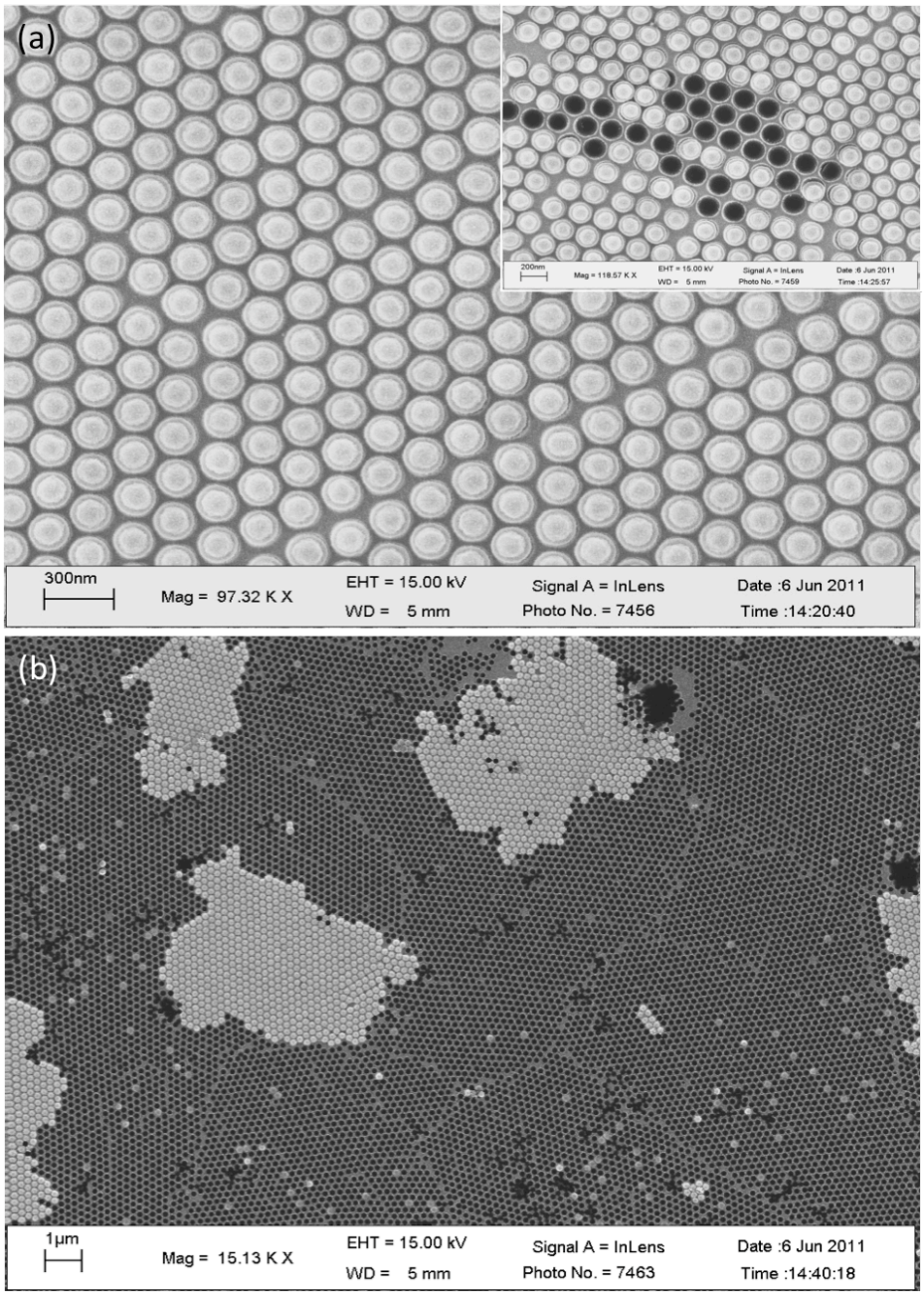

Figure 3.3 SEM images of Pt nanomesh formation after removal of PS spheres in cyclohexane at 60°C for 2 h. a) without sonication and b) additional sonication for 90 sec in D.I. water.

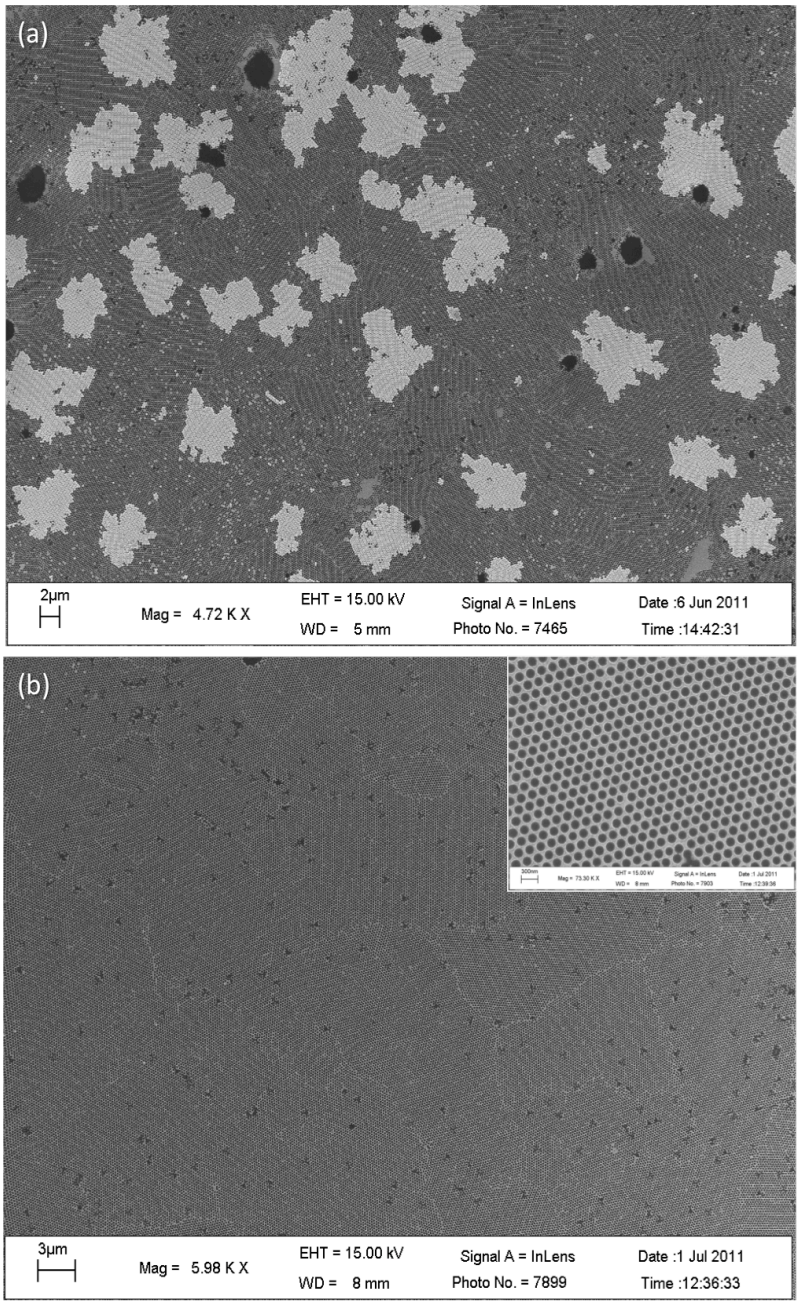

Figure 3.4 SEM images of Pt nanomesh formation after removal of PS spheres in a) cyclohexane with additional 90 sec ultrasonication and b) 1-chloropentaneat 60°C for 2 h.

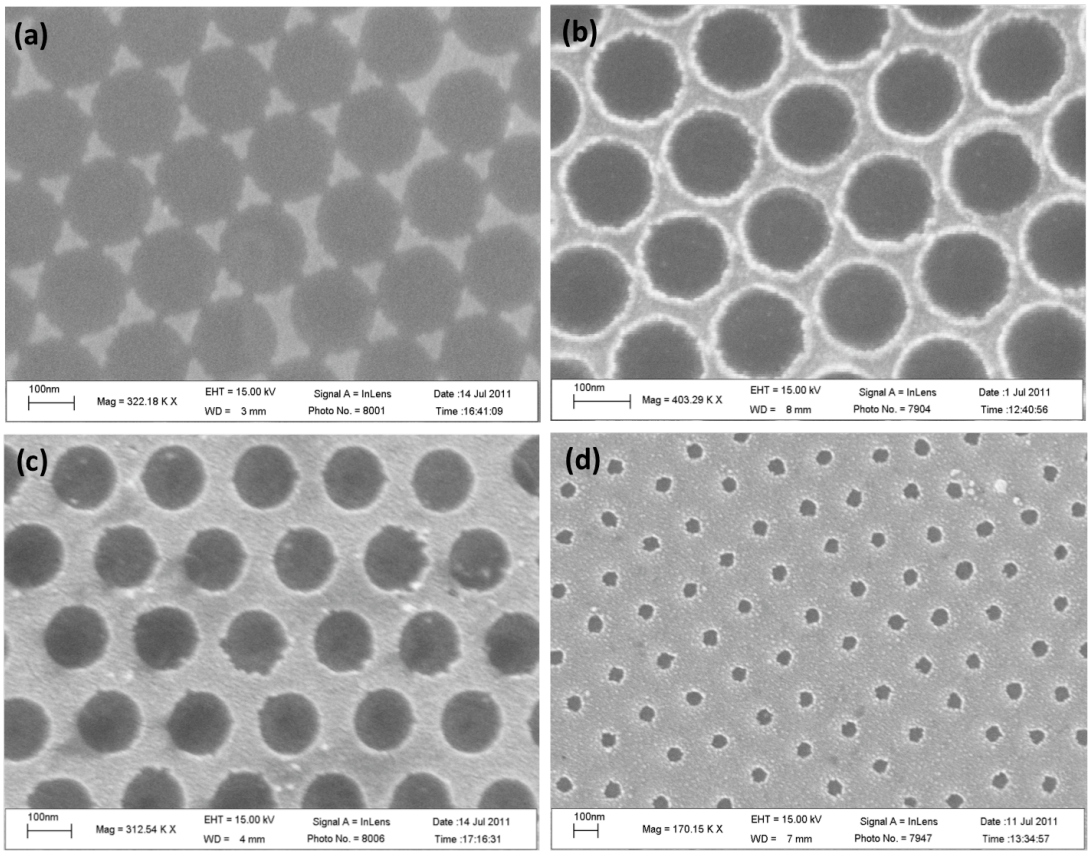

Figure 3.5 SEM images of Pt nanomeshes over PMMA/grapheme/SiO_2/Si substrates depending on RIE etching time of self-assembled PS monolayer; (a) 5 sec, b) 10 sec, (c 12 sec and d) 15 sec.

Figure 3.6 shows SEM images of large area CVD-grown graphene and corresponding GNMs after O_2 plasma etching of Pt nanomesh/PMMA/graphene/SiO_2/Si substrate at 100 W for 150 s in 50 sccm flowing O_2 atmosphere, followed by successive removal of Pt nanomesh and PMMA in aqua regina and acetone. As shown in Figure 3.6a, several wrinkles are frequently observed in the large-area graphene film during the transfer process. These wrinkles were existed/broken during the nanomesh processing

steps, and their traces are clearly visible in the large area nanomesh (Fig. 3.6b). However, our demonstrated processing steps on ultraflat graphene[15] would potentially remove these defects over the entire GNMs surface. As shown in the inset of Fig. 3.6b, the synthesized GNM exhibited narrow neck-width of about ~20 nm with certain periodicity. This process also demonstrates that large area GNMs with desired neck-widths and periodicities could be attainable by changing the duration/power of RIE and the diameter of PS spheres, respectively.

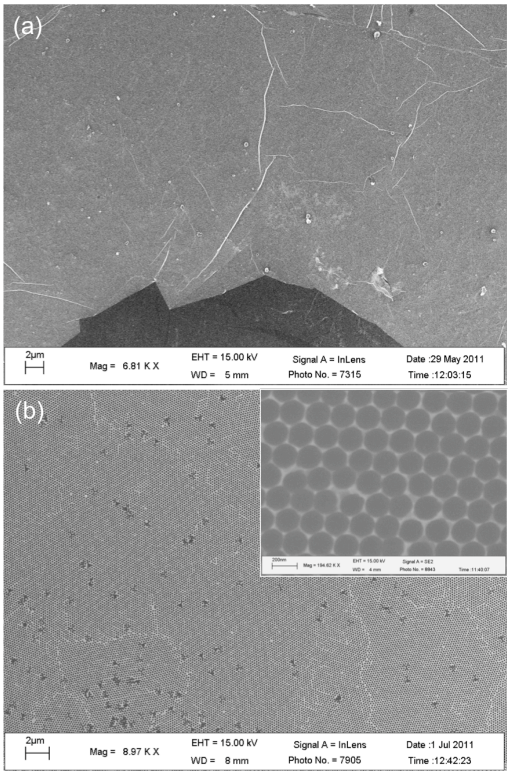

Figure 3.6 SEM images of large area a) CVD-grown polycrystalline graphene onto SiO_2/Si substrates and corresponding synthesized GNMs using PS nanosphere lithography.

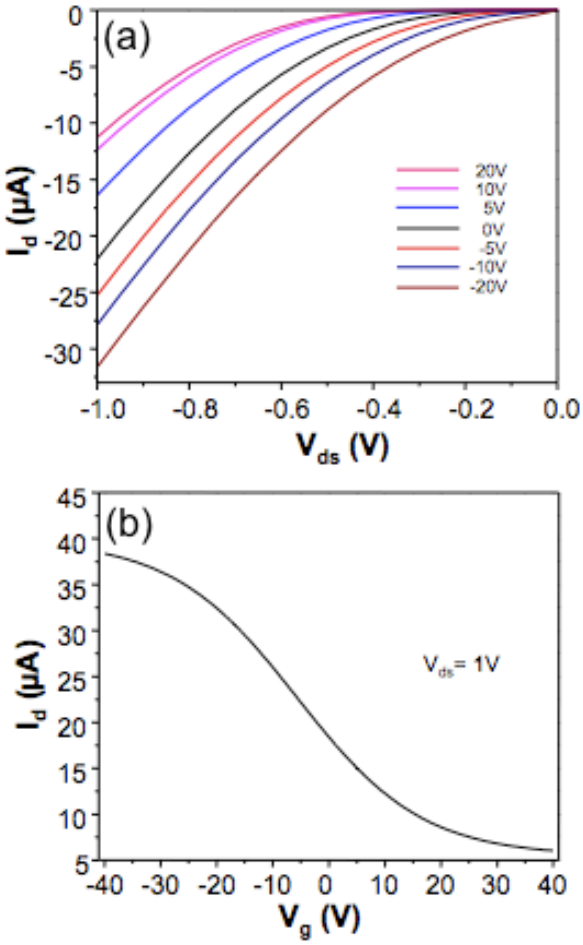

Figure 3.7 Electrical properties of synthesized GNM film. a) Low bias two terminal source–drain current–voltage (I_d–V_{ds}) and b) transfer (I_d-V_g) characteristic curves recorded on a GNM FET (L_c=3 μm and W_c=200 μm).

To investigate the electronic properties of fabricated GNM-based transistor, a three terminal transistor device was made using GNM as the semiconducting channel, e-beam evaporated Ti (20 nm)/Au (180 nm) source-drain contacts, a highly doped p-type Si

as global back gate, and 300 nm thermally grown SiO_2 as the gate dielectric. Figure 3.7 shows the electrical transport characteristics of the fabricated GNM transistor with a neck-width ~20 nm. Drain current (I_d) versus source-drain voltage (V_{sd}) with various gate voltages (V_g) of the GNM showed p-type transistor behavior (Fig. 3.7a). The hole doping of synthesized GNM can be attributed to the edge oxidation during the O_2 plasma process similar to the GNR-based transistor devices reported earlier.[2] The I_d-V_g curve (Fig. 3.7b) at a V_{sd} of 1 V showed I_{ON}/I_{OFF} ratio of ~6.5, which is higher than the ethanol-based graphene film (about 3),[10] and comparable to sub-20nm width GNR transistor device (about 5).[2] Further optimization of RIE conditions should easily allow to synthesize GNMs with narrower necks as described in Fig. 3.5, thus providing higher I_{ON}/I_{OFF} GNM transistor devices.

3.4 Conclusion

Using a simple polystyrene nanosphere lithography technique, we systemically investigated the process conditions and synthesized large-area graphene nanomesh from CVD-grown graphene film. In fact, this method can be scaled to wafer scale GNMs using the current wafer scale CVD grown graphene platform. The resulting neck-width of the synthesized nanomesh was about ~20 nm and comprised of the gap between polystyrene spheres that was formed during the reactive ion etching process. The neck-width and the periodicities of the graphene nanomesh could be easily controlled depending the duration/power of RIE and the size of PS nanospheres. Our demonstrated approach could

open up a way to fabricate various thin-film semiconductor nanomeshes for application in scalable nanoelectronics.

3.5 References

1. Novoselov, K. S.; Geim, A. K.; Morozov, S. V.; Jiang, D.; Zhang, Y.; Dubonos, S. V.; Grigorieva, I. V.; Firsov, A. A. Science 2004, 306, 666.

2. Li, X.; Wang, X.; Zhang, L.; Lee, S.; Dai., H. Science 2008, 319, 1229.

3. Bai, J.; Zhong, X.; Jiang, S.; Huang, Y.; Duan, X. Nat. Nanotechnol. 2010, 5, 190.

4. Kosynkin, D. V.; Higginbotham, A. L.; Sinitskii, A.; Lomeda, J. R.;Dimiev, A.; Price, B. K.; Tour, J. M. Nature 2009, 458, 872.

5. Higginbotham, A. L.;Kosynkin, D. V.; Sinitskii, A.; Sun, Z.; Tour, J. M. ACS Nano 2010, 4,2059.

6. Jiao, L.; Wang, X.; Diankov, G.; Wang, H.; Dai., H. Nat.Nanotechnol. 2010, 5, 321.

7. Bai, J.; Duan, X.; Huang, Y. Nano Lett. 2009, 9, 2083.

8. Sinitskii, A;M. Tour, J.M. J. Am. Chem. Soc. 2010, 132, 14730–14732.

9. Li, X. S.; Cai, W. W.; An, J. H.; Kim, S.; Nah, J.; Yang, D. X.; Piner, R. D.; Velamakanni, A.; Jung, I.; Tutuc, E.; Banerjee, S. K.; Colombo, L.; Ruoff, R. S. Science 2009, 324, 1312-1314.

10. Paul, R. K., Badhulika, S., Niyogi, S., Haddon, R. C., Boddu, V. M., Costales-Nieves, C., Bozhilov, K. N., Mulchandani, A., *Carbon*, **2011**, 49, 3789.

11. Lin, H.; Steyerl, A.; Satija, S. K.; Karim, A.; Russell, T. P.Macromolecules 1995, 28, 1470.

12. Xu, T.; Goldbach, J. T.; Misner, M. J.; Kim, S.; Gibaud, A.; Gang,O.; Ocko, B.; Guarini, K. W.; Black, C. T.; Hawker, C. J.; Russell, T.P. Macromolecules 2004, 37, 2972.

13. García, P.D.; Sapienza, R.; Blanco, A.; López. C. Adv. Mater. 2007, 19, 2597–2602.

14. Harton, S.E.; Luning, J.;Betz, H.; Ade, H.Macromolecules 2006, 39, 7729-7733.

15. Lui, C.H.; Liu, L.; Mak, K.F.; Flynn, G.W.; Heinz, T.F. Nature 462, 2009, 339-341.

CHAPTER 4

Large Area Graphene Nanomesh Synthesis for Chemiresistor Gas Sensors

Graphene, one of the carbon allotropes, has attracted significant attention as a promising sensor material because of the sensitivity towards different gaseous species and biomolecules. In this work, ethanol-chemical vapor deposition (CVD) grown p-type semiconducting large-area (~1 in^2) monolayer graphene film patterned into nanomesh by the combination of nanosphere- and optical-lithography was applied for chemiresistor gas sensor devices. The nanomesh sensor devices showed excellent sensitivity towards NO_2 and NH_3, significantly higher than their film counterparts. The change in conductance of the graphene nanomesh sensor devices in response to NO_2 or NH_3 was a combined result of high defects density, charge confinement and charge transfer effects. The ethanol-based graphene nanomesh sensor devices exhibited sensitivities of about 4.32%/ppm in NO_2 and 0.71%/ppm in NH_3 with estimated limit of detections of 15 ppb and 160 ppb, respectively. Our demonstrated studies on the sensing properties of graphene nanomesh would lead to further improvement of its sensitivity and selectivity as a potential sensor material.

4.1 Introduction

Nanostructured materials are promising candidates as sensor elements due to their high surface-to-volume ratio that potentially leads to exceptional device performance, reduced device size and low power consumption.[1-4] Chemiresistor and field-effect transistors based sensors are the most common type and simplest sensors. In these types of sensors, the modulation of electrical resistance/conductance of the sensing element resulting from the interaction with the analyte is measured using a simple ohmmeter. Graphene, a one atom thick sp^2 hybridized two-dimensional honeycomb lattice of carbon with extraordinary mechanical, thermal and electronic properties is an interesting nanomaterial that is receiving significant attention for chemiresistor (CR) and field-effect-transistor (FET) sensor devices.[5-8] Recently, there have been several reports in the literature demonstrating application of graphene for CR/FET chemical and biological sensors.[9,10] However, the material used, in all but one of the reported devices was chemically derived graphene, i.e. graphene oxide (GO). Although elegant, there are significant drawbacks in full-scale development of devices made from derived graphene/GO. First, GO is inherently insulating and hence it has to be reduced before it is useful as the conduction channel of CR/FET. Second, because of variability in the degree of reduction of the GO making the conduction channel of CR/FET there could be a problem in device-to-device reproducibility. Third, the expansion/exfoliation method used for producing GO produces micron size multilayer flakes of random geometry, which while suitable for single device fabrication for demonstration purposes have serious limitations in fabrication of large numbers of devices with reproducible performance. These drawbacks can be alleviated

using graphene or derivatized graphene with uniform morphological, chemical and electrical properties. This can be achieved by synthesizing graphene at wafer level using chemical vapor deposition. However, CVD produced graphene although semiconducting has zero bandgap and FET devices made with such graphene cannot be truly turned off and hence cannot compete with conventional complementary metal-oxide-semiconductor (CMOS) devices in terms of I_{ON}/I_{OFF} ratio. Recently, it has been shown theoretically and experimentally that lateral confinement of the graphene into sub-10 nm wide graphene nanoribbons (GNRs) could induce a bandgap by the quantum confinement and edge effects.[11] The bandgap of a GNR is related with the ribbon width by the equation[12] $Eg = 0.8/W$, where Eg is the bandgap and W is the ribbon width in nanometer. Several reports have been published over the last few years showing the ability of bandgap tuning of ultra-narrow GNRs and their possible applications in nanoelectronics.[13-17] However, single GNR devices usually show low driving currents or low transconductances. Thus, despite the promising electronic properties, single GNR devices cannot be applied on the platform of scalable electronics because there is no state-in-the-art technique to integrate them in a wafer scale circuitry. Moreover, patterning of wafer scale chemical vapor deposition (CVD)-grown graphene into sub-10 nm dimensions is still challenging with the e-beam lithography.

Recently, an approach named block copolymer lithography was reported to pattern micron-size exfoliated graphene into graphene nanomesh (GNM).[18] The resulting GNMs exhibited large enough bandgap to be used as a semiconducting channel in a FET. In fact, GNM-FET devices showed high I_{ON}/I_{OFF} ratio with remarkably higher driving

currents than single GNR-FET devices. The narrow neck-width of GNM confines the charge while being used as channel in an FET device. However, the size of the synthesized GNM is limited to the micron-sized exfoliated graphene. Thus, synthesis of large area graphene nanomesh needs to be demonstrated using the state-of-art techniques to achieve larger device density for realizing its practical applications.

Recently, we showed that ethanol-based CVD grown graphene (gEtOH) exhibited a p-type semiconducting behavior due to the polycrystalline nature as opposed to the ambipolar electron transfer characteristics of methane-based CVD grown graphene (gCH_4).[19,20] In the two-dimensional (2D) polycrystalline gEtOH, grain boundaries are the one-dimensional (1D) interfaces between two crystalline domains with different crystallographic orientations. In fact, the grain boundaries and oxygenated functional groups present in the polycrystalline gEtOH act as defect sites to induce short-range charge disorder leading to higher I_{ON}/I_{OFF} ratio in a gEtOH FET device.[20] In this work, we report large area patterning of graphene film into GNM using a simple reactive-ion-etching (RIE) modified polystyrene (PS)-nanospheres-lithography technique and its application as gas sensors for toxic gases NO_2 and NH_3 that affect human health. We also fabricated sensor devices using graphene films to compare their sensitivity to nanomesh counterparts. Fabricated gEtOH nanomesh sensor devices showed room temperature limit of detections of 15 ppb and 160 ppb in NO_2 and NH_3, significantly lower than Occupational Safety and Health Administration (OSHA) permissible exposure limits of 5 ppm (NO_2) and 50 ppm (NH_3), respectively.

4.2 Experimental Procedure

Growth of large area graphene film and patterning into graphene nanomesh (GNM): Large area (~1 in^2) graphene films grown by methane-CVD[19] and ethanol-CVD[20] processes were transferred onto SiO_2/Si substrate. PMMA was spin-coated over the graphene/SiO_2/Si substrates and baked at 110°C for 5min, followed by O_2 plasma etching for 40 sec to make the surface hydrophilic. A stock solution consist of 10 wt% PS nanospheres (200 nm average diameter; Alfa Aesar) was ultra-sonicated in ethanol/water (1:1) solution for 30 min to disperse the PS nanospheres properly. A few drops of the stock solution were added on the D.I. water surface in a petri dish. In this step, several islands of monolayer PS nanospheres were visible on the water surface. Interestingly, a drop of SDS (1%) solution immediately assembled those islands into a large area compact monolayer film of PS nanospheres on the water surface. The PMMA coated graphene/SiO_2/Si substrate was then brought into the contact of PS monolayer film on the water surface and easily transferred to cover the whole substrate, followed by drying in room temperature. Reactive ion etching (RIE; O_2) was then employed at 75 W for 10 sec in flowing 50 sccm O_2 to define 15-20 nm gap (comprised of resulting neck width of GNMs) between the nanospheres. A 15 nm Pt was deposited over the substrate using an e-beam evaporator (Temescal, BJD-1800) to fill up the gaps. A lift-off in 1-choropentane (Sigma) at 60°C for 2 h confirmed selective and complete removal of the PS nanosphere to result a perfect Pt nanomesh mask. In the second RIE step, the substrate was exposed to O_2 plasma at 75 W for 150 sec in flowing 50 sccm O_2 to remove the PMMA/graphene

in the unprotected areas from Pt nanomesh. A second lift-off was carried out in acetone removed Pt nanomesh mask and PMMA to form GNM over SiO_2/Si substrate.

Gas sensing measurements of GNMs sensor: GNMs sensor devices were fabricated by writing finger-like source-drain Ti (20 nm)/Au (180 nm) electrodes with 3 μm channel length defined by optical lithography. The samples were then mounted on a chip holder and wire bonded to complete fabrication of GNM chemiresistor gas sensor devices. GNM sensors were then placed inside 1.3 cm^3 glass chamber with inlet and outlet ports. Dry air or air/NO_2mixtures or air/NH_3 mixtures was supplied into the glass chamber maintaining a total flow rate of 200 sccm controlled by mass flow controllers (MFCs). The sensor arrangement was subjected to 1 V source-drain (V_{sd}) bias and the two-probe resistance across the sensor was recorded continuously using a dual channel Keithley Source Meter (Model 2363A). A custom Labview program was developed to control the MFCs and monitor the resistance of the GNMs sensor devices. The sensor device was first purged with dry air for 200 min until the resistance of the sensors stabilized, followed by increasing NO_2 or NH_3 concentration in dry air every 15 min with an interval of 20 min recovery in air between two NO_2 or NH_3 exposures.

4.3 Results and Discussion

Large-area graphene films were synthesized by chemical vapor deposition techniques using EtOH and CH_4 as carbon precursors, and transferred onto SiO_2 (300nm)/Si substrate (see detailed experimental section).[19,20] For GNM synthesis, PMMA coated graphene/SiO_2/Si substrates was used as the platform for nanosphere

lithography. PS nanospheres from a stock solution were spread on deionized (D.I.) water surface to form a large-area compact monolayer film of PS nanosphere on water surface. The total area of the assembled compact monolayer PS spheres can readily be increased depending on the area of water surface and the amount of PS stock solution. Thus, this method can be easily scaled to the current wafer scale CVD grown graphene to synthesize wafer scale GNM. The PS nanospheres monolayer film was transferred onto PMMA coated graphene/SiO_2/Si substrate by contacting the substrate with the PS nanospheres monolayer film floating on water followed by drying the substrate in room temperature as shown in Figure 4.1a. Reactive-ion-etching (RIE; O_2) was then employed to define the desired gaps (comprised of resulting neck width of GNMs) between the PS nanospheres by the reduction of each PS nanosphere size, as shown in Figure 4.1b. Subsequently, Pt was deposited over the substrate using an e-beam evaporator to fill up the gaps. Complete removal of PS nanospheres was then carried out in 1-chloropentane to form a continuous Pt nanomesh mask over PMMA/graphene/SiO_2/Si substrate as shown in Figure 4.1c. 1-chloropentane selectively dissolves PS nanospheres without reacting to the PMMA. Therefore, this lift-off approach results in the formation of continuous Pt nanomesh mask, as opposed to the removal of PS nanospheres by ultrasonication that often damages the Pt nanomesh. In the second RIE step, the substrate was exposed to O_2 plasma again to etch the PMMA/graphene in the unprotected areas. Second lift-off was performed in acetone to remove Pt nanomesh mask and PMMA to form GNM over SiO_2/Si substrate as shown in Figure 1d. The average neck width of the GNM was ~20

nm. The neck width of the resulting GNM can be controlled depending on the RIE etching time of PS nanospheres.

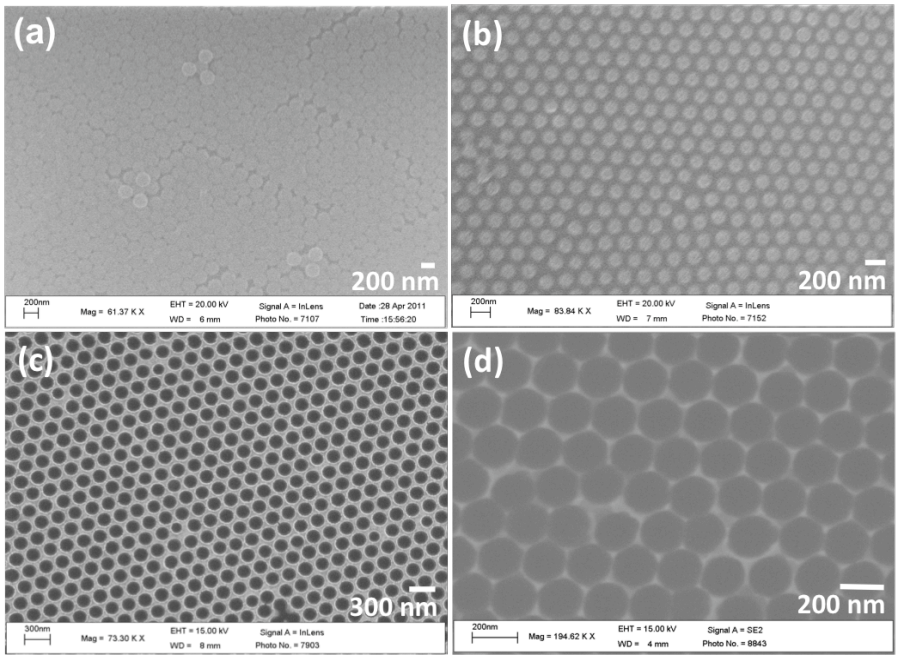

Figure 4.1 SEM images of self-assembled monolayer of PS spheres onto PMMA/gEtOH/SiO_2/Si substrate a) before and b) after 10 sec RIE etching. c) Formation of Pt nanomesh mask onto PMMA/gEtOH/SiO_2/Si substrate by removal of PS spheres in 1-chloropentane. d) gEtOH nanomesh onto SiO_2/Si substrate after etching of PMMA/gEtOH films in the unprotected areas, followed by removal of Pt nanomesh mask and PMMA using lift-off in acetone.

To evaluate the application of GNM for chemiresistor sensors, gEtOH and gCH_4 nanomesh were applied as conduction channel between a pair of photolithographically defined Ti/Au electrodes, acting as source and drain, separated by a 3 mm gap. For comparison, sensor devices made of gEtOH and gCH_4 film conduction channels were

also evaluated. To start, the devices were tested for their response (normalized resistance change) to 1 ppm NO_2. As illustrated in Fig. 4.2a, gEtOH nanomesh sensor exhibited the best response (~6%) followed by gCH_4 nanomesh sensor (~4.5%) whereas there was no response from their film counterparts. The decrease in resistance of the device is attributed to increase in hole-density of p-type semiconductor graphene upon adsorption the electron acceptor NO_2. The very good response from GNM devices compared to the film counterparts is attributed to the formation of large number of edges in the nanomesh structure that leads to hole doping by edge-oxidation during the O_2 plasma process and/or physisorbed oxygen from the ambient and other species during the sample preparation steps similar to that of GNRs devices.[22,23] On the other hand, the narrow neck regions of GNM controls the charge transport across the source-drain electrodes by lateral quantum confinement, leading to higher sensitivity while being exposed to electron donating or withdrawing gas/bio molecules.[21]

Figure 4.2b and 4.2c show the dynamic responses and calibration plots, respectively, of chemiresistor sensors made with gEtOH and gCH_4 GNM and films as conduction channel operating at room temperature for increasing NO_2 concentrations. Similar to response for 1 ppm NO_2, the responses over the tested range of 1 to 10 ppm NO_2 was in the order, gEtOH nanomesh > gCH_4 nanomesh > gEtOH film > gCH_4 film. Further, the response time, defined as the time required reaching a 90% of the maximum resistance change of the sensor, for GNM sensors at 1 ppm NO_2 in dry air was approximately 7 min and decreased to 5 min at 10 ppm. The relationship between the sensor response and concentration (Fig. 4.2c) exhibited the Langmuir-like absorption

isotherm, where the relationship between the response and concentration is governed by the eqn.

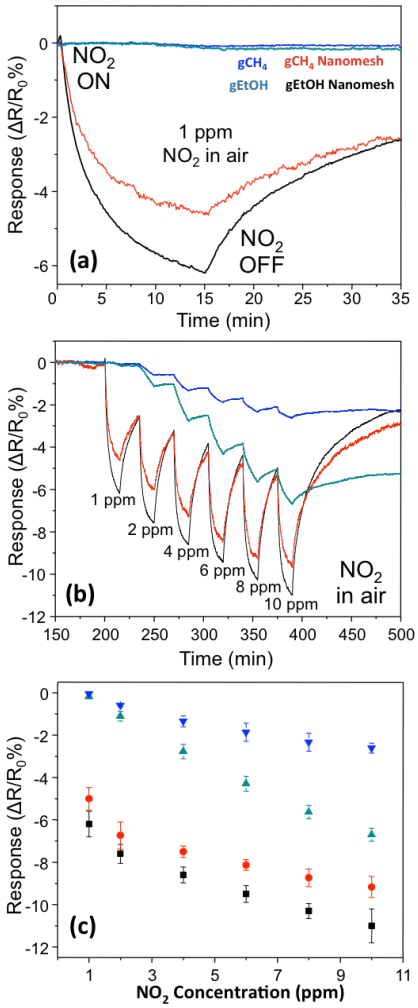

Figure 4.2. a) Comparison of dynamic responses of sensor devices fabricated from gCH_4 and gEtOH nanomesh and their continuous film counterparts to 1 ppm NO_2 in dray air. b) Comparison of dynamic responses of sensor devices fabricated from gCH_4 and gEtOH nanomesh and their continuous film counterparts exposed to various concentrations of NO_2 in dry air ranging from 1 ppm to 10 ppm, as labeled. c) Calibration curves of gCH_4 and gEtOH nanomesh sensor devices in various concentrations NO_2 in dry air.

$$\frac{\Delta R}{R_O} = \left(\frac{\Delta R}{R_O}\right)_{\max} \bullet \frac{c}{k+c}$$

where $\left(\Delta R / R_O\right)_{\max}$ is the maximum change in normalized resistance occurring in the saturation regime, and k is the affinity constant. The sensitivity (slope of the linear part of calibration curve) and estimated limit of detection (defined as LOD=$3S_D$/m, where m is the slope of linear part of the calibration curve and S_D is the standard deviation of noise in the response curve in dry air) of the gEtOH nanomesh NO_2 sensor were determined to be 4.32%/ppm and 15 ppb (parts-per-billion), respectively. This result is comparable to the 3.5%/ppm sensitivity and 1 ppm LOD reported for a three-dimensional CNTs (20μm)/reduced graphene hybrid NO_2 sensor.[24]

Graphene has similar graphitic structure as CNTs, and thus exhibit similar working principle of electrical conductivity modulation by the charge transfer mechanism in detecting gas molecules adsorbed at its surface. However, it has been recognized that pristine CNTs exhibit weak binding energies to the foreign molecules and thereby show poor reactivity at their defect-free surfaces due to small charge transfers from the adsorbed molecules. In fact, in our previous work we demonstrated that compared to CVD-synthesized gCH_4 film, CVD-synthesized gEtOH film exhibits polycrystallinity containing highly disordered sp^3 hybridization, large number of edge defects and oxygenated functional groups, affecting it's electronic and transport properties.[20] Figure 3 shows a schematic diagram (not to scale) comparing the structural differences between gCH_4 and gEtOH nanomesh sensor devices. The gCH_4 nanomesh contains defects mostly formed due to the formation the edges of nanoholes during nanosphere lithography (Fig.

4.3a), whereas gEtOH nanomesh had additional unsaturated grain boundary (intrinsic topological defect as labeled by colored pentagons and heptagons) due to its polycrystalline nature (Fig. 4.3b), which could modulate the charge transport properties.[25,26] Moreover, the higher defects density of the oxygenated gEtOH films could modify the local electronics-charge distribution, enhancing the reactivity at those specific sites.[27,28] These highly reactive defects of gEtOH film or nanomesh give rise to higher sensitivity by the adsorption of maximum number of NO_2 molecules. This is also evident in the NO_2 response curves of GNM devices. As shown in Figures 4.2a and 4.2b, both gEtOH and gCH_4 nanomesh devices had almost similar response time but different response intensities. The gCH_4film/nanomesh had lesser defect sites than gEtOH film/nanomesh to have less number of NO_2 molecules adsorbed on the surface as shown in Figure 3, limiting the low conductivity modulation.

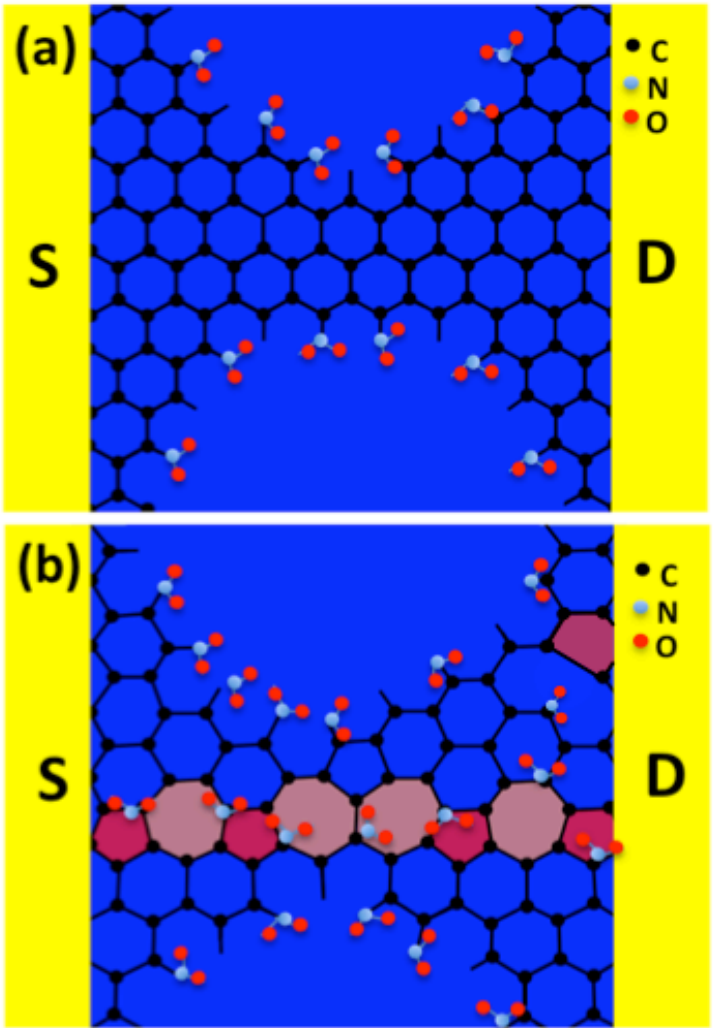

Figure 4.3 A structural representation (not in scale) comparing the defect densities between a) gCH_4 and b) gEtOH nanomesh sensor devices, and adsorptions of NO_2 molecules on the defect sites. A typical intrinsic defect (grain boundary) of polycrystalline gEtOH nanomesh labeled as colored unsaturated carbon (pentagons and heptagons) structure in b).

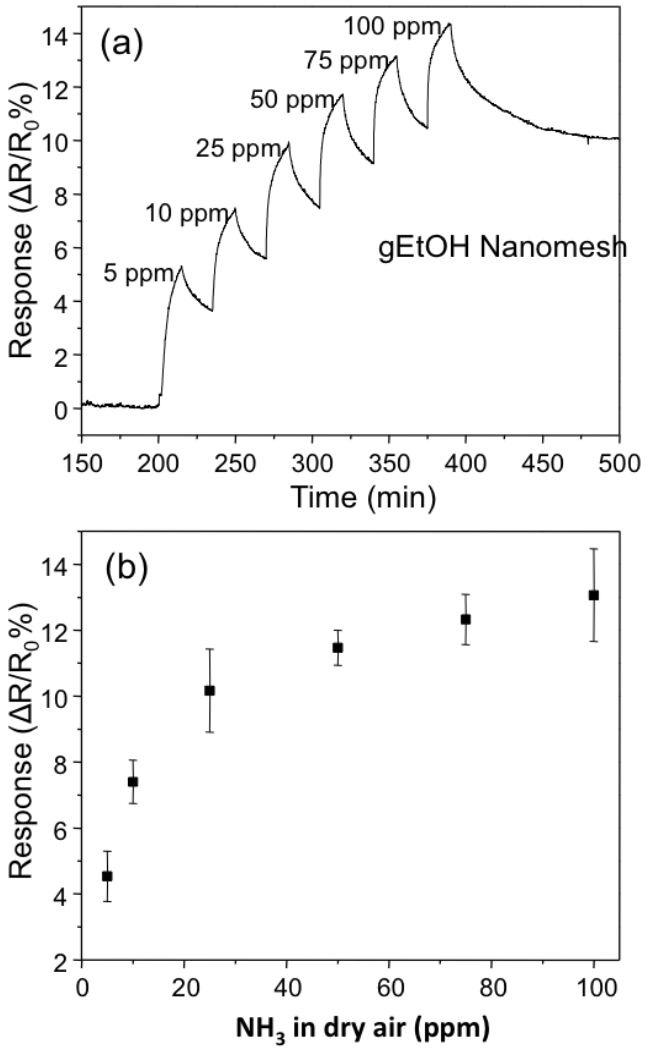

Figure 4.4 a) Dynamic response and b) calibration curve of gEtOH nanomesh sensor device exposed to various concentrations of NH_3 in dry air ranging from 5 ppm to 100 ppm, as labeled.

Furthermore, similar to the case of carbon nanotubes,[29,30] the resistance of the GNM sensor devices increased when exposed to NH_3 (an electron donor), (Fig. 4.4a). This result suggests that the response of p-type gEtOH nanomesh sensor device in NH_3

exposures is due to the depletion of holes during the electron transfer from NH_3 molecules to the nanomesh surface.[31,32] There is a monotonic increase in responses with the increasing NH_3 concentrations ranging from 5 ppm to 100 ppm in dry air. The sensitivity and estimated LOD of gEtOH sensor devices calculated from the calibration curve in Figure 4.4b were about 0.71%/ppm and 160 ppb, respectively.

4.4 Conclusion

Large area graphene nanomeshes with certain periodicity were synthesized using the combination of chemical vapor deposition and nanosphere lithography techniques. Fabricated graphene nanomesh sensor devices containing narrow neck width of about ~20 nm represented remarkably higher sensitivity to both NO_2 and NH_3 exposures than their film counterparts. Due to the higher defect density, ethanol-derived graphene nanomesh sensor showed enhanced responses and sensitivity than the methane-derived graphene nanomesh devices by the adsorption of maximum number of gas molecules. The sensitivity and estimated limit of detection of ethanol-based graphene nanomesh devices were about 4.32%/ppm and 15 ppb in NO_2, and 0.71%/ppm and 160 ppb in NH_3, respectively. These results revealed that the fabricated GNM sensors could be successfully used for detection of other electron-donating or electron-withdrawing species. Further, the decrease in neck width of synthesized nanomesh and/or surface modification of those nanomesh sensor devices with polymers or catalyst nanoparticles would increase the sensitivity further with possible selectivity.

4. 5 References

[1] Y. N. Xia, P. D. Yang, Y. G. Sun, Y. Y. Wu, B. Mayers, B. Gates, Y. D. Yin, F. Kim, Y. Q. Yan, *Adv. Mater*. **2003**, 15, 353.

[2] P. Qi, O. Vermesh, M. Grecu, A. Javey, Q. Wang, H. J. Dai, *Nano. Lett*. **2003**, 3, 347.

[3] J. L. Johnson, A. Behnam, S. J. Pearton, A. Ural, *Adv. Mater*. **2010**, 22, 4877.

[4] R. K. Paul, S. Badhulika, A. Mulchandani, *Appl. Phys. Lett*. **2011**, 99, 033103.

[5] K. S. Novoselov, A. K. Geim, S. V. Morozov, D. Jiang, Y. Zhang, S. V. Dubonos, I. V. Grigorieva, A. A. Firsov, *Science* **2004**, 306, 666–9.

[6] I. W. Frank, D. M. Tanenbaum, A. M. Van der Zande, P. L. McEuen,*J. Vac. Sci. Technol. B* **2007**,25**,** 2558.

[7] A. A. Balandin, S. Ghosh, W. Z. Bao, I. Calizo, D. Teweldebrhan, F. Miao, C. N. Lau, *Nano Lett*. **2008**, 8**,** 902.

[8] A. K. Geim, K. S. Novoselov, *Nat. Mater*. **2007**, 6 183.

[9] G. Lu, S. Park, K. Yu, R. S. Ruoff, L. E. Ocola, D. Rosenmann, J. Chen, *ACS Nano*, **2011**, 5, 1154.

[10] T. Kuila, S. Bose, P. Khanra, A. K. Mishra, N. H. Kim, J. H. Lee, *Biosensors and Bioelectronics*, **2011**, 26, 4637.

[11] K. T. Lam, D. Seah,S. K. Chin, S. B. Kumar, G. Samudra,Y. C. Yeo,G. Liang,*IEEE Electron Device Lett*. **2010**, 31, 555.

[12] X. Li, X. Wang,L. Zhang,S. Lee, H. Dai, *Science* **2008**, 319, 1229.

[13] K. A. Ritter,J. W. Lyding, *Nat. Mater*. **2009**, 8, 235.

[14] T. S. Shimizu, J. Haruyama, D. C. Marcano, D. V. Kosinkin, J. M. Tour, K. Hirose,K. Suenaga,*Nat. Nanotechnol.* **2011**, 6, 45.

[15] J. W. Bai, R. Cheng, F. X. Xiu, L. Liao, M. S. Wang, A. Shailos, K. L. Wang, Y. Huang, X. F. Duan, *Nat. Nanotechnol.* **2010**, 5, 655.

[16] L. Jiao, X. Wang,G. Diankov, H. Wang,H. Dai, *Nat. Nanotechnol.* **2010**, 5, 321.

[17] M. Sprinkle, M. Ruan, Y. Hu, J. Hankinson, M. Rubio-Roy, B. Zhang, X. Wu, C. Berger, W. A. de Heer, *Nat. Nanotechnol.* **2010**,5, 727.

[18] J. Bai, X. Zhong, S. Jiang, Y. Huang, X. Duan, *Nat. Nanotechnol.* **2010**, 5, 190.

[19] X. S. Li, W. W. Cai, J. H. An, S. Kim, J. Nah, D. X. Yang, R.D. Piner, A. Velamakanni, I. Jung, E. Tutuc, S. K. Banerjee, L. Colombo, R.S. Ruoff, *Science* **2009**, 324, 1312.

[20] R. K. Paul, S. Badhulika, S. Niyogi, R. C. Haddon, V. M. Boddu, C. Costales-Nieves, K. N. Bozhilov, A. Mulchandani, *Carbon*, **2011**, 49, 3789.

[21] F. Schedin, A. K. Geim, S. V. Morozov, E. W. Hill, P. Blake, M. I. Katsnelson, K. S. Novoselov, *Nat. Mater.* **2007**, 6, 652.

[22] T. C. Li, S. P. Lu, *Phys. Rev. B* **2008**, 77, 085408.

[23] F. Sols, F. Guinea, A. H. Castro Neto, *Phys. Rev. Lett.* **2007**, 99, 166803.

[24] H. Y. Jeong, D. S. Lee, H. K. Choi, D. H. Lee, J. E. Kim, J. Y. Lee, W. J. Lee, S. O. Kim, S. Y. Choi, *Appl. Phys. Lett.* **2010**,96, 213105.

[25] P. Kim, *Nat. Mater.* **2010**, 9, 792.

[26] O. V. Yazyev, S. G. Louie, *Nat. Mater.* **2010**, 9, 806.

[27] Z. Zanolli, J. C. Charlier, *Phys. Rev. B* **2009**, 80, 155447.

[28] K. N. Kudin, B. Ozbas, H. C. Schniepp, R. K. Prud'homme, I. A. Aksay, R. Car, *Nano Lett*. **2008**, 8, 36.

[29] P. G. Collins, K. Bradley, M. Ishigami, A. Zettl, *Science* **2000**, 287,1801.

[30] J. Kong, N. R. Franklin, C. Zhou, M. G. Chapline, S. Peng, K. Cho, H. Dai, *Science* **2000**, 287, 622.

[31] R. S. Sundaram, C. Gomez-Navarro, K. Balasubramanian, M. Burghard, K. Kern, *Adv*. *Mater*. **2008**, 20, 3050.

[32] J. Kong, M. G. Chapline, H. Dai, *Adv*. *Mater*. **2001**, 13, 1384.

CHAPTER 5

Platinum Nanoflowers Decorated Three-Dimensional Graphene/Carbon Nanotubes Electrode for Methanol Oxidation

A three-dimensional (3D) carbon electrode in the form of vertically oriented oriented multiwalled carbon nanotubes (MWNTs) on a graphene floor was transferred onto glassy carbon electrode (GCE) as supporting materials for for platinum (Pt) electrocatalyst. Pt nanoparticles were electrochemically deposited deposited over these carbon based support materials and the resulting Pt/G-Pt/G-MWNTs/GCE was characterized by scanning electron microscopy (SEM), (SEM), energy dispersive spectroscopy (EDS), cyclic voltammetry (CV) and and electrochemical impedance spectroscopy. The electrocatalytic properties of the properties of the modified electrode for electro-oxidation of methanol have been have been investigated by CV. Experimental results demonstrates an enhanced enhanced efficiency of the G-MWNTs hybrid film, as catalyst support, for methanol methanol oxidation in comparison to Pt nanoparticles graphene and glassy carbon carbon with regard to electroactive surface area, forward anodic peak current current density, onset oxidation potential, diffusion efficiency and the ratio of ratio of forward to backward anodic peak current density (I_f/I_b). This enhanced

enhanced catalytic performance towards methanol oxidation is due to the high high surface area of three-dimensional G-MWNT hybrid film, allowing higher higher dispersion of Pt together with excellent electrical properties of MWNTs.

MWNTs.

5.1 Introduction

Direct methanol fuel cell (DMFC) is an attractive power source for portable electronic devices and automobiles[1]. However, the conversion of chemical energy into electricity in direct methanol fuel cells (DMFCs) requires significant development of better catalysts to improve the cell performance. With the development of nanotechnology, nanostructured materials offers new avenues for searching and designing effective electrocatalysts, which have attracted attention of many researchers and advances the progress in this field. Among the nanocatalysts, platinum (Pt) based catalyst has been considered as the best electrocatalyst in the low temperature fuel cells.[2] The methanol oxidation at electrode surface in acidic electrolyte is an electrocatalytic process, in which CO_2 and six electrons are produced. However, there are some critical factors that limit the particular application of methanol fuel cell, including sluggish kinetics of methanol oxidation at anode and the high cost of noble Pt-based catalysts. Therefore, the development of support material with high surface area is of considerable interest to effectively disperse catalyst particles and to reduce the catalyst loading with enhancing the catalytic activity for the eletrooxidation of methanol. RuPt nanoalloys

coated carbon black in the form of well-dispersed $Pt_{50}Ru_{50}$ particles are frequently used in commercial anode catalysts in DMFCs.[3]

High-surface-area carbon nanostructures such as carbon nanotube (CNT) and carbon nanofibres have been used extensively for the oxidation of methanol because of their micro- and macro-structural characteristic.[4-6] The CNTs have excellent intrinsic properties such as their unique morphology including inherent size and hollow geometry, high electrical conductivity and good chemical stability that that make them promising supports materials for heterogeneous catalysts.[7] The recent emergence of graphene, one-atom thick planar sheet of hexagonally arrayed sp^2 carbon atoms, in many technological fields, such as nanoelectronics, nanocomposites, batteries and supercapacitors[8] has opened a new opportunity for utilizing this 2D carbon material as a heterogeneous catalyst support in direct methanol fuel cells [9-11]. However, graphene films are mostly produced by exfoliating graphite and are limited to small sizes (<1000 μm^2). Since large size graphene films are required for making large transparent - electrode, it has been grown on a number of metals [12]. Recently, a single layer graphene was grown on copper at a temperature of 1000 °C by chemical vapor deposition (CVD) of carbon using a mixture of methane and hydrogen [13]. On the one hand, significant efforts have also been made to synthesize high-surface-area graphene-based composites as electrode materials to achieve high catalytic activity. On the other hand, synthesis of noble electrocatalyst nanoparticles with uniform size and good dispersion over the carbon supports, as an electrocatalytic material also remained to be a demanding work. Keeping this in view, a

one-step CVD-grown large-area 3D G-MWNTs hybrid nanosructure, composed of multiwall carbon nanotubes (MWNTs) and graphene film, was transferred onto a glassy carbon electrode (GCE) to fabricate a heterogeneous catalyst support (G-MWNTs/GCE). Pt-nanoparticles were electrochemically deposited onto G-MWNTs/GCE, graphene/GCE and GCE for comparative investigation of their catalytic properties for electrochemical oxidation of methanol.

5.2 Experimental Procedure

Graphene was grown by acetylene (C_2H_2)-chemical vapor deposition (CVD) process on a copper foil (~2.54cm^2) using a CVD technique as reported previously. In brief, a piece of copper foil was decorated with 1 nm thick iron nanoparticles using an e-beam evaporator (Temescal, BJD-1800). The iron nanoparticles and Cu foil were acted as catalysts for MWNTs growth and graphene, respectively. The growth substrates were placed inside a fused silica tube (5 cm inside diameter by 100 cm long) and the temperature raised to 700-770°C, under flowing Ar/H_2, 100 sccm (standard cubic centimeter per min)/50 sccm, atmosphere. A 50 sccm flow of C_2H_2 was supplied for 10 min in the tube once the temperature stabilized at growth temperature. After the growth process, the MFC for C_2H_2 was turned off, followed by cooling the furnace to room temperature in flowing Ar/H_2 atmosphere. Graphene film formed on the backside of the Cu foil was removed by O_2 plasma, followed by etching of the Cu foil in a 1 M aqueous $FeCl_3$ solution to collect single layer graphene and/or G-MWNTs film grown on the other

side. Subsequent cleaning of the films was performed with an aqueous HCl (5%) and deionized (D.I.) water for several times.

GC electrodes (3 mm diameter) were polished first with emery paper and then with aqueous slurries of fine alumina powder (1 and 0.05 μm) on a polished cloth, and finally rinsed with D.I. water in an ultrasonic bath for 5 min. Single layer graphene and G-MWNTs hybrid films were transferred over GCE, followed by drying at 50°C temperature for 1 hr in oven to obtain the graphene/GCE and G-MWNTs/GCE electrodes, respectively.

Electrocatalyst precursor salts, i.e., $H_2PtCl_6.6H_2O$ and $RuCl_3$, were purchased from Sigma. All other chemicals were of analytical grade and used as received without further purification. Double distilled water was used through all experiments. All the experiments were carried out at room temperature. Pt nanoparticles were electrochemically deposited onto the bare GCE, G-MWNTs hybrid film modified GCE and single layer graphene modified GCE by potential sweeping of 25 CV cycles each between +0.30 and -0.70 V, at a scan rate of 50 mV sec^{-1}, in 0.1 M HCl solution containing 5mM $H_2PtCl_6.6H_2O$, under identical experimental conditions**.** The Pt/G-MWNTs/GCE, Pt/graphene/GCE and Pt/GCE so obtained were washed with D.I. water and dried at 50°C temperature for 30 min, in oven, under vacuum. RuPt/G-MWNTs/GCE was prepared from an equimolar solution mixture of 0.25 M each $H_2PtCl_6.6H_2O$ and $RuCl_2$ in a cyclic voltammetry mode with 25 potential cycles between the same potential window, under identical conditions, as mentioned above for Pt deposition.

Detailed materials characterization of the synthesized films was performed using transmission electron microscopy (TEM; Philips, CM300, Japan), scanning electron microscopy (SEM; Leo, 1550) and Energy dispersion spectroscopy (EDS; Leo, 1550). Electrochemical characterization was performed with a CHI 750C (CH instruments Inc., USA). A three-electrode system was employed, while the Pt nanoparticles modified electrode (Pt/G-MWNTs/GCE, Pt/graphene/GCE or Pt/GCE) was the working electrode, Ag/AgCl with KCl solution acted as the reference electrode, and the platinum wire was the counter electrode. All cyclic voltammetric measurements were performed for at least three cycles, until a reliable and repeatable response was achieved and data presented were taken from the 3rd cycle.

5.3 Results and Discussion

Scanning electron microscopy (SEM) and transmission electron microscopy (TEM) studies were employed to investigate the morphologies of as prepared G-MWNTs hybrid film As shown in the SEM image (Fig. 5.1a), the one-step G-MWNTs synthesis method produced a highly dense MWNTs of an average tube diameter of 30 nm growing uniformly over the entire large-area graphene surface. A low magnification TEM image of PGN hybrid film transferred on a lacey carbon-supported Cu TEM grid (Fig. 5.1a) depicts growth of MWNTs from graphene surface. In the 1 nm Fe nanoparticles decorated Cu substrate, Fe and Cu were acting as metal catalysts for MWNT and graphene growth, respectively, during the one-step CVD growth process at 750°C in flowing Ar (100 sccm)/H_2 (50 sccm)/C_2H_2 (50 sccm) atmosphere. In the unique catalyst

system of Fe decorated Cu substrate, the MWNTs growth was made possible by typical vapor-liquid-solid (VLS) mechanism, whereas the graphene growth occurred by surface catalysis mechanism. In the bottom view of G-MWNTs hybrid film (Fig. 5.1b), the individual MWNT's root had highly crystalline contact with the graphene floor showing hollow circular pattern (as shown with dotted circles) comprising of typical carbon-carbon covalent bond between the two carbon allotropes.[17] This crystalline contact between MWNTs and graphene would remarkably reduce the contact resistance to achieve maximum charge transfer through the G-MWNTs hybrid system.

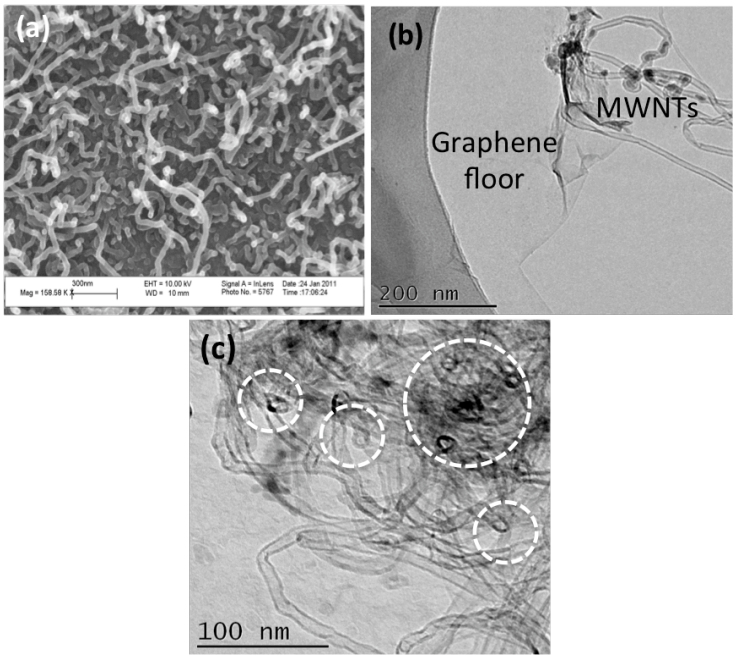

Figure 5.1. SEM and TEM images of the G-MWNTs hybrid film. (a) G-MWNTs film composed of vertically grown MWNTs on graphene floor, covering the GCE electrode, (b) MWNTs growth from graphene surface and (c) bottom view of G-MWNTs hybrid film showing crystalline contact between individual MWNT's root (dashed circles) and the graphene surface.

Figures 5.2a and 5.2b show SEM micrograph and EDS profile (insets) of G-MWNTs after electrodeposition of Pt and PtRu nanoparticles, respectively. As evident from the images, the electrodeposition conditions employed in this work produced a uniformly distributed flower-like structure comprising clusters of needles/flakes with needle size of 60-90 nm in case of Pt alone, and a combination of both spherical and needle like bimetallic

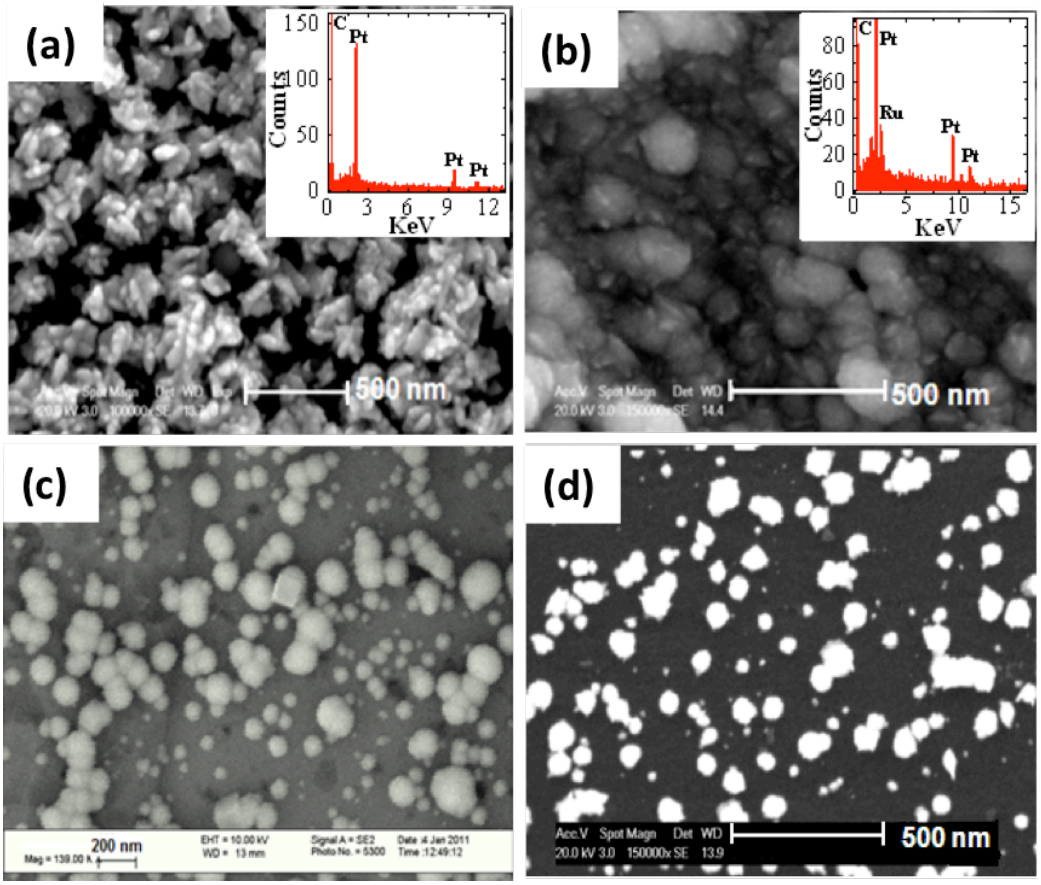

Figure 5.2 SEM images of a) Pt/G-MWNTs/GCE (inset shows EDS pattern), b) RuPt/G-MWNTs/GCE (inset shows EDS pattern), c) Pt/graphene/GCE and d) Pt/GCE.

particles in the case of PtRu, were formed over the hybrid film producing a high surface-to-volume catalyst over the G-MWNTs hybrid. In comparison, identical electrodeposition conditions on monolith graphene resulted in Pt nanoparticles ranging from 20-200 nm diameter having a few aggregated clusters of particles spread out on the graphene film (Fig. 5.2c) and well-dispersed 50-90 nm diameter particles (Fig. 5.2d) on GC surface.

Figures 5.3 shows the cyclic voltammetry (CV) with electrochemical impedance spectra (insets of Figure 5.3) of G-MWNTs/GCE, graphene/GCE and GCE electrodes before (Fig. 5.3a) and after electrodeposition of Pt nanoparticles (Fig. 5.3b) in degassed 0.01M $K_3[Fe(CN)_6]$ / 0.1M KCl solution in deionized water at a scan rate of 50 mV s^{-1}. Well-defined oxidation and reduction peaks were observed with significant difference in peak-to-peak potentials separation on these electrodes. The highest peak current with smallest peak separation was noticed on the G-MWNTs/GCE electrode (Table 5.1), indicating the highest electroactive surface area. The electroactive surface area of the G-MWNTs/GCE, calculated using the Randles–Sevcik equation[18] [$I_p = 2.69 \times 10^5 AD^{1/2} n^{3/2} \nu^{1/2} c$, where n (=1) is the number of electrons participating in the redox reaction, A is the electroactive surface area (cm^2), D (=6.70 x 10^{-6} cm^2 s^{-1}) is the diffusion coefficient of $Fe_3(CN)_6^{3-}$ in solution, c (=0.01 M) corresponds to the concentration of the redox probe ($K_3[Fe(CN)_6]$), and ν is the scan rate of the potential perturbation (V s^{-1})], was determined to be 0.088 cm^2. This was 2.2 and 1.2 times larger compared to the surface areas for graphene/GCE and GCE electrodes, respectively (Table 5.1). The geometric surface area (GA) of these electrodes was 0.07 cm^2. The electroactive surface area of G-MWNTs/GCE,

graphene/GCE and GCE after electrodeposition of Pt nanoparticles increased to 1.21, 0.071 and 0.85 cm^2, respectively (Table 5.1).

Table 5.1. Comparison of electron transfer properties of various electrode systems

Electrode	Electroactive surface area (EA) (cm^2)	Ratio of electroactive to geometrical surface area (EA : GA)	ΔE (mV)	Charge transfer resistance (R_{ct} * GA) (Ohm cm^2)	K^0_{app} ($cm\ s^{-1}$) for $Fe(CN)_6^{3-/4-}$	Capacitance (μF cm^{-2})
GCE	0.074	1.05	142	45.43	5.85×10^{-4}	320
Graphene/GCE	0.040	0.57	299	96.22	2.76×10^{-4}	220
G-MWNTs/GCE	0.088	1.25	140	35.55	7.48×10^{-4}	620
Pt/ GCE	0.085	1.21	137	16.51	1.61×10^{-3}	3620
Pt/Graphene/GCE	0.071	1.01	138	18.74	1.41×10^{-3}	3260
Pt/G-MWNTs/GCE	0.121	1.72	136	12.75	2.08×10^{-3}	6900

The insets in Figure 5.3 show the impedance spectra of GCE, graphene/GCE and G-MWNTs/GCE without (Fig. 5.3a) and with Pt nanoparticles (Fig. 5.3b). In accordance with the inverse relationship with the electroactive surface area, the charge transfer resistance followed the order of G-MWNTs/GCE < GCE < graphene/GCE and Pt/G-MWNTs/GCE < Pt/GCE < Pt/graphene/GCE (Table 5.1). Correspondingly, the heterogeneous electron transfer rate constant, K^0_{app} ($=RT/n^2F^2CR_{ct}$) which is directly proportional to electroactive surface area, followed the order of G-MWNTs/GCE > GCE > graphene/GCE and Pt/G-MWNTs/GCE > Pt/GCE > Pt/graphene/GCE (Table 5.1).

These results are in conformity with the pattern observed in CV measurements, confirming the highest electroactive surface area for G-MWNTs/GCE, both before and after the Pt nanoparticles deposition. The lowest electroactive area and sluggish electron transfer rate for the graphene/GCE is attributed to a perfectly crystalline nature (negligible defects) of the single layer graphene film, as reported recently by electrochemical measurement on pristine epitaxial graphene grown on silicon carbide (SiC) surface.[19]

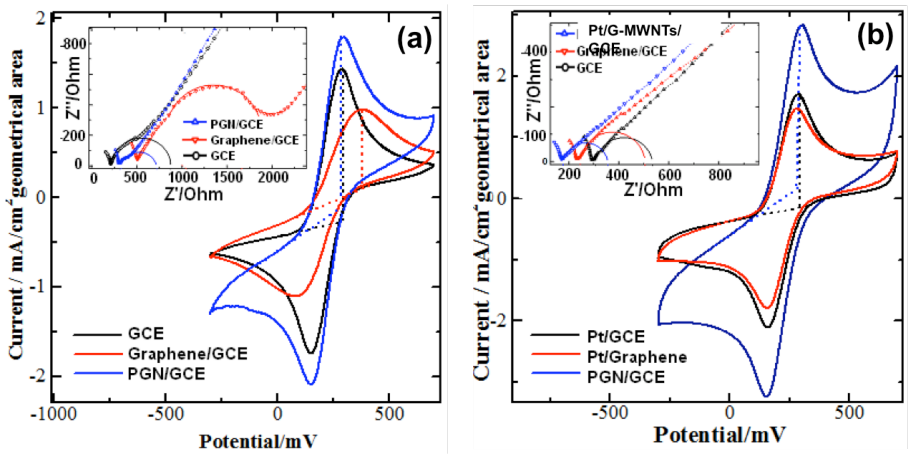

Figure 5.3 Cyclic voltammograms of a) G-MWNTs/GCE, Graphene/GCE and GCE (inset showing EDS spectra); b) Pt/G-MWNTs/GCE, Pt/Graphene/ GCE and Pt/GCE (inset showing EIS spectra) in 0.01 M $K_3[Fe_3(CN)_6]$ + 0.1M KCl in degased water, at scan rate of 50 mV sec^{-1}.

The electrochemical capacitance performance of the electrodes was performed using galvanostatic charge/discharge test. As evident from Figures 5.4a and 5.4b, the specific capacitance calculated from the charge-discharge cycling measurements

followed the order G-MWNTs/GCE > GCE > graphene/GCE and Pt/G-MWNTs/GE > Pt/GCE > Pt/graphene/GCE, indicating the G-MWNTs/GCE and Pt/G-MWNTs/GCE have highest capacitance in their respective group. The specific capacitance values tabulated in Table 5.1 were calculated by the formula, $C=I\ \Delta t\ /\Delta v$, where I is the discharge current, Δt is the discharge time, Δv is the potential drop in the discharge progress, and C is the specific capacitance of the material. The significantly higher specific capacitance of G-MWNTs hybrid than that of graphene and GCE is attributed to direct interactions between graphene and MWNTs in the hybrid film and high electroactive surface area. The significant increase in electroactive surface area of G-MWNTs/GCE and Pt-NP/G-MWNTs/GCE suggests that these may be promising electrodes for super-capacitor and direct methanol fuel cell.

Figures 5.5a-5.5c show typical cyclic voltammograms for the electro-oxidation of 0.5 – 3.0 M methanol in 0.1 M H_2SO_4 at Pt/G-MWNTs/GCE, Pt/graphene/GCE and Pt/GCE. As shown in the figures, all CV profiles consisted of two strong anodic peaks, a forward peak and a backward peak, which are well known to originate from the electrooxidation of methanol and the intermediate, respectively. The forward and backward anodic peaks in the scan correspond to oxidation of methanol forming Pt-adsorbed CO, which is known to poison the electrocatalyst, and CO_2 (eqns. 1 & 2) and the oxidation of adsorbed carbonaceous species to CO_2 (eqn. 3), respectively.[20]

$$Pt + CH_3OH \rightarrow Pt\text{-}CO_{ads} + 4H^+ + 4e^- \qquad (1)$$

$$CH_3OH + H_2O \rightarrow CO_2 + 6H^+ + 6e^- \qquad (2)$$

$$Pt\text{-}CO_{ads} + H_2O \rightarrow Pt + CO_2 + 2H^+ + 2e^- \quad (3)$$

Additionally, the Figure 5.5 illustrates that the methanol oxidation current density increased with increasing methanol concentrations up to 3 M at the Pt/G-MWNTs/GCE but leveled at 2 M at the Pt/GCE and Pt/graphene/GCE electrodes. This phenomenon is ascribed to the saturation of active sites at the electrode surface. Further, the methanol oxidation current density was highest at Pt/G-MWNTs/GCE at all methanol concentrations. Pt loading has direct effect on the oxidation of methanol. Hence, to compare the performance of different electrodes same number of CV cycles, in this study, 25 cycles was used for Pt nanoparticles deposition. This number of CV cycles value was chosen based on our observation and that reported in the literature[21], that there was not any significant increase in the methanol oxidation current beyond 25 cycles of Pt deposition at GCE. This phenomenon is ascribed to the saturation of active sites at the electrode surface.

Although a good catalytic activity was observed at Pt/G-MWNTs/GCE, poisoning of Pt by the carbonaceous intermediate, CO in particular, on the electrode surface cannot be

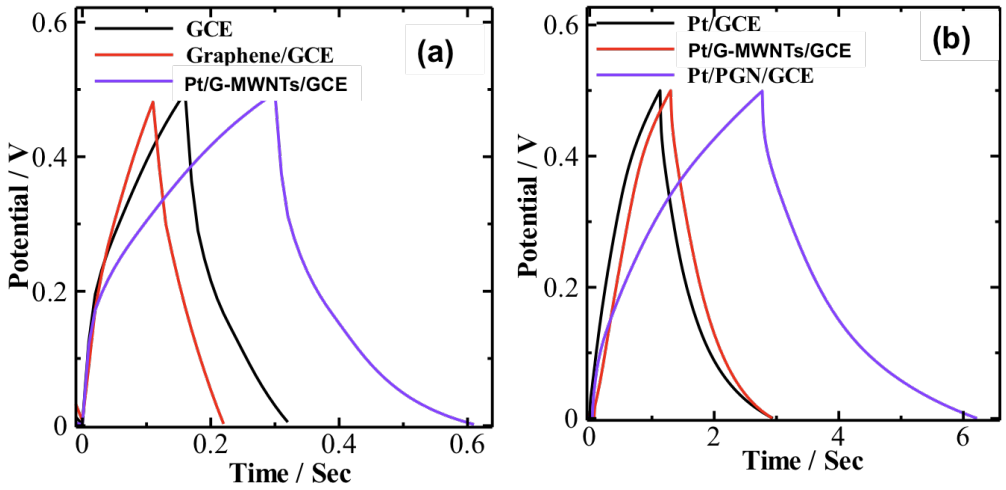

Figure 5.4 Galvanostatic charge-discharge curve of (a) G-MWNTs/GCE, Graphene/GCE and GCE; (b) Pt/G-MWNTs/GCE, Pt/Graphene/GCE and Pt/GCE, at a constant current density of 1mA/cm^2 in electrolyte 0.1M H_2SO_4.

overlooked. RuPt is commonly accepted as best electrocatalyst for methanol oxidation. Bimetallic Ru and Pt was electrochemically deposited on G-MWNTs/GCE, under identical conditions as described for Pt deposited electrodes, and evaluated for methanol oxidation. As shown in Fig. 5.6b, the backward anodic current peak was significantly reduced at RuPt/G-MWNTs/GCE in 1.0 M CH_3OH/0.1M H_2SO_4, indicating the removal of CO_{ads} by Ru via the following (eqn. 4) bi-functional mechanism.[22]

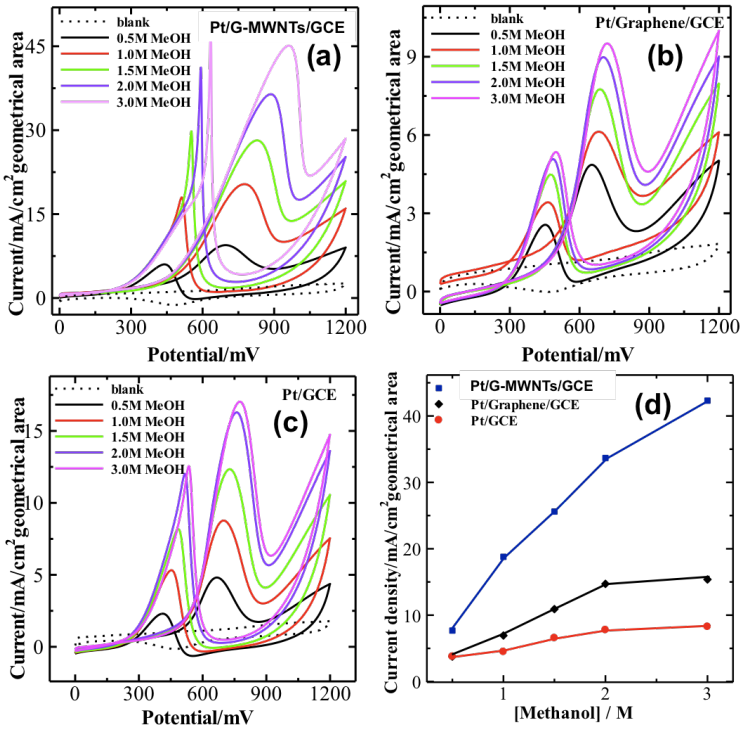

Figure 5.5 Cyclic voltammograms of a) Pt/G-MWNTs/GCE, b) Pt/Graphene/GCE, c) Pt/GCE in 0.0-3.0M CH_3OH/0.1 M H_2SO_4 at scan rate of 50 mV sec^{-1} and d) plot of forward anodic peak current density vs. CH_3OH concentration for Pt/G-MWNs/GCE, Pt/Graphene/GCE and Pt/GCE.

Additionally, the Figure 5.5 illustrates that the methanol oxidation current density increased with increasing methanol concentrations up to 3 M at the Pt/G-MWNTs/GCE but leveled at 2 M at the Pt/GCE and Pt/graphene/GCE electrodes. This phenomenon is ascribed to the saturation of active sites at the electrode surface. Further, the methanol oxidation current density was highest at Pt/G-MWNTs/GCE at all methanol concentrations. Pt loading has direct effect on the oxidation of methanol. Hence, to

compare the performance of different electrodes same number of cycles, 25 in this study, was used for Pt nanoparticles deposition. This number of cycles value was chosen based on our observation and that reported in the literature[21], that there was not any significant increase in the methanol oxidation current beyond 25 cycles of Pt deposition at GCE. This phenomenon is ascribed to the saturation of active sites at the electrode surface.

Although a good catalytic activity was observed at Pt/G-MWNTs/GCE, poisoning of Pt by the carbonaceous intermediate, CO in particular, on the electrode surface cannot be overlooked. RuPt is commonly accepted as best electrocatalyst for methanol oxidation. Bimetallic Ru and Pt was electrochemically deposited on G-MWNTs/GCE, under identical conditions as described for Pt deposited electrodes, and evaluated for methanol oxidation. As shown in Fig. 5.6b, the backward anodic current peak was significantly reduced at RuPt/G-MWNTs/GCE in 1.0 M CH_3OH/0.1M H_2SO_4, indicating the removal of CO_{ads} by Ru via the following (eqn. 4) bi-functional mechanism.[22]

$$Pt\ (CO)_{ads} + Ru\ (OH)_{ads} \rightarrow Ru + Pt + CO_2 + 2H + 2e^- \quad (4)$$

The ratio of the forward peak current density (I_f) to backward anodic peak current density (I_b), used to describe the catalyst tolerance to carbonaceous species accumulation, were observed to be 9.38, 1.11, 1.10 and 1.02 for RuPt/G-MWNTs/GCE, Pt/G-MWNTs/GCE, Pt/GCE and Pt/Graphene/GCE, respectively. The approximately 9-fold higher I_f/I_b for Ru-Pt/G-MWNTs/GCE over Pt/G-MWNTs/GCE confirms the ability of the bimetallic catalyst to withstand poisoning from carbonaceous materials by oxidizing them to CO_2. Although the I_f/I_b at Pt/G-MWNTs/GCE (1.11) is significantly lower than

RuPt/G-MWNTs/GCE, it is higher than those of recently reported for Pt/graphene oxide (0.83) and Pt/MWNT (0.72).[23]

The onset potential of methanol oxidation is also an indicator for determining and comparing the electrocatalyst activity for methanol oxidation.[24] The onset oxidation potential (Fig. 5.6 insets) was found to be in the order of RuPt/G-MWNTs/GCE (0.27V) < Pt/G-MWNTs/GCE (0.31V) < Pt/GCE (0.41V) < Pt/Graphene/GCE (0.46V), revealing that G-MWNTs supported catalyst, both Pt and RuPt, had enhanced electrocatalysis capability in the methanol oxidation when compared to graphene and glassy carbon catalyst supports.

Kinetics of methanol oxidation reaction at Pt deposited electrodes was investigated by studying the relationship between the forward anodic peak current density of methanol oxidation and CV scan rate (ν). Figure 5.7a-c shows CV curves for methanol oxidation at Pt/G-MWNTs/GCE, Pt/Graphene/GCE and Pt/GCE, at a scan rate of 25V to125 mV sec^{-1}. A linear relationship between forward peak current density and $\nu^{1/2}$ for Pt/G-MWNTs/GCE, Pt/Graphene/GCE and Pt/GCE, shown in Figure 5.7d, suggests that the oxidation behavior of methanol at all electrodes is controlled by diffusion process.[25] The larger slope for Pt/G-MWNTs/GCE (2.01) compared to Pt/graphene/GCE (0.40) and Pt/GCE (0.87) is indicative of a fast diffusion process of methanol on the surface of G-MWNTs hybrid film than those of graphene and GC catalyst supports. This result is also

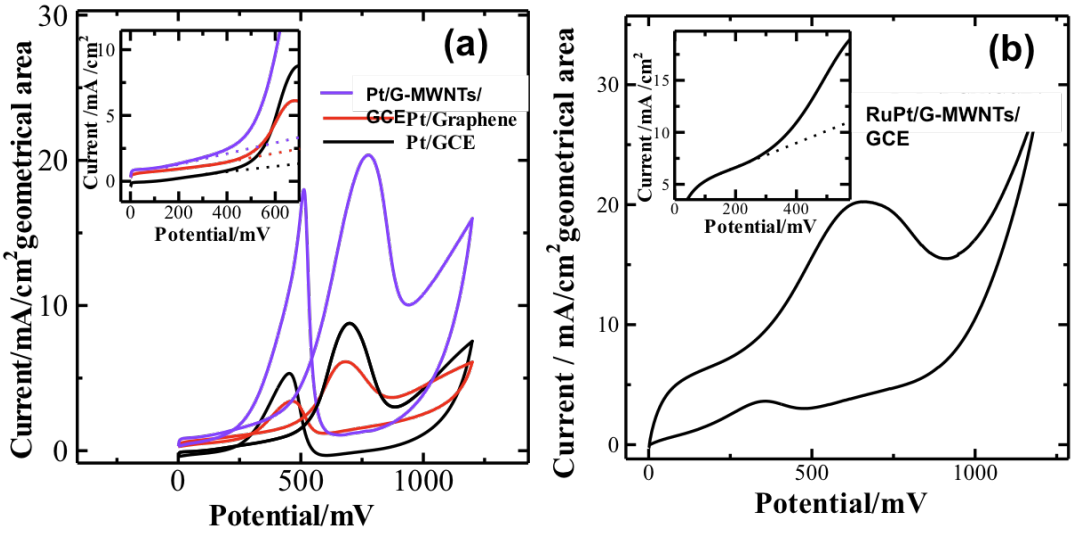

Figure 5.6 Electrocatalytic performance of a) Pt/G-MWNTs/GCE, Pt/ Graphene/GCE and Pt/GCE and b) RuPt/G-MWNTs/GCE in 1 M CH_3OH/0.1 M H_2SO_4 at a scan rate of 50 mV sec^{-1}.

attributed to large surface area of Pt nanoparticles catalyst per unit geometrical area of G-MWNTs hybrid electrode and is consistent with SEM and electroactive surface measurement studies, further suggests G-MWNTs hybrid film to be promising catalyst support for the direct DMFCs applications.

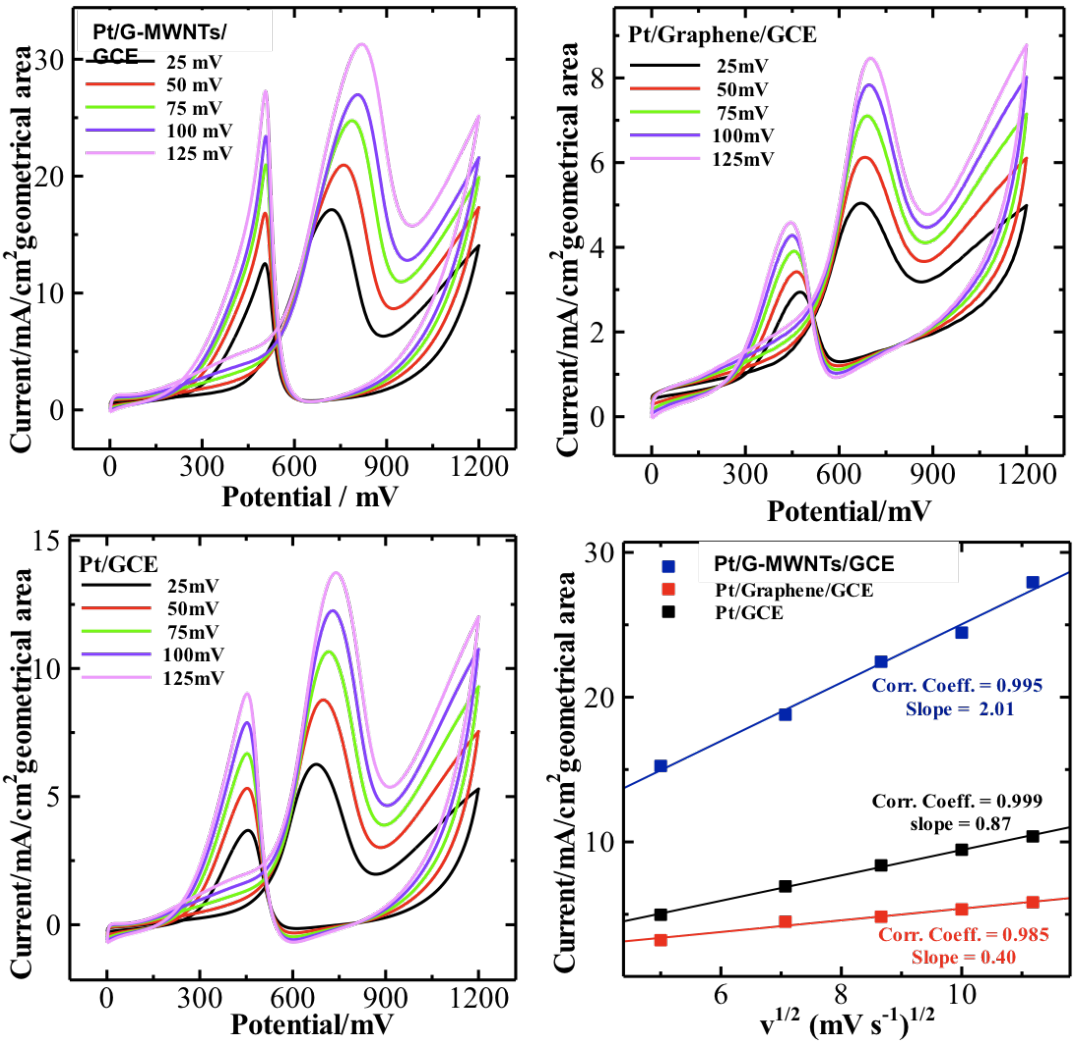

Figure 5.7 Cyclic voltammograms of a) Pt/G-MWNTs/GCE, b) Pt/Graphene/GCE, c) Pt/GCE in 1M CH_3OH/0.1 M H_2SO_4, at a scan rate of 25-125 mV sec^{-1} and d) the relationship of anodic forward peak current density vs. scan rate for Pt/G-MWNTs/GCE, Pt/ Graphene/GCE and Pt/GCE.

5.4 Conclusion

We have demonstrated an efficient fabrication of Pt nanoparticles deposited novel electrode system using Graphene-MWNTs hybrid nanostructure as catalyst support for the electro-oxidation of methanol. SEM analysis confirmed that flower-like Pt nanostructures of about 60-90 nm in size with cluster of needles were electrochemically deposited over the entire hybrid nanostructure. On the basis of CV results Pt/G-MWNTs/GCE exhibited the highest electroactive surface area with enhanced elctrocatalytical activity and fast diffusion process towards electrocatalytic oxidation of methanol as compare to GC and graphene modified GC catalyst supports. Additionally, RuPt/G-MWNTs/GCE prepared in the present work reduces the backward anodic current peak significantly by oxidizing the carbonaceous intermediate to CO_2. The high performance of G-MWNTs/GCE as catalyst support for electro-oxidation of methanol is due to the large surface area of unique 3D carbon nanostructure having efficient charge transfer at G-MWNTs/electrolyte interface allowing higher dispersion of Pt, and good electrical properties of MWNTs. These results suggest that G-MWNTs could be a potential candidate as a catalyst support material for the applications in the DMFCs.

5.5 References

1. Arico, A.S.; Srinivasan, S; Antonucci, V. DMFCs: From Fundamental Aspects to Technology Development. *Fuel Cell*. **2001**, *1*, 133-161.

2. Steele, B.C.H.; Heinzel, A. Materials for Fuel-Cell Technologies. *Nature* **2001**, *414*, 345-352.

3. Li, L.; Xing, Y. *J. Phys. Chem. C* 2007, *111*, 803-808.

4. Yoo, E. J.; Okada, T.; Kizuka, T.; Nakamura, J. Effect of Carbon Substrate Materials as a Pt-Ru Catalyst Support on the Performance of Direct Methanol Fuel Cells. *J. Power Sources* **2008**, *180*, 221–226.

5. Prabhuram, J.; Zhao, T. S.; Tang, Z. K.; Chen, R.; Liang, Z. X. Multiwalled Carbon Nanotube Supported PtRu for the Anode of Direct Methanol Fuel Cells. *J. Phys. Chem. B* **2006**, *110*, 5245–5252.

6. Liao, S.; Holmes, K. A.; Tsaprailis, H.; Briss, V. I. High Performance PtRuIr Catalysts Supported on Carbon Nanotubes for the Anodic Oxidation of Methanol. *J. Am. Chem. Soc*. **2006**, *128*, 3504–3505.

7. Wildgoose, G. G.; Banks, C. E.; Compton, R. G. Metal Nanoparticles and Related Materials Supported on Carbon Nanotubes: Methods and Applications. *Small* **2006**, *2*, 182–193.

8. Geim, A. K.; Novoselov, K. S. The Rise of Graphene. *Nat. Mater*. **2007**, *6*, 183-91.

9. Xu, C.; Wang, X.; Zhu, J. W. Graphene-Metal Particle Nanocomposites. *J. Phys. Chem. C* **2008**, *112*, 19841–19845.

10. Si, Y. C.; Samulski, E. T. Exfoliated Graphene Separated by Platinum Nanoparticles. *Chem. Mater.* **2008**, *20*, 6792–6797.

11. Yoo, E. J.; Okata, T.; Akita, T, Kohyama, M.; Nakamura, J.; Honma, I. Enhanced Electrocatalytic Activity of Pt Subnanoclusters on Graphene Nanosheet Surface. *Nano Lett.* **2009**, *9*, 2255–2259.

12. Blake, P.; Brimicombe P. D.; Nair, R. R.; Booth, T. J.; Jiang, D.; Schedin, F.; Ponomarenko, L. A.; Morozov, S. V.; Gleeson, H. F.; Hill, E. W.; Geim A. K.; Novoselov, K. S. Graphene-Based Liquid Crystal Device. *Nano Lett.* **2008**, *8*, 1704-1708.

13. Li, X.; Cai, W.; An, J.; Kim, S.; Nah, J.; Yang, D.; Piner R.; Velamakanni, A.; Jung, I.; Tutuc, E.; et al. Large Area Synthesis of High Quality and Uniform Graphene Films on Copper Foils. *Science* **2009**, *324*, 1312-1314.

14. Girishkumar G.; Hall, T. D.; Vinodgopal, K.; Kamat, P.V. Single Wall Carbon Nanotube Supports for Portable Direct Methanol Fuel Cells. *J. Phys. Chem. B* **2006**, *110*, 107-114.

15. Xing, Y. Synthesis and Electrochemical Characterization of Uniformly-Dispersed High Loading Pt Nanoparticles on Sonochemically-Treated Carbon Nanotubes. *J. Phys. Chem. B* **2004**, *108*, 19255-19259.

16. Yuan, J.; Wang, Z.; Zhang, Y.; Shen, Y. F.; Han, D.; Zhang, Q.; Xu, X.; Niu, L. Electrostatic Layer-by-Layer a of Platinum-Loaded Multiwall Carbon Nanotube Multilayer: A Tunable Catalyst Film for Anodic Methanol Oxidation. *Thin Solid Film* **2008**, *516* , 6531-6535.

17. Paul, R.K.; Ghazinejad, M.; Penchev, M.; Lin, J.; Ozkan, M.; Ozkan, C.S. Synthesis of a Pillared Graphene Nanostructure: A Counterpart of Three-Dimensional Carbon Architectures. *Small* **2010**, *6*, 2309–2313.

18. Wan, Q.; Wang, X.; Yu, F.; Wang, X.; Yang, N. Effects of Capacitance and Resistance of MWNT-Film Coated Electrodes on Voltammetric Detection of Acetaminophen. *J. Appl. Electrochem* ***2009***, *39*, 1145–1151.

19. Lim., C. X.; Hoh, H. Y.; Ang, P. K.; Loh, K. P. Direct Voltammetric Detection of DNA and pH Sensing on Epitaxial Graphene: An Insight Into the Role of Oxygenated Defects. *Anal. Chem.* **2010**, *82,* 7387–7393.

20. Chen, C.H.; Shimizu, K.; Lin, Y.Y.; Bailey, F.; Cheng, I. F.; Wai, C. M. Chemical Fluid Deposition of Pt-Based Bimetallic Nanoparticles on Multiwalled Carbon Nanotubes for Direct Methanol Fuel Cell Application. *Energy Fuels* **2007**, *21*, 2268-2271.

21. Wen, Y.; Ye, J.; Zhang, W.; Sheu, F.; Xu, G.Q. Electrocatalytic Oxidation of Methanol on a Platinum Modified Carbon Nanotube Electrode. *Microchim Acta* **2008**, *162*, 235–243.

22. Selvaraj, V.; Alagar, M. Pt and Pt–Ru Nanoparticles Decorated Polypyrrole/Multiwalled Carbon Nanotubes and Their Catalytic Activity Towards Methanol Oxidation. *Electrochem. Commun.* **2007**, *9*, 1145–1153.

23. Li, Y.; Gao, W.; Ci, L.; Wang C.; Ajayan, P. M. Catalytic Performance of Pt Nanoparticles on Reduced Graphene Oxide for Methanol Electro-Oxidation. *Carbon* **2010**, *48*, 1124-1130.

24. Han, D. M.; Guo, Z. P.; Zhao, Z. W.; Meng, Y. Z.; Shu, D.; Liu, H. K. Polyoxometallate-Stabilized Pt–Ru Catalysts on Multiwalled Carbon Nanotubes: Influence of Preparation Conditions on the Performance of Direct Methanol Fuel Cells. *J. Power Sources* **2008**, *184*, 361-369.

25. Honda, K.; Yoshimura, M.; Rao, T. N.; Tryk, D. A.; Fujishima, A.; Yasui, K; Sakamoto Y.; Nishio, K; Masuda H. Electrochemical Properties of Pt-Modified Nano-Honeycomb Diamond Electrodes. *J. Electroanal. Chem.* **2001**, *514*, 35-50.

CHAPTER 6

Conclusions

6.1 Summary

Using a chemical vapor deposition (CVD) technique, large area graphene films were synthesized utilizing surface catalysis mechanism on a copper surface depending on the carbon precursors such as methane (CH_4), acetylene (C_2H_2) and Ethanol (C_2H_5OH). By using Raman spectroscopy, X-ray photoelectron spectroscopy, electron diffraction pattern analysis and high-resolution transmission electron microscopy techniques, we demonstrated the polycrystalline nature of ethanol-based graphene film showing p-type semiconducting behavior as well as incorporation of oxygen-related carboxylic functional group (~ 3 at.%) as opposed to CH_4 and C_2H_2 based graphene film. The sizes of individual graphene crystallite in the ethanol-based graphene films synthesized at 900°C and 1000°C were about 2 nm and 5 nm, respectively, and they are oriented in [100] the crystal direction. The synthesized polycrystalline graphene film could potentially be exploited in the doping of heteroatoms as well as binding with other functional groups for desired applications. The reported method provides large-area polycrystalline graphene film, which could be a potential candidate to study further for applications in sensors, energy storage, biological systems and nanoelectronics.

Large area graphene nanomeshes with certain periodicity were synthesized from CVD-grown graphene film using the combination of reactive ion etching and nanosphere

lithography techniques. Fabricated graphene nanomesh sensor devices containing narrow neck width of about ~20 nm represented remarkably higher sensitivity to both NO_2 and NH_3 exposures than their film counterparts. Due to the higher defect density, ethanol-derived graphene nanomesh sensor showed enhanced responses and sensitivity than the methane-derived graphene nanomesh devices by the adsorption of maximum number of gas molecules. The sensitivity and estimated limit of detection of ethanol-based graphene nanomesh devices were about 4.32%/ppm and 15 ppb in NO_2, and 0.71%/ppm and 160 ppb in NH_3, respectively. These results revealed that the fabricated GNM sensors can be successfully used for detection of other electron-donating or electron-withdrawing species. Further, the decrease in neck width of synthesized nanomesh and/or surface modification of those nanomesh sensor devices with polymers or catalyst nanoparticles would increase the sensitivity further with possible selectivity.

On the other hand, a unique 3D carbon architecture that combines graphene and CNTs, was used in methanol oxidation to realize it's potential as a 3D electrode system in direct methanol fuel cells (DMFCs). The graphene/CNTs composite was transferred onto glassy carbon electrode (GCE) as supporting materials for platinum (Pt) electrocatalyst. Pt nanoparticles were electrochemically deposited over these carbon based support materials and the resulting Pt/G-MWNTs/GCE was characterized by scanning electron microscopy (SEM), energy dispersive spectroscopy (EDS), cyclic voltammetry (CV) and electrochemical impedance spectroscopy. The electrocatalytic properties of the modified electrode for electro-oxidation of methanol have been investigated by CV. Experimental results demonstrate an enhanced efficiency of the G-MWNTs hybrid film, as catalyst

support, for methanol oxidation in comparison to Pt nanoparticles, graphene and glassy carbon with regard to electroactive surface area, forward anodic peak current density, onset oxidation potential, diffusion efficiency and the ratio of forward to backward anodic peak current density (I_f/I_b). This enhanced catalytic performance towards methanol oxidation is due to the high surface area of three-dimensional G-MWNTs hybrid film, allowing higher dispersion of Pt together with excellent electrical properties of MWNTs.

6.2 Suggestions for Future Works

GNR SNAP (superlattice nanowire pattern): Patterning of CVD-graphene into aligned GNRs with specific width and pitch

One of the major challenges in the application of GNRs transistors includes patterning/aligning of sub-10 nm GNRs in a specific pitch over a large area to design ultrahigh density GNRs circuits.

It has been shown previously that SNAP technique can be used to produce aligned ultrahigh density Pt and/or Si nanowires. This technique involves growth of aligned metal nanowires (NWs) with specific diameter and pitch. These aligned NWs can be used a mask for a thin film semiconductor in fabricating ultrahigh-density semiconductor nanowires array by traditional top-down patterning methods.

The SNAP technique was being utilized to produce ultrahigh-density GNRs array using large area CVD-grown graphene. Figure 6.1 shows a schematic diagram of the process involved in synthesizing large area aligned GNRs array in specific width and

pitch. Figure 6.1 a shows a Pt deposited GaAs/AlGaAs superlattice that used to produce a aligned Pt NWs mask. Figure 6.1 b shows aligned Pt NWs on polymer/graphene/SiO_2/Si substrate after transferring from GaAs/AlGaAs superlattice. The average diameter of individual Pt NW was about 20 nm with a pitch of about 34 nm between two Pt NWs. The diameter and pitch of resulting Pt NWs reflect the as-grown GaAs/AlGaAs superlattice. Figure 6.1c shows schematic diagram of the process involving in top-down patterning of GNRs array. A modified RIE will be performed over the samples (Fig. 6.1b) in O_2 plasma to etch polymer/graphene in the unprotected area from Pt NWs mask, as shown in Figure 6.1c. Finally a lift-off in acetone would provide GNRs array onto SiO2/Si substrate. Detailed electrical characterization will then be done on fabricated aligned GNRs transistor devices.

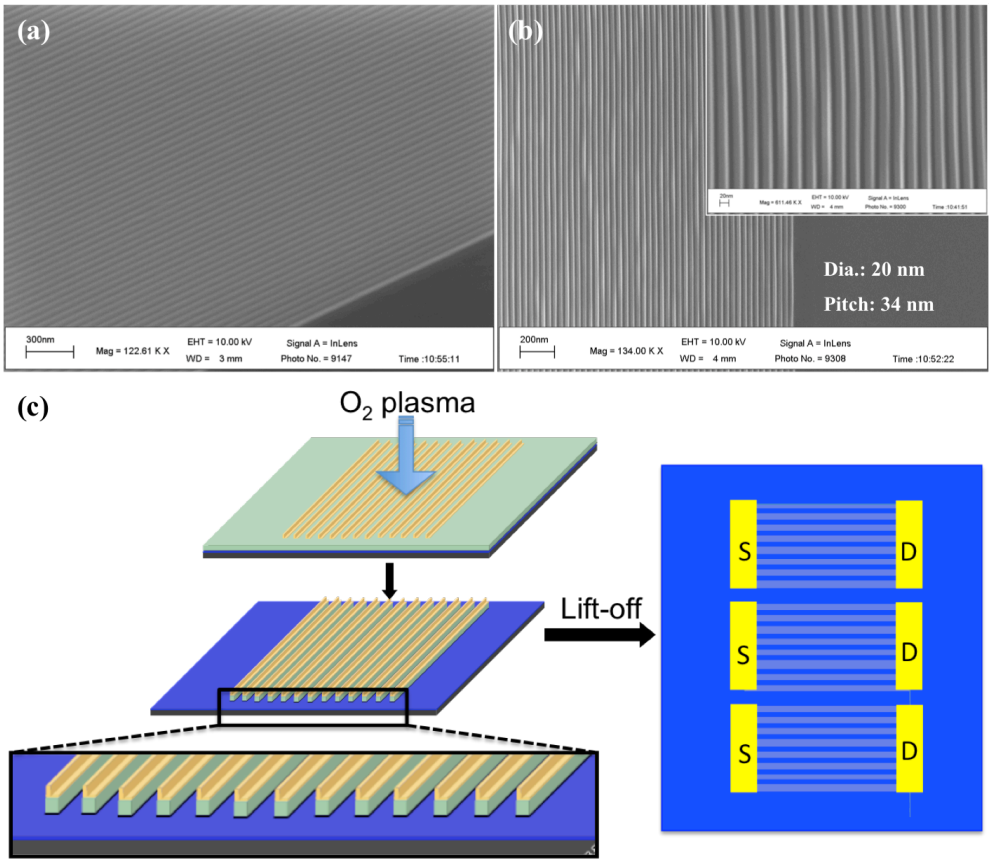

Figure 6.1 SNAP technique to synthesize ultrahigh-density GNRs array with narrow diameter and specific pitch. SEM images of (a) Pt deposited GaAs/AlGaAs superlattice and (b) ultrahigh-density Pt NWs (a part of about 250 Pt NWs) onto polymer/graphene/SiO_2/Si substrate after transfer process. (c) Next steps involved fabricating ultrahigh-density GNRs transistor array.

Appendix

Nonenzymatic Glucose Sensor Based on Platinum Nanoflowers on Multi-walled Carbon Nanotube/Graphene Hybrid

In this work, we demonstrate the electrodeposition of platinum nanoflowers on multi walled carbon nanotube (MWNT)/ graphene hybrid which is synthesized by one step chemical vapor deposition process via in situ vapor–liquid–solid and surface-catalyzed mechanisms. Structural characterization revealed that the roots of MWNTs were directly connected to the graphene floor. Electrodeposition of platinum with optimized parameters was performed at room temperature to obtain high density flower like nanostructures of platinum uniformly distributed over the hybrid membrane. This arrangement of Pt-nanoflowers/ MWNT/ graphene was used for amperometric detection of glucose in the physiological range at neutral pH. Direct oxidation of glucose takes place due to the electrocatalytic property of the Pt-nanoflowers resulting in the non-enzymatic detection of glucose. The developed sensor responded linearly to glucose over the range of 1-7 mM (R^2 = 0.978) with a sensitivity of 11.06 μA mM^{-1} cm^{-2}.

Introduction

Monitoring blood glucose levels is of prime importance in medical diagnostics and clinical applications. Over the past few decades, enzymatic glucose sensors have been developed and widely used for continuous blood glucose detection. However, the activity of enzymes is easily affected by temperature, pH value, humidity, and presence of toxic chemicals (Wilson and Turner, 1992). Further, the gradual degradation of enzyme over time, their high oxygen dependency and inability to offer anti-interference from other electroactive components present in blood glucose are certain issues that render them unsuitable for real time and reliable usage (Huot *et al*., 2009; Wilkins *et al*., 1995) for blood glucose monitoring.

Thus, the interest for enzyme-free glucose sensor that would directly oxidize glucose in solution has been keen. Among the nonenzymatic glucose sensors reported so far, platinum (Pt) has been the most popular material due to its high catalytic activity toward glucose oxidation (Aoun *et al*., 2003; Chung *et al*., 2003; Jin and Chen, 2007; Sheu *et al*., 2007; Xia *et al*., 2005).

Direct electrochemical oxidation of glucose on bulk platinum has been reported (Vassilyev *et al*., 1985). Ever since, different kinds of platinum based electrode materials like macroporous platinum (Chung *et al*., 2003) and (Xia *et al*., 2005) and platinum-nanotubule arrays (Yuan *et al*., 2005) electrodes with high electrode surface roughness have been developed to enhance the amperometric response of glucose oxidation and effectively lower the interference arising from other co-existing electroactive species.

However, surface poisoning by adsorbed intermediates (Ernst *et al*., 1979) and chloride ion, low sensitivity and poor selectivity are some drawbacks that still plague these electrodes. It has been reported that many metal nanoparticles and carbon nanotubes electrode show reproducible sensitivity in the presence of high concentration of chloride ion (Xu *et al*., 2004). (Xia *et al*., 2007) reported a nonenzymatic glucose sensor by using highly dispersed Pt nanoparticles supported on carbon nanotubes as sensing interface that provided better screening towards interfering analytes when detection of glucose is performed at an appropriate potential. Nano-structured Pt possesses a very large surface activation area, thereby favoring kinetically controlled reactions (i.e., the electrocatalytic oxidation of glucose) more than diffusion controlled reactions (i.e., the common electroactive species) thus offering higher sensitivity for glucose detection along with better selectivity towards interfering analytes.

There are fewer reports which exploit the unique combined properties of both carbon nanomaterials and Pt nanoparticles for enzyme free glucose detection via direct glucose electrocatalysis. Some examples include amperometric glucose detection using Pt nanoparticles in different carbon matrices such as Pt-activated carbon, Pt-Carbon nanofibers, Pt-MWNTs (Dempsey *et al*., 2010), Pt-nanoflowers on SWNT membrane (Lei *et al*., 2010) , Pt nanoparticles supported onto mesoporous carbon (Su *et al*., 2010) and Pt nanoparticles supported on multi-walled carbon nanotubes (Xia *et al*., 2007). Nonenzymatic glucose detection using multi-walled carbon nanotube electrodes has been reported (Xu *et al*., 2004). In this report, Xu and co-workers suggested that electrocatalytic oxidation of glucose in alkaline medium takes place directly at well-

aligned MWNT with possible minor contributions from the Co catalysts present on the Ta substrate.

Herein we report the synthesis of Pt- nanoflower like structures as the catalyst supported on MWNT/graphene hybrid and demonstrate its application as an enzyme free glucose sensor over the physiological range at neutral pH. Electrodeposition of Pt nanoparticles provides for a simple, cost effective and controlled approach of synthesizing nanoparticles of desired shape, size, distribution, and crystallinity by varying deposition parameters and substrate properties. It results in high purity nanomaterials at room temperature thus overcoming the short comings of other techniques that require elevated temperatures, extensive template removal procedures and relatively high loadings of Pt precursor for nanoparticles synthesis. Large area MWNT/graphene hybrid, on the other hand, synthesized by one step chemical vapour deposition technique (CVD) with its high surface to volume ratio and superior chemical, electrical, and mechanical properties constitutes an excellent catalyst supporting membrane. Thus the electrodeposition of uniformly spread, large surface area Pt-nanoflowers on MWNT/graphene hybrid provides a synergistic platform for the detection of glucose which results in better sensitivity and the ability to efficiently discriminate against other electroactive interferents.

Experimental

Chemicals and Reagents

Uric acid, Ascorbic acid and D-Glucose were procured commercially from Fisher Scientific and were used as received. Hydrogen hexachloroplatinate (IV) hexahydrate ($H_2PtCl_6 \cdot 6H_2O$) was purchased from ACROS. All buffer solutions used as supporting electrolytes were prepared in deionized water obtained by purifying distilled water through a Milli-Q plus (Millipore Inc) ultrapure water system.

Instrumentation

The structure and surface composition of the MWNT/graphene hybrid and later Pt- nanoflowers/ MWNT/graphene were characterized by a scanning electron microscope SEM (Leo, 1550) with a field emission source. Cyclic voltammetric and amperometic measurements were performed on a CHI electrochemical workstation (CHI Instruments, Inc., Austin, TX) at room temperature. A three electrode cell (5 ml) was used which consisted of the modified GC electrode (2.5 mm in diameter) as the working electrode, an Ag/AgCl electrode as the reference electrode and a large area Pt mesh as the counter electrode.

Synthesis of MWNT/ graphene hybrid

CVD synthesis of MWNT/graphene hybrid nanostructure was performed by a combination of in situ vapor–liquid–solid and surface-catalyzed mechanisms from a nearly similar procedure adapted from literature (Ozkan *et al*., 2010) . In brief, 1 nm Fe nanoparticles were deposited on the surface of copper film by electron beam evaporation (Temescal, BJD-1800). C_2H_2 (50 sccm) was used as a carbon source in an atmosphere of

flowing Ar (100 sccm) and H_2 (50 sccm) ; the flow rates being precisely controlled by using mass-flow controllers (MFC) to synthesize a large area, approx 1 inch sq. in dimension MWNT/graphene hybrid structure at 750^0 C for 10 minutes time. Growths of graphene and carbon nanotube take place simultaneously on copper foil and iron catalyst particles respectively. The mechanism of growth involved the synthesis of graphene film on copper substrate (Colombo *et al*., 2009) by vapor–liquid–solid mechanism technique and simultaneous in-situ growth of MWNTs through surface catalyzed expansion of Fe particles during the diffusion of carbon atoms. The Cu foil with the MWNT/graphene hybrid on top of it was then transferred into aqueous $FeCl_3$ solution (1M) and kept overnight wherein the copper was etched away leaving behind the hybrid structure on the surface of the etchant. The hybrid was then transferred onto aqueous HCl (5%) and DI water solution for cleaning residues, if any. No noticeable bulk defects were observed during the etching and cleaning processes, which confirmed the flexibility of the synthesized hybrid structure that consisted of high density MWNTs on top of monolithic graphene film.

For the purpose of electrochemical sensing, the MWNT/graphene hybrid was then transferred onto a freshly polished and cleaned glassy carbon (GC) electrode, diameter 2.5 mm by simple contact lifting from the surface of DI water. To ensure better adhesion of the hybrid onto GC, the electrode was kept in the oven maintained at 50^0C for 1 hour. Prior to the transfer of the hybrid graphene onto the GC electrode, the electrode was polished successively with 1 μm, 0.3 μm and 0.05 μm α-alumina powder

and rinsed thoroughly with distilled water between each polishing step. The GC was ultrasonicated thereafter in acetone and distilled water for 5 mins each.

Electrodeposition of Pt-nanoflowers

The electrodeposition of Pt-nanoflowers was carried out on the surface of the MWNT/ graphene /GC electrode from 5mM chloroplatinic acid hexahydrate (H_2PtCl_6) solution in presence of 0.1M HCl at ambient temperature. A three-electrode system was set up consisting of MWNT/ graphene/ GC as the working electrode, a platinum mesh and an Ag/AgCl (saturated with KCl) as the counter and reference electrode respectively. Pl-nanoflowers were synthesized on the surface of MWNT/graphene hybrid via cyclic voltammetry performed in the metallic precursor based electrolyte for 25 cycles at a scan rate of 50 mV/s between -0.7 and 0.3 V (vs. Ag/AgCl 3M KCl) at room temperature.

Results and discussions

Characterization

Structural characterization in terms of SEM was performed on the synthesized MWNT/graphene hybrid as shown in Fig. 1. The as grown hybrid revealed the roots of MWNTs to be directly connected to the graphene floor. Highly dense MWNTs with uniform and regular morphologies were spread over the large area graphene. This makes for an excellent conductive substrate for electrodeposition with high flexibility and stability. SEM micrographs were also recorded to study the morphology and distribution

of the electrodeposited Pt nanoparticles on the surface of graphene/ MWNT hybrid. As can be seen in Fig. 2, high density flower like Pt nanostructures were found uniformly deposited throughout the cross section of the graphene/ MWNT hybrid. Apart from having a uniform distribution, these nanoflowers like structures have a very high surface area.

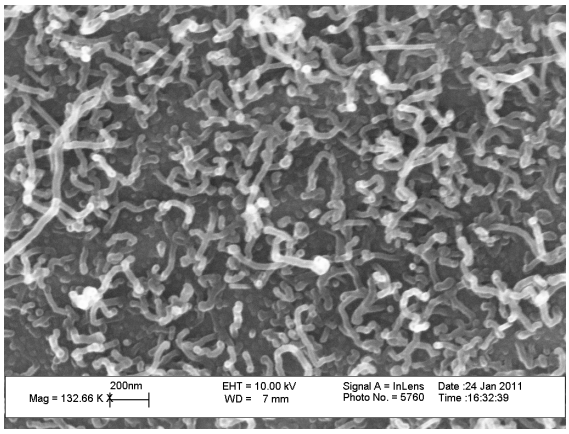

Figure 1 SEM image of MWNT/graphene hybrid.

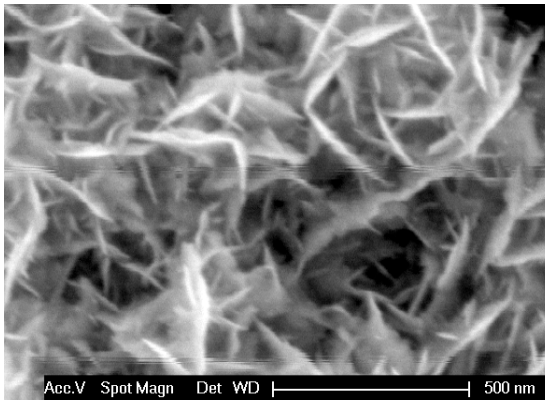

Figure 2 SEM image of Pt nanoflowers electrodeposited from 0.1 M HCl containing 5 mM H_2PtCl_6 for 25 cycles at a scan rate of 50 mV/s between -0.7 and 0.3 V (vs. Ag/AgCl 3M KCl) at room temperature.

Electro oxidation of glucose

In order to determine the accurate potential range for the electrooxidation of glucose, CVs of the electrodeposited Pt-nanoflowers on MWNT/graphene surface (Pt-nanoflower/ MWNT/ graphene) were performed before and after addition of glucose into phosphate buffer solution (pH 7.4). Injection of glucose enhances the glucose oxidation current. As seen clearly in Fig. 3, pronounced oxidation current peaks were observed at a low positive potential window of 0.4 to 0.7 V. Hydrodynamic voltammetry performed at three

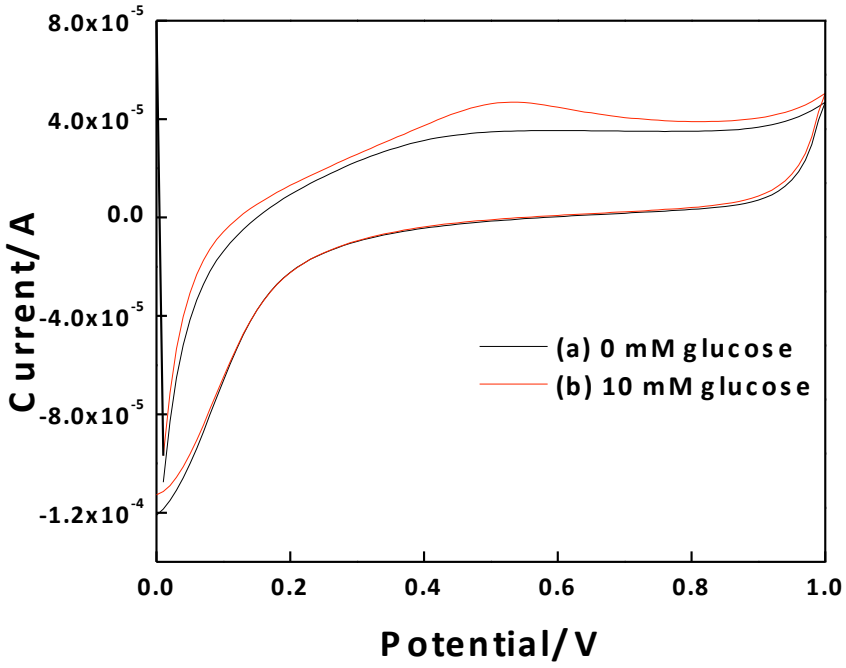

Figure 3 Response of Pt-nanoflower/ MWNT/ graphene to glucose electro-oxidation from 0.4 to 0.7 V vs. Ag/AgCl for (a) 0mM glucose, (b) 10 mM glucose at scan rate of 50 mV/s in 0.1M PB; pH 7.4.

different potentials revealed that the sensor exhibits improved signal-to-noise ratio and enhanced sensitivity towards glucose at an applied potential of 0.4 V as compared to 0.3 V and 0.5 V (data not shown). Lowering the working potential would improve the selectivity of the sensor further; however, it would also affect the sensitivity towards detecting glucose. Hence, in order to achieve a glucose sensor which exhibits better sensitivity and considerable selectivity in terms of its response towards interfering analytes at the same time, a trade off in applied potential is necessary. Thus, 0.4 V vs. Ag/ AgCl was chosen to the working potential for glucose detection.

Amperometric detection of glucose

Amperometric measurements of the Pt-nanoflowers/ MWNT/ graphene electrode to the sequential addition of glucose were carried out in a standard three electrode electrochemical cell configuration at +0.4 V in PB solution (pH 7.4, 5ml) under constant gently stirring conditions. The initial current response obtained in the buffer was considered as the saturated background current of the sensor. With every subsequent addition of glucose into the solution, rapid and steady state current signals were obtained as shown in Fig. 4. This was due to the direct electro-oxidation of glucose, which involved the steps of adsorption, electron transfer and subsequent chemical rearrangements limited within the electro deposited Pt surface. In brief, the mechanism (Chung *et al*., 2006) of glucose detection involves the glucose molecules to undergo electrosorption on the Pt-nanoflower electrode surface to form a layer of glucose

intermediates, which can be easily oxidized. These adsorbed intermediates are further oxidized at more positive potentials to form products such as gluconolactone or gluconic acid in neutral media. Fig. 5 shows the calibration plot for the successive increments of

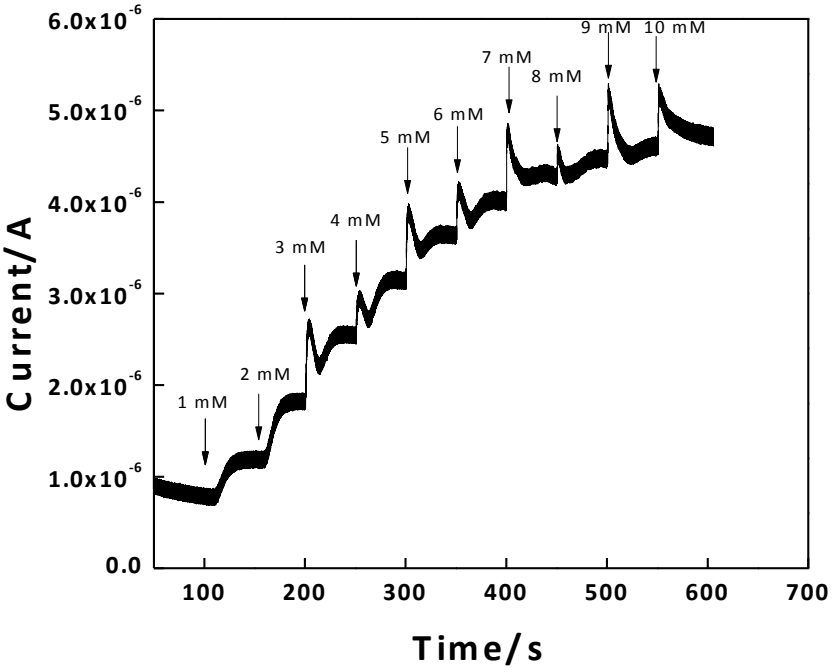

Figure 4 Real-time amperometric response of the Pt nanoflower/ MWNT/ graphene working electrode towards successive addition of glucose at 0.4 V vs. Ag/AgCl in 0.1M PB; pH 7.4.

glucose concentrations from 1 mM upto 10 mM range obtained from 3 electrodes. The calibration curve yields a linear chronoamperometric response range between 1 mM to 7 mM of glucose concentrations with a sensitivity of 11.06 μA mM^{-1} cm^{-2} (R^2 = 0.978) calculated as the slope of the linear region of the calibration curve divided by geometric

surface area of the GC electrode. The limit of detection of this Pt-nanoflowers/ MWNT/ graphene hybrid electrode was found out to be 0.387 mM based on the three times of signal-to noise ratio. To confirm that the direct oxidation of glucose is caused only due to the electrocatalytic property of the Pt-nanoflowers, a control experiment was performed wherein the as transferred MWNT/graphene hybrid was used as the working electrode and amperometric responses were recorded for subsequent additions of glucose (Fig. 6). No change in current response was observed thus confirming the fact that response comes from the direct glucose oxidation at the active sites of the catalyst.

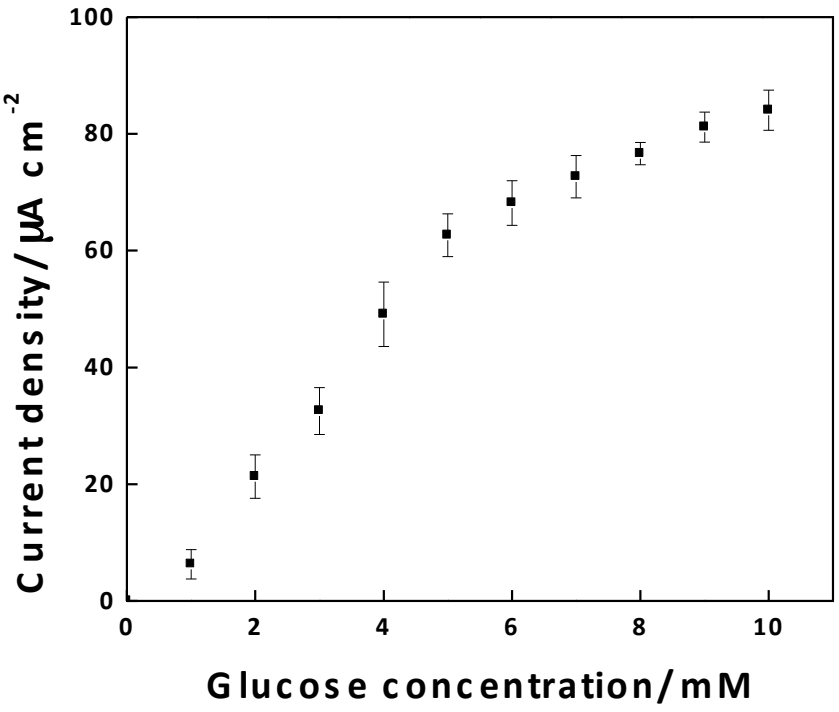

Figure 5 Calibration curve showing the response of electrodes (n=3) towards glucose.

Interference studies

The interferences arising from electroactive compounds like Ascorbic acid (AA) and Uric acid (UA) that co-exist along with glucose in physiological samples of blood was investigated. The range of concentration of these reducing agents in normal blood ranges

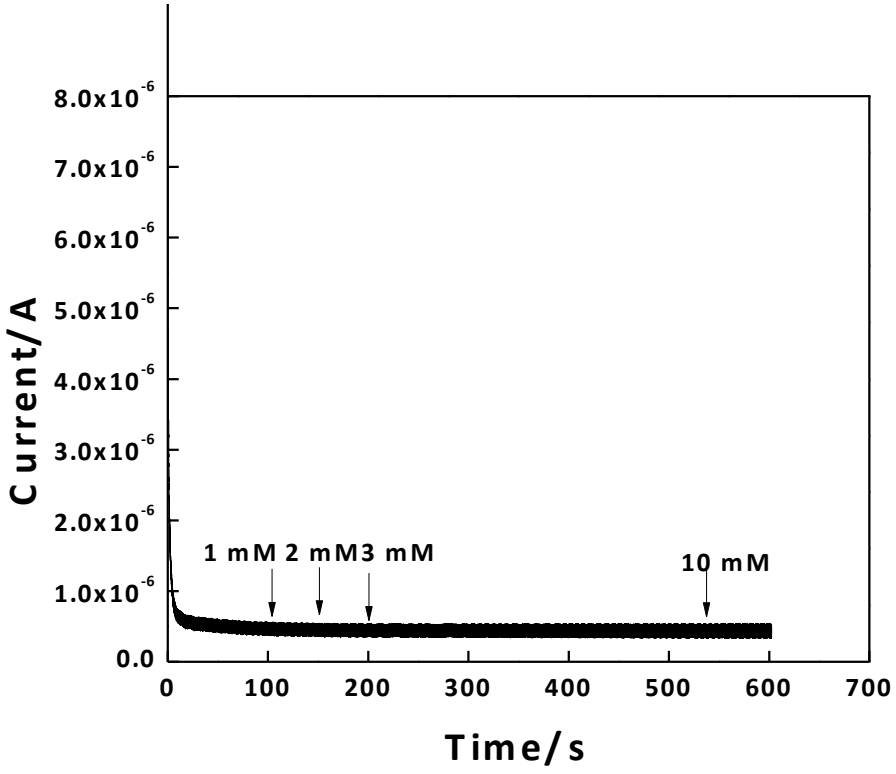

Figure 6 Real-time amperometric response of the MWNT/graphene working electrode towards successive addition of glucose at 0.4 V vs. Ag/AgCl in 0.1M PB; pH 7.4.

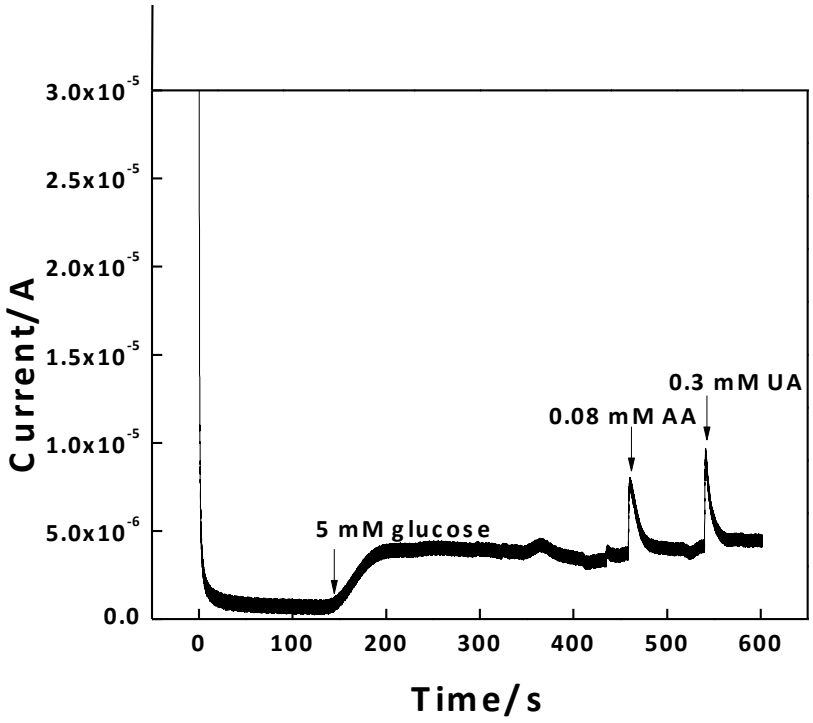

Figure 7 Real-time amperometric response of the Pt nanoflowers/MWNT/ graphene working electrode towards 5 mM glucose, 0.08 mM AA and 0.3 mM UA at 0.4 V vs. Ag/AgCl in 0.1M PB; pH 7.4.

between 0.02 and 0.08 mM (AA) and 0.18 to 0.42 mM (UA). Selectivity studies were performed using amperometric I (t) curves at +0.4 V that recorded the response signals of physiological levels of AA and UA during the detection of glucose. Figure 7 shows the

amperometric current responses to 5 mM glucose, 0.08 mM AA and 0.3 mM UA in PB buffer, pH 7.4 at +0.4 V operational potential. The current responses for the interfering analytes obtained by normalizing to the response for glucose i.e. 61.55 μA /cm^2 were found to be 16.5 % and 15.8 % for AA and UA respectively. In case of higher concentrations of interferants, surface modification of the Pt-nanoflowers/MWNT/graphene electrode can be done possibly by coating it with Nafion that has a considerable influence on the selectivity towards glucose by providing good anti-interference towards co-existing interferants (Tang *et al*., 2009; Xia *et al*., 2007).

Most of the electrochemical glucose sensors based on metals (Vassilyev *et al*., 1985) tend to lose their electroactivity due to the poisoning of chloride ions. The effect of chloride ions on the electrocatalytic ability of Pt-nanoflowers towards glucose oxidation was examined by recording amperometric response in supporting electrolyte with 0.15 mM NaCl (data not shown). It remained unchanged, thus, implying that the electrode retains its electroactivity in presence of chloride ion.

Results obtained from this work were compared with most recently reported Pt-nanoflowers on SWNT membrane for glucose detection (Lei *et al*., 2010). The demonstrated sensor in our case exhibits a higher sensitivity because of the synergistic benefits of high surface-to-volume ratio of the catalyst supporting structure along with high density, large surface area Pt-nanoflowers thus providing more active sites for the direct electrocatalysis of glucose. The quick response time (i.e. the time taken to reach 90% of the signal) of this sensor notably 12 seconds together with the ability to detect glucose with negligible interference from co-existant electroactive components makes it

an ideal device for the detection of blood glucose level in medical diagnostics and clinical applications.

Conclusion

A highly sensitive, low-potential and fast amperometric sensor based on Pt-nanoflowers electrodeposited on MWNT/graphene hybrid for the detection of blood glucose over the physiological range was developed and demonstrated. This enzyme free sensor exhibited a good linear dependence on the physiological glucose concentration range from 1 to 7 mM with a sensitivity of 11.06 μA mM^{-1} cm^{-2}. These results can be attributed to the enhanced surface-to-volume ratio of the catalyst supporting membrane which in turn facilitates uniform and good area coverage of the electrodeposited Pt-nanoflowers that act as active sites for direct glucose oxidation with high utilization efficiency. The developed sensor offers good anti-interference to electroactive interferences such as ascorbates and urates that are commonplace in real blood samples. This novel platform of MWNT/ graphene hybrid with its high electrical conductivity, mechanical strength and large specific surface area can be used as a superior catalyst supporting matrix in a wide array of electrochemical applications such as biosensors and renewable, sustainable direct methanol fuel cells.

References

Aoun, S.B., Bang, G.S., Koga, T., Nonaka, Y., Sotomura, T., Taniguchi, I., 2003. Electrocatalytic oxidation of sugars on silver-UPD single crystal gold electrodes in alkaline solutions. Electrochem Commun 5(4), 317-320.

Chung, T.D., Park, S., Boo, H., 2006. Electrochemical non-enzymatic glucose sensors. Anal Chim Acta 556(1), 46-57.

Chung, T.D., Park, S., Kim, H.C., 2003. Nonenzymatic glucose detection using mesoporous platinum. Anal Chem 75(13), 3046-3049.

Colombo, L., Li, X.S., Cai, W.W., An, J.H., Kim, S., Nah, J., Yang, D.X., Piner, R., Velamakanni, A., Jung, I., Tutuc, E., Banerjee, S.K., Ruoff, R.S., 2009. Large-Area Synthesis of High-Quality and Uniform Graphene Films on Copper Foils. Science 324(5932), 1312-1314.

Dempsey, E., Rathod, D., Dickinson, C., Egan, D., 2010. Platinum nanoparticle decoration of carbon materials with applications in non-enzymatic glucose sensing. Sensor Actuat B-Chem 143(2), 547-554.

Ernst, S., Heitbaum, J., Hamann, C.H., 1979. Electrooxidation of Glucose in Phosphate Buffer Solutions .1. Reactivity and Kinetics Below 350 Mv-Rhe. J Electroanal Chem 100(1-2), 173-183.

Huot, C., Girardin, C.M., Gonthier, M., Delvin, E., 2009. Continuous glucose monitoring: A review of biochemical perspectives and clinical use in type 1 diabetes. Clin Biochem 42(3), 136-142.

Jin, C.C., Chen, Z.D., 2007. Electrocatalytic oxidation of glucose on gold-platinum nanocomposite electrodes and platinum-modified gold electrodes. Synthetic Met 157(13-15), 592-596.

Lei, Y., Su, L.A., Jia, W.Z., Zhang, L.C., Beacham, C., Zhang, H., 2010. Facile Synthesis of a Platinum Nanoflower Monolayer on a Single-Walled Carbon Nanotube Membrane and Its Application in Glucose Detection. J Phys Chem C 114(42), 18121-18125.

Ozkan, C.S., Paul, R.K., Ghazinejad, M., Penchev, M., Lin, J.A., Ozkan, M., 2010. Synthesis of a Pillared Graphene Nanostructure: A Counterpart of Three-Dimensional Carbon Architectures. Small 6(20), 2309-2313.

Sheu, F.S., Cui, H.F., Ye, J.S., Zhang, W.D., Li, C.M., Luong, J.H.T., 2007. Selective and sensitive electrochemical detection of glucose in neutral solution using platinum-lead alloy nanoparticle/carbon nanotube nanocomposites. Anal Chim Acta 594(2), 175-183.

Su, C., Zhang, C., Lu, G.Q., Ma, C.N., 2010. Nonenzymatic Electrochemical Glucose Sensor Based on Pt Nanoparticles/Mesoporous Carbon Matrix. Electroanal 22(16), 1901-1905.

Tang, F.Q., Yang, L.Q., Ren, X.L., Zhang, L., 2009. A practical glucose biosensor based on Fe(3)O(4) nanoparticles and chitosan/nafion composite film. Biosens Bioelectron 25(4), 889-895.

Vassilyev, Y.B., Khazova, O.A., Nikolaeva, N.N., 1985. Kinetics and Mechanism of Glucose Electrooxidation on Different Electrode-Catalysts .1. Adsorption and Oxidation on Platinum. J Electroanal Chem 196(1), 105-125.

Wilkins, E., Atanasov, P., Muggenburg, B.A., 1995. Integrated Implantable Device for Long-Term Glucose Monitoring. Biosens Bioelectron 10(5), 485-494.

Wilson, R., Turner, A.P.F., 1992. Glucose-Oxidase - an Ideal Enzyme. Biosens Bioelectron 7(3), 165-185.

Xia, X.H., Rong, L.Q., Yang, C., Qian, Q.Y., 2007. Study of the nonenzymatic glucose sensor based on highly dispersed Pt nanoparticles supported on carbon nanotubes. Talanta 72(2), 819-824.

Xia, X.H., Song, Y.Y., Zhang, D., Gao, W., 2005. Nonenzymatic glucose detection by using a three-dimensionally ordered, macroporous platinum template. Chem-Eur J 11(7), 2177-2182.

Xu, G.Q., Ye, J.S., Wen, Y., Zhang, W.D., Gan, L.M., Sheu, F.S., 2004. Nonenzymatic glucose detection using multi-walled carbon nanotube electrodes. Electrochem Commun 6(1), 66-70.

Yuan, J.H., Wang, K., Xia, X.H., 2005. Highly ordered platinum-nanotubule arrays for amperometric glucose sensing. Adv Funct Mater 15(5), 803-809.